SERI/STR--211-3580

DE89 009491

SERI/STR-211-3580
UC Category: 271
DE89009491

Task B: Research on Stable High-Efficiency, Large Area Amorphous Silicon-Based Solar Cells

Phase II Annual Subcontract Report 1 February 1988 - 1 February 1989

A. W. Catalano, R. R. Ayra, M. S. Bennett, C. R. Dickson, B. Fieselmann, B. Goldstein, J. Morris, J. L. Newton, J. G. O'Dowd, R. S. Oswald, E. Twesme, S. Wiedeman, L. Yang
Solarex Thin Film Division
Newtown, Pennsylvania

October 1989

SERI Technical Monitor: B. Stafford

Prepared under Subcontract No. ZB-7-06003-2

Solar Energy Research Institute
A Division of Midwest Research Institute

1617 Cole Boulevard
Golden, Colorado 80401-3393

Prepared for the
U.S. Department of Energy
Contract No. DE-AC02-83CH10093

MASTER

DISTRIBUTION OF THIS DOCUMENT IS UNLIMITED

DISCLAIMER

This report was prepared as an account of work sponsored by an agency of the United States Government. Neither the United States Government nor any agency thereof, nor any of their employees, makes any warranty, express or implied, or assumes any legal liability or responsibility for the accuracy, completeness, or usefulness of any information, apparatus, product, or process disclosed, or represents that its use would not infringe privately owned rights. Reference herein to any specific commercial product, process, or service by trade name, trademark, manufacturer, or otherwise does not necessarily constitute or imply its endorsement, recommendation, or favoring by the United States Government or any agency thereof. The views and opinions of authors expressed herein do not necessarily state or reflect those of the United States Government or any agency thereof.

DISCLAIMER

Portions of this document may be illegible in electronic image products. Images are produced from the best available original document.

NOTICE

This report was prepared as an account of work sponsored by an agency of the United States government. Neither the United States government nor any agency thereof, nor any of their employees, makes any warranty, express or implied, or assumes any legal liability or responsibility for the accuracy, completeness, or usefulness of any information, apparatus, product, or process disclosed, or represents that its use would not infringe privately owned rights. Reference herein to any specific commercial product, process, or service by trade name, trademark, manufacturer, or otherwise does not necessarily constitute or imply its endorsement, recommendation, or favoring by the United States government or any agency thereof. The views and opinions of authors expressed herein do not necessarily state or reflect those of the United States government or any agency thereof.

Printed in the United States of America
Available from:
National Technical Information Service
U.S. Department of Commerce
5285 Port Royal Road
Springfield, VA 22161

Price: Microfiche A01
Printed Copy A06

Codes are used for pricing all publications. The code is determined by the number of pages in the publication. Information pertaining to the pricing codes can be found in the current issue of the following publications which are generally available in most libraries: *Energy Research Abstracts (ERA)*; *Government Reports Announcements* and Index (*GRA* and I); *Scientific and Technical Abstract Reports (STAR)*; and publication NTIS-PR-360 available from NTIS at the above address.

SUMMARY

Semiconductor Materials Research

The major focus of this subtask has been on improving the quality of wide bandgap a-SiC:H alloys and narrow bandgap a-SiGe:H alloys. We have explored intrinsic a-SiC:H alloys deposited from a large number of feedstocks, with various diluents and under many deposition conditions. Amorphous SiGe:H work has mainly been concentrated on deposition from silane and germane feedstock. Work on deposition of a-Ge:H films was also initiated. The transport and optical properties of undoped films were characterized by Photothermal Deflection Spectroscopy, Raman Spectroscopy, dark and photo-conductivity, and visible and near infrared spectroscopy. During the latter part of this period we set-up Steady-State Photocarrier Grating (SSPG) technique to measure the ambipolar diffusion length of undoped films. Initial measurements on a-SiGe:H films show a decrease in the diffusion length with increase in germanium content of the alloy films. Although the mobility-lifetime ($\mu\tau$) product decreases for both the wider and the narrower bandgap alloys as the carbon and the germanium content increases respectively, there are marked differences in the optical absorption spectra of these two alloys. The carbon containing alloys exhibit an increase in the Urbach energy as a function of carbon indicating an increase in the tail density of states distribution. In contrast, no such increase in either the tail or the midgap density of states is evident in silicon germanium alloys. Raman spectroscopy of a-SiGe:H alloys suggests that the alloys are inhomogeneous, showing a higher concentration of Ge-Ge bonds than expected from a random mixing model.

High-Efficiency Device Research

In contrast, silicon-carbon single junction devices have resulted in open-circuit voltages as high as 0.96 V with above 0.6 fill-factor. Silicon-germanium devices show far better performance using p/i graded interface, i(a-Si)/i(a-SiGe) graded interface and an inverse graded interface at the i/n junction along with an amorphous silicon n-layer compared to an a-SiGe:H n-layer. Initial results indicate that the transport properties of alloys are improved by trace boron doping. The best single junction device with 1.55eV bandgap i-layer material had a conversion efficiency of 10.1%. The device exhibited a current density of 20 mA/cm^2. Single junction devices with an i-layer thickness of only 1000A and bandgap of about 1.4eV exhibit excellent long wavelength response with above 40% response at 800nm and above 10% response at 900nm.

Several stacked junction configurations have resulted in conversion efficiencies above 10%. Four configurations have been used: An a-SiC top cell with either a-Si:H or a-SiGe:H bottom cells, as well as both an a-Si:H/a-SiGe:H and a-Si:H/a-Si:H tandem device. 10.5% efficiency has been obtained by coupling a-SiC top cell with an a-SiGe:H bottom cell while a-SiC/a-Si:H structure yielded 10.2%. Triple stacked cells in which the bottom most cell has a 1.4eV bandgap a-SiGe:H alloy have resulted in conversion efficiencies above 9%. Major problems exist in accurate measurement of low bandgap devices by using a Xenon simulator filtered for AM1.5 spectrum because such simulators have relatively poor outputs at long wavelengths. A multi-source simulator is under construction to overcome this problem.

Stacked junction devices have shown far less susceptibility to light-induced degradation. The best a-Si:H/a-Si:H stacked junction devices which had an initial performance close to 9% lost less than 14% of its initial performance after 1150 hours of continuous exposure to AM1 illumination. Analysis indicates that the rate of degradation of stacked junction devices is the mean of the rates of degradation of the individual devices.

Microcrystalline p-layer silicon films have been prepared by either rf or dc glow-discharge. It is possible to prepare microcrystalline p-type films containing carbon albeit in an amorphous phase. Even though excellent conductivities and activation energies have been obtained and direct evidence of microcrystallinity in p-i-n devices have been observed by TEM, higher open-circuit voltages have not been obtained.

Non-Semiconductor Materials Research

Modelling of optical enhancement of long wavelength light in single junction devices suggests that several parasitic losses are present in the device structure. In most cases, the absorption in the rear contact is the major loss mechanism. This accounts for the 14% improvement in the short-circuit current density of a-Si:H single junction devices with ITO/Ag as compared to Al rear contact. No statistically significant difference was found by varying the ITO thickness from 1000A to 5000A.

A variety of materials including epoxy, urethane and asphaltic material were developed to achieve isolation breakdown voltage greater than 1550 volts dc. Several spray-type encapsulant materials have been evaluated. Varnish, epoxy, urethane and their derivatives, epoxy urethane and acrylic urethane have been developed. All these materials are cost effective and adaptable to continuous in-line manufacturing.

Submodule Research

The focus of this subtask has been fourfold. First, the development of high efficiency a-Si:H single junction modules, second, the development of stable a-Si:H stacked junction modules, and third, development of high efficiency alloy stacked modules, and fourth, development of advanced laser scribing processes.

Amorphous silicon single junction modules have been fabricated with active area conversion efficiency as high as 9.4% and with fill-factors as high as 0.74. This was accomplished by employing Al rear contact but reducing the width of segments thereby decreasing the series resistance contribution of tin oxide to the fill-factor of modules.

During this period-more than 200 a-Si:H/a-Si:H modules were fabricated with average conversion efficiencies above 6%. These were light-soaked for 200 hours and the extrapolated value of degradation for one year is 14.8%. This is a marked improvement over single junction modules.

The best all alloy submodule had an active area conversion efficiency of 7.73% and a total area conversion efficiency of 7%. This module had an a-SiC:H top device and an a-SiGe:H bottom device. Since the rear contact was Al which is a poor reflector of long wavelength light, the current density of this module was limited.

During this period an advanced laser scribing process which reduces the number of laser scribing steps from three to two was developed. This process has successfully passed the critical environmental tests. This development would significantly impact the cost and reliability of the manufacturing process of modules.

TABLE OF CONTENTS

FIGURE CAPTIONS

TABLE CAPTIONS

1.0 SEMICONDUCTOR MATERIALS RESEARCH

1.1 INTRODUCTION

High efficiency multi-junction amorphous silicon based solar cells require the development of device quality wide and narrow bandgap alloys. We have been investigating a-SiC:H alloys (Eg = 1.7eV to 2.0eV) for the wide bandgap intrinsic layer and a-SiGe:H alloys (Eg = 1.7eV to 1.1eV) for narrow bandgap intrinsic layer. Alloy material research is critical to improvement of transport properties of these alloys which should translate into improved performance and stability of multijunction solar cells.

During the period of this report, we have concentrated our efforts on depositing alloy films under various deposition conditions and numerous novel feedstocks. The films were characterized by measuring the dark and photoconductivity, the conductivity activation energy, IR absorption by means of FTIR spectroscopy and Raman spectroscopy, midgap density of states, Urbach edge, and optical bandgap using PDS (Photo thermal deflection spectroscopy) and visible and near infrared absorption spectroscopy. Recently, we have set-up the steady-state photocarrier grating (SSPG) technique to measure the ambipolar diffusion length in films. Periodically elemental analysis was done by Rutherford Back Scattering (RBS) and Energy Dispersive X-ray Analysis (EDAX). We have chosen the mobility-lifetime ($\mu\tau$) product derived from the photoconductivity data and lately the ambipolar diffusion length measurements derived from SSPG as a measure of film quality recognizing that the former measurement being a majority carrier measurement may be affected by factors such as the Fermi level position and may not be totally applicable to minority carrier devices such as solar cells. At present we are in the process of making complete sets of solar cells with i-layers deposited under the same conditions as were used for the films. This will allow us to establish material measurement(s) which are suitable to determine the device quality of these alloys.

1.2 WIDE BANDGAP ALLOYS

Wide bandgap a-SiC:H alloys were deposited using a variety of feedstocks, diluents, and deposition conditions. These are partially listed in Table 1-1. Although no single scheme has been devised into which all results can fit, some of our findings are summarized below:

1) A mixture of SiH_4 and CH_3-SiH_3 produced films which were, at a given bandgap, indistinguishable from films produced from CH_4 feedstock, using any of the measurements available to us. However, carbon was incorporated into the films much more efficiently than from a silane-methane mixture.

2) Films deposited from ethylene (C_2H_4) were uniformly poor. We suspect that all feedstock containing double and triple C-bonds will have similar poor properties. It was necessary to dilute this feedstock in hydrogen to avoid graphitic deposits.

3) Films grown from methane highly diluted in argon have much greater carbon incorporation and in some cases superior photoconductive properties.

4) a-SiC:H films deposited from methane diluted in either H_2 or Ar were of superior quality than those deposited from methane with no dilution. This conclusion is based on the IR peaks around 2000cm^{-1} (indicative of mono-or di-hydride bonding in a dense network) and 2070cm^{-1} (indicative of similar bonding in an environment of larger microvoids).

5) Films deposited from methane with no H_2 dilution show fewer CH_2, CH_3, Si-CH_3 bonds as the deposition power is increased. Similar films deposited with H_2 dilution show that the 2070cm^{-1} peak, the Si-CH_3 peak and the Si-H wag peak all broaden as the power increases.

TABLE 1-1

FEEDSTOCKS USED FOR THE PREPARATION OF THE a-$Si_{1-x}C_x$:H ALLOYS

Feedstock	Diluent
CH_4	none
"	Ar
"	H_2
"	He
C_2H_6	none
C_2H_4	H_2
SiH_3-CH_3	none
"	Ar
"	H_2

6) A few SiN films were grown with bandgaps in the 1.9eV range using NH_3 and NF_3 as feedstocks. These had very similar properties to a-SiC:H films of the same bandgap.

1.3 NARROW BANDGAP ALLOYS

We have taken two approaches to the narrow bandgap a-SiGe:H alloy research. The first approach was to deposit a-SiGe:H alloys in the bandgap range of 1.4 - 1.5eV with conventional feedstock of silane-germane mixtures with or without diluents and to find the optimum deposition conditions for high quality films. The second approach was to find the optimum deposition conditions for good quality a-Ge:H films.

Experiments in the first approach involved our normal feedstock, which is silane and germane with no dilution. Three variables were simultaneously varied: temperature in the range of 230° C to 300° C, total gas flow (SiH_4 + GeH_4) and total power. In all cases the germane fraction (GeH_4/(GeH_4 + SiH_4)) was then adjusted to produce a film with an optical bandgap of 1.45eV (2E03 from PDS spectra). Results of these films is presented in terms of ambipolar diffusion length measurements (to be described separately in another section) although the same qualitative results are found if the mobility-lifetime product is used instead (Figure 1-1). The highest ambipolar diffusion length occurs for films deposited at the highest temperature, 300° C, although considerable scatter is evident. A better correlation is found if one plots the ambipolar diffusion length (or mobility-lifetime product) vs. the fraction of germane in the deposition gas as shown in Figure 1-2. The best quality film at a given bandgap is deposited under conditions which use as small a fraction of germane in the feedstock as possible. This requires deposition at higher temperatures low power and low total flow. As can be seen from Figure 1-2, our present deposition conditions are near optimum.

Attempts to use inert gas dilution have not been successful in depositing films with improved properties. Also films prepared with SiH_4 + GeF_4 do not show any significant improvement in the $\mu\tau$ product over films prepared from silane-germane mixtures.

The second approach involves an investigation of the optimal deposition conditions for a-Ge:H films. Knowledge of these conditions could provide a clue to the region of the parameter space which should be explored to improve the alloy material. We have deposited a-Ge:H films from germane gas with and without diluents such as argon and hydrogen as a function of deposition temperature, pressure and power. The opto-electronic properties of some films is summarized in Table 1-2. The films which were found to have the sharpest Urbach edge and lowest midgap DOS are believed to be of relatively high quality. However, many of the films with the highest $\mu\tau$ product and highest ratio of light to dark conductivity had high dark conductivities, high Urbach edges, and high midgap absorption. Figure 1-3 shows the PDS spectra of some a-Ge:H films deposited under different conditions. Although the highest H_2 dilution used thus far has been 5:1, preliminary results indicate that even higher dilution ratios may be beneficial.

The mobility-lifetime product ($\mu\tau$) and Urbach edge for wide bandgap and narrow bandgap alloy films are shown in Figures 1-4 and 1-5 respectively. Several trends are readily apparent. The photoconductive properties of the alloys fall as the bandgap (estimated to be the energy at which the absorption coefficient equals $2x10^3 cm^{-1}$ as measured by PDS) moves away in either direction from that of a-Si:H. Specifically, the logarithm of $\mu\tau$ product falls linearly with bandgap more or less independently of the preparation method. The fall-off in the $\mu\tau$ product is much more rapid for silicon-carbon and silicon-nitrogen alloys than for silicon-germanium alloys. There is also a pronounced difference in the slope of the Urbach edge for the alloys. The Urbach edge is strongly dependent on the bandgap for the wide bandgap alloys but is relatively independent of bandgap for a-SiGe:H alloys. Therefore, the mechanism for the inferior transport properties of the two classes of alloys appears to be quite different. The lack of an increase in the midgap density of states with decreasing bandgap for a-SiGe:H alloys, also associated with the light-induced defects, suggests a mechanism other than the dangling bond defect limits the transport properties. The problem may lie with preferred Ge-Ge bonding or clusters of Ge leading to large potential fluctuations in the material and recombination centers. We have used Raman spectroscopy to study the inhomogeneities in a-SiGe:H alloys and these results are discussed elsewhere in this report.

FIGURE 1-1 AMBIPOLAR!:DIFFUSION LENGTH AS A FUNCTION OF GERMANE FRACTION IN THE DEPOSITION GAS FOR VARIOUS a-SiGe FILMS OF 1.45eV BANDGAP.

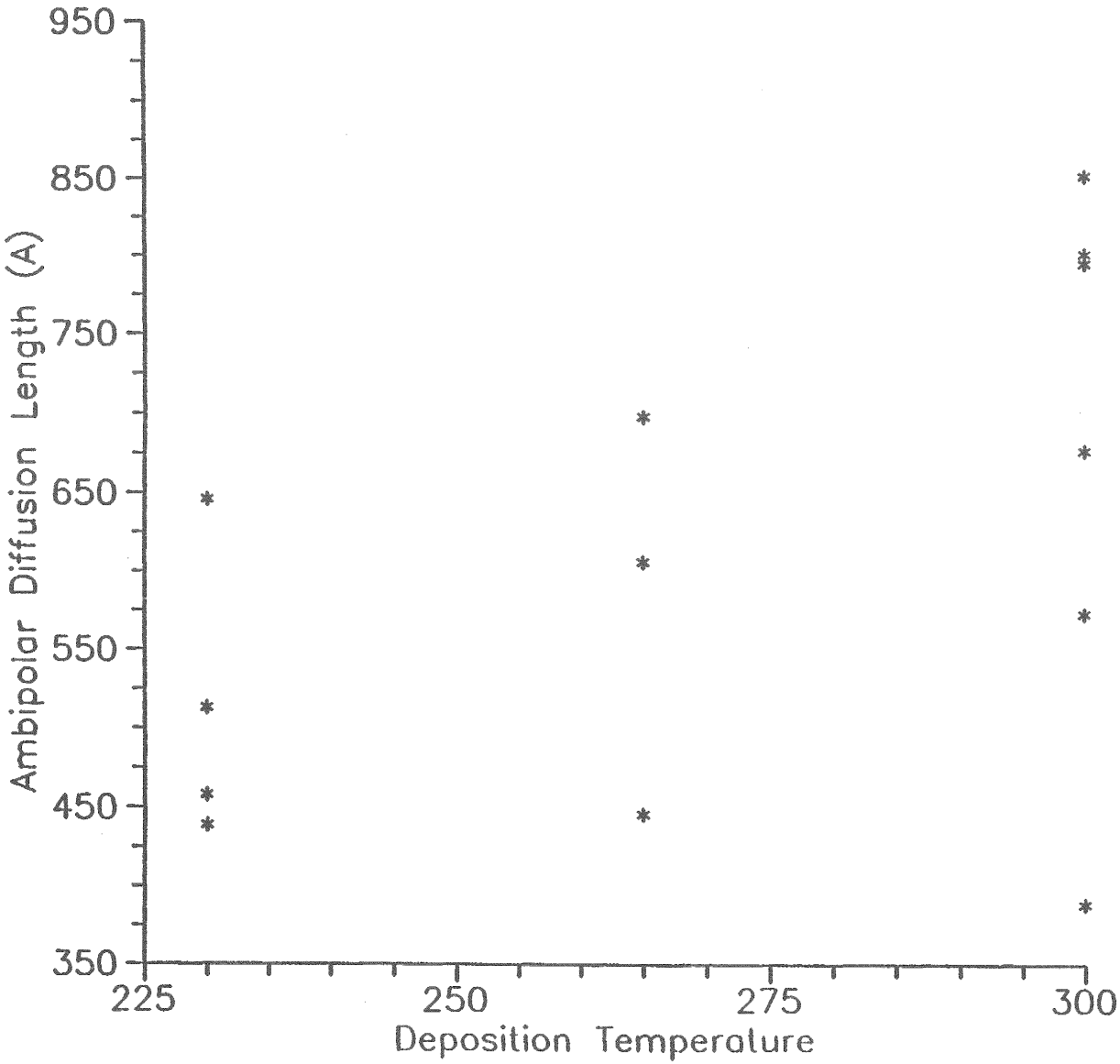

FIGURE 1-2 AMBIPOLAR DIFFUSION LENGTH AS A FUNCTION OF DEPOSITION TEMPERATURE FOR VARIOUS a-SiGe FILMS OF 1.45eV BANDGAP.

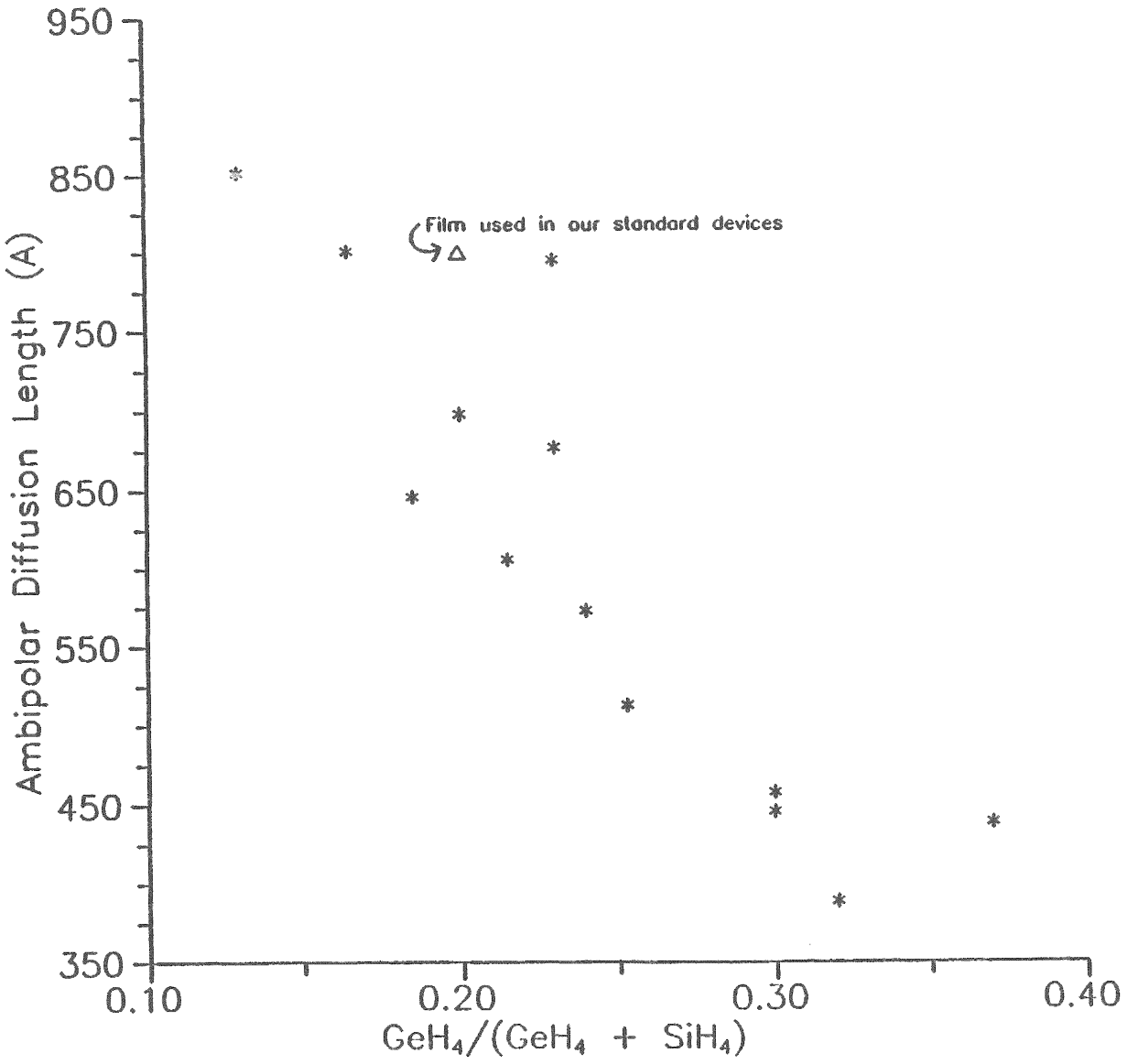

TABLE 1-2

A COMPARISON OF THE DEPOSITION CONDITIONS
AND OPTICAL AND ELECTRONIC PROPERTIES
FOR SOME a-Ge:H FILMS

temp	pressure	growth rate	dilution	Urbach energy	Absorption coefficient at 0.62eV	$\mu\tau$	$\frac{\sigma_{ph} - \sigma_{dark}}{\sigma_{dark}}$
° Cm	Torr	A/sec		meV	$1/cm^2$	cm /v	
290	500	1.83	5:1 H_2	59	109	$1.2(10)^{-7}$	.067
340	400	6.50	5:1 H_2	55	129	$4.7(10)^{-8}$	.023
340	400	2.14	5:1 H_2	56	150	$1.9(10)^{-7}$	.045
240	400	6.33	5:1 H_2	59	126	$4.7(10)^{-8}$	.032
340	550	1.90	5:1 H_2	56	126	$2.6(10)^{-8}$	.023
240	400	8.53	5:1 Ar	144	452	$7.2(10)^{-6}$	.072
240	500	16.0	1:1 Ar	103	228	$4.1(10)^{-7}$	.056
340	600	8.0	none	90	572	$9.8(10)^{-9}$	.005
290	600	6.44	5:1 Ar	73	579	$3.7(10)^{-7}$	.009

FIGURE 1-3 COMPARISON OF PDS SPECTRA OF a-Ge:H FILMS DEPOSITED USING VARIOUS DILUTION CONDITIONS.

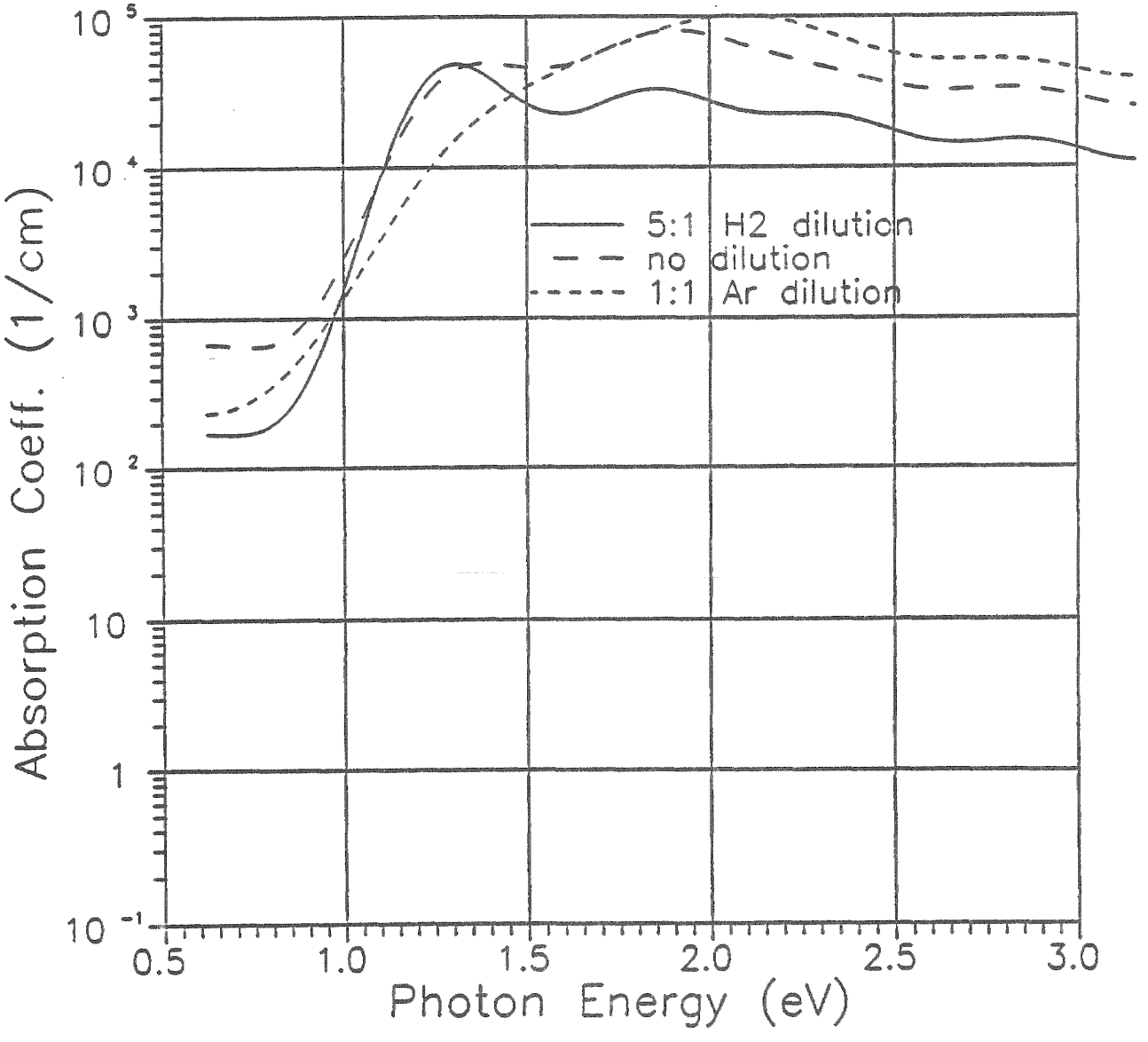

FIGURE 1-4 MOBILITY-LIFETIME PRODUCT PLOTTED VERSUS OPTICAL BANDGAP OF a-$Si_{1-x}C_x$:H and $Si_{1-x}Ge_x$:H FILMS

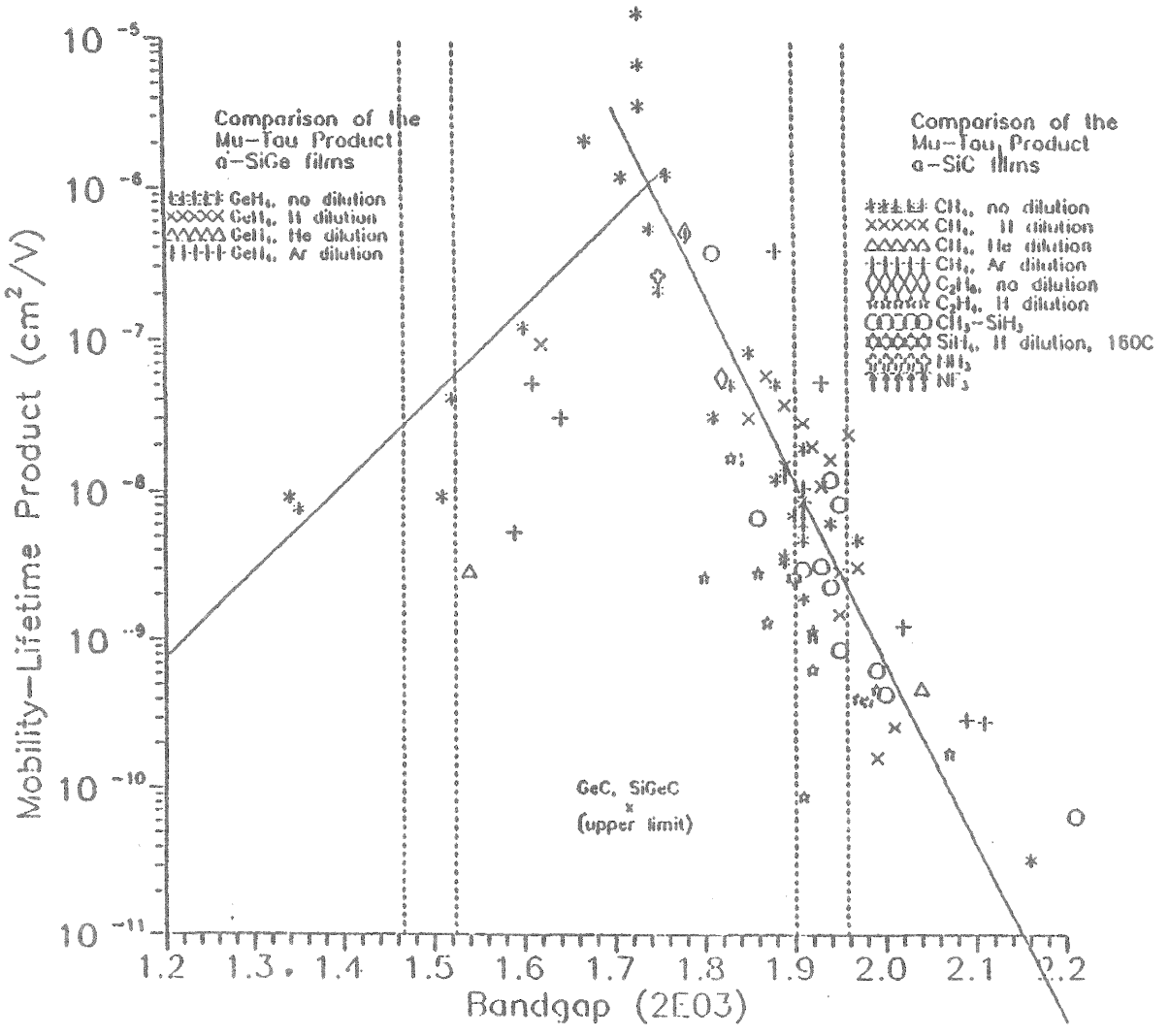

FIGURE 1-5 . URBACH ENERGY AS A FUNCTION OF BANDGAP FOR a-$Si_{1-x}Ge_x$:H AND a-$Si_{1-x}C_x$:H.

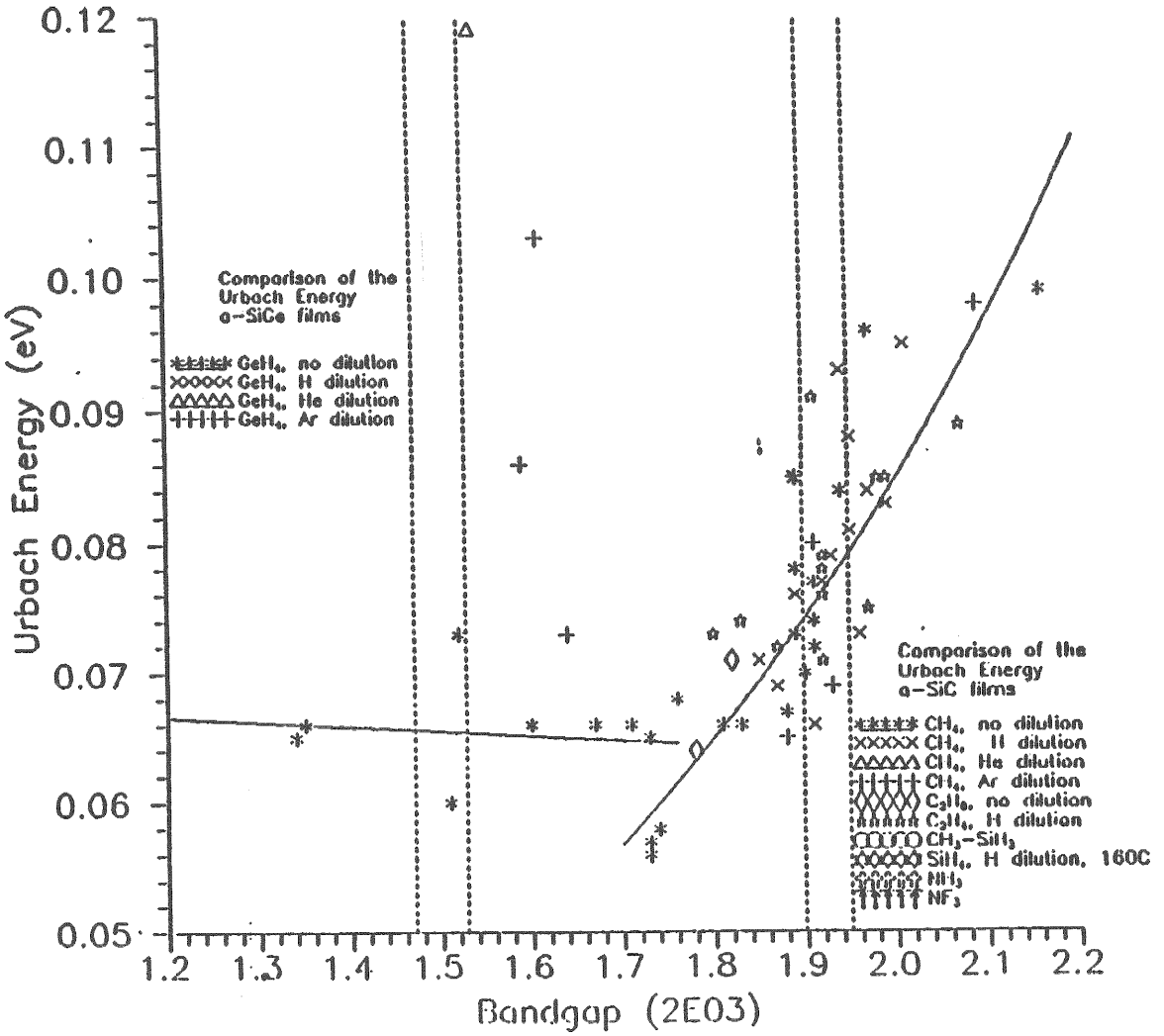

1.4 STEADY-STATE PHOTOCARRIER GRATING TECHNIQUE (SSPG)

Solar cells are well known to be ambipolar devices in which equal amounts of photoexcited electrons and holes must be extracted to external electrodes and thus the performance of which is usually limited by the type of carrier with poorer transport properties. For amorphous semiconductors, including the most commonly used a-Si:H and a-SiGe:H alloys, many experimental studies indicate that the transport properties of holes are much worse than those of electrons. For an example, the drift mobility of electrons is more than an order of magnitude larger than that of holes. Such a large asymmetry between electrons and holes makes many conventionally used characterization techniques, such as, photoconductivity inappropriate for determining the hole transport properties and hence unable to correlate well with solar cell performance and provide guidelines in the optimization process. Therefore, ambipolar diffusion length has been recognized for a long time being one of the most relevant parameters to characterize semiconductor materials for photovoltaic applications because it not only represents appropriately the minority carrier transport properties, but also relates closely to the collection length which is the quantity to describe current collection in a p-i-n cell for a given electric field. In the past, the surface photovoltage technique (SPV) has been the most commonly used technique for ambipolar diffusion length measurement for a-Si:H. However, problems associated with the fact that the absorption depth of the light and the width of the depletion region at the junction are of comparable dimension and that it is difficult to measure accurately the absorption depth has limited the SPV technique from providing a reliable measure of the diffusion length.

Recently, a new method called the steady state photocarrier grating (SSPG) technique has been developed for the measurement of ambipolar diffusion length in amorphous semiconductors aiming to make it important in the search for high efficiency solar cells. Since there is no junction involved in the measurement and the length scale against which the diffusion length is measured is set by the period of a light grating produced by the interference of two coherent laser beams, the SSPG technique immediately avoids the problems posed to the SPV technique. Realizing these advantages, we have set up the SSPG technique at Solarex and made a number of studies with it which will be described in this section.

The SSPG technique utilizes a coplanar geometry of a photoconductor on which a spatially modulated light intensity produces a grating of photocarrier generation. This grating becomes blurred due to carrier diffusion. The photoconductivity σ_g transverse to the grating fringes is then expected to depend on the ratio L/Λ, where L is the ambipolar diffusion length and Λ is the known grating period. The procedure which enables the derivation of the magnitude of L/Λ is based on a comparison of σ_g and σ, where the latter quantity is the photoconductivity for uniform illumination. Suppose that the grating is created by two coherent beams with intensities F_1 and F_2. The experimentally determined ratio

$$\beta = \frac{\sigma_g - \sigma(F_1)}{\sigma(F_1+F_2) - \sigma(F_1)} \qquad (1\text{-}1)$$

can be shown to be related to L/Λ by

$$\beta = 1 - 2\gamma\gamma_o^2/\{(1+\gamma F_2/F_1)[1+(2\pi L/\Lambda)^2]^2\} \qquad (1\text{-}2)$$

where γ is the exponent in the power law dependence of photoconductivity on light intensity, γ_o is an experimental quality factor. If the above expression is rewritten as

$$1/\Lambda^2 = \{(2\gamma)^{1/2}\gamma_o/[1-\beta)(1+\gamma F_2/F_1)]^{1/2} - 1\}/(2\pi L)^2, \qquad (1\text{-}3)$$

the value of L can be easily obtained from the intercept in the $1/\Lambda^2$ versus $(1/1-\beta)^{1/2}$ plot.

To demonstrate the sensitivity of the technique, we show in Figure 1-6 experimental data for two a-SiGe:H samples (E_g~1.6eV) made with different deposition currents of 50 and 80mA and otherwise identical conditions. It is evident that SSPG measured a better diffusion length for the film with 80mA current (~15% higher) in agreement with solar cell performances incorporating such i-layers. This and other similar experiments such as diffusion length versus deposition temperature showed that SSPG is indeed a reliable technique for measuring the ambipolar diffusion length and its sensitivity is better than 10%.

Figures 1-7 and 1-8 show the diffusion lengths (a) and optical bandgaps (b) of a series of a-SiGe:H alloys as functions of germane fraction in the mixtures of silane and germane. While the bandgap showed a smooth decrease with increasing germane fraction, the decrease of the diffusion length, which is expected, showed an uneven rate of decrease. From a fundamental point of view, this is interesting because it reflects the mechanism that SiGe alloys are formed with the corresponding transport properties. Practically, it provides an important piece of information for optimizing the performance of devices containing such alloys when one has to compromise between bandgap and carrier transport.

Since light intensity dependence of ambipolar diffusion length gives information on the distribution of density of states (DOS) as that of photoconductivity does for states near the conduction band edge, we have done some measurements to study this effect. Generally, the intensity dependence of diffusion length can also be characterized by a power law, $L \propto F^{-s}$, as shown experimentally for six samples in Figure 1-9. The exponent s varied from 0.09 to 0.17 among those samples which included intrinsic a-Si:H, a-SiGe:H with E_g = 1.6eV and a trace boron doped a-Si:H. The magnitude of the exponent relates to the slope of the exponential DOS near the quasi-Fermi level, namely the larger the s value, the steeper the DOS varies with energy. Our results indicate that different deposition conditions as well as doping can cause variations in the DOS.

As we discussed in the previous paragraph, low level boron-doping changes the hole transport property quite dramatically as represented by the ambipolar diffusion length. We have made systematic studies of this effect with both a-Si:H and an a-SiGe:H alloy with E_g = 1.6eV. Figures 1-10a and b show diffusion lengths of a-Si:H (a) and a-SiGe:H (b) as functions of gas phase boron-doping level. For both materials, the diffusion lengths increased quite strongly with very low level of doping until they peaked at around 0.2ppm level with ~70% increase from the undoped sample in the case of a-Si:H and ~40% in the case of a-SiGe:H. Further doping then caused the diffusion length to fall continuously. Dark conductivity measurements showed that although B-doping does in general shift Fermi level toward valence band edge, the magnitude of this shift at 0.2ppm doping level is small (<50meV). The electron $\mu\tau$ product measured from photoconductivity , on the other hand, exhibited sharp decreases, as much as an order of magnitude, at this doping level. These experiments seem to indicate that trace amount of boron when incorporated can significantly improve the hole transport, probably increasing lifetime, through a reduction of hole recombination centers. The fact that the diffusion length peaked at a very low doping level, which was confirmed by the little movement of the Fermi energy, suggests that the number of hole recombination centers being reduced might be small, but the trapping cross section is large in order to account for the observed effect. The doping seems to induce extra defect states for electrons as indicated by photoconductivity measurements. Finally, these extra doping induced defects, when exceeding the effect of reducing existing hole defects, when exceeding the effect of reducing existing hole recombination centers with further doping, caused the diffusion length to decline.

We are currently carrying out experiments to incorporate such low-level boron doped i-layers into solar cells to examine whether the observed increase in diffusion length can be translated into an improvement in cell performance. However, doping can introduce other effects such as changes in the spatial distribution of the built-in electric field, which also have to be taken into account in a device application.

Finally, we present diffusion length measurements on the effect of light induced degradation. Figure 1-11 shows the normalized diffusion length, L/L_0, as a function of hours of AM1 light soaking for three different samples. Up to 300 hours, all samples degraded considerably, ranging from 76% to 84%. a-Si:H seems to

FIGURE 1-6 AMBIPOLAR DIFFUSION LENGTH OF TWO a-SiGe (1.GeV BANDGAP) SAMPLES DEPOSITED AT DIFFERENT CURRENTS.

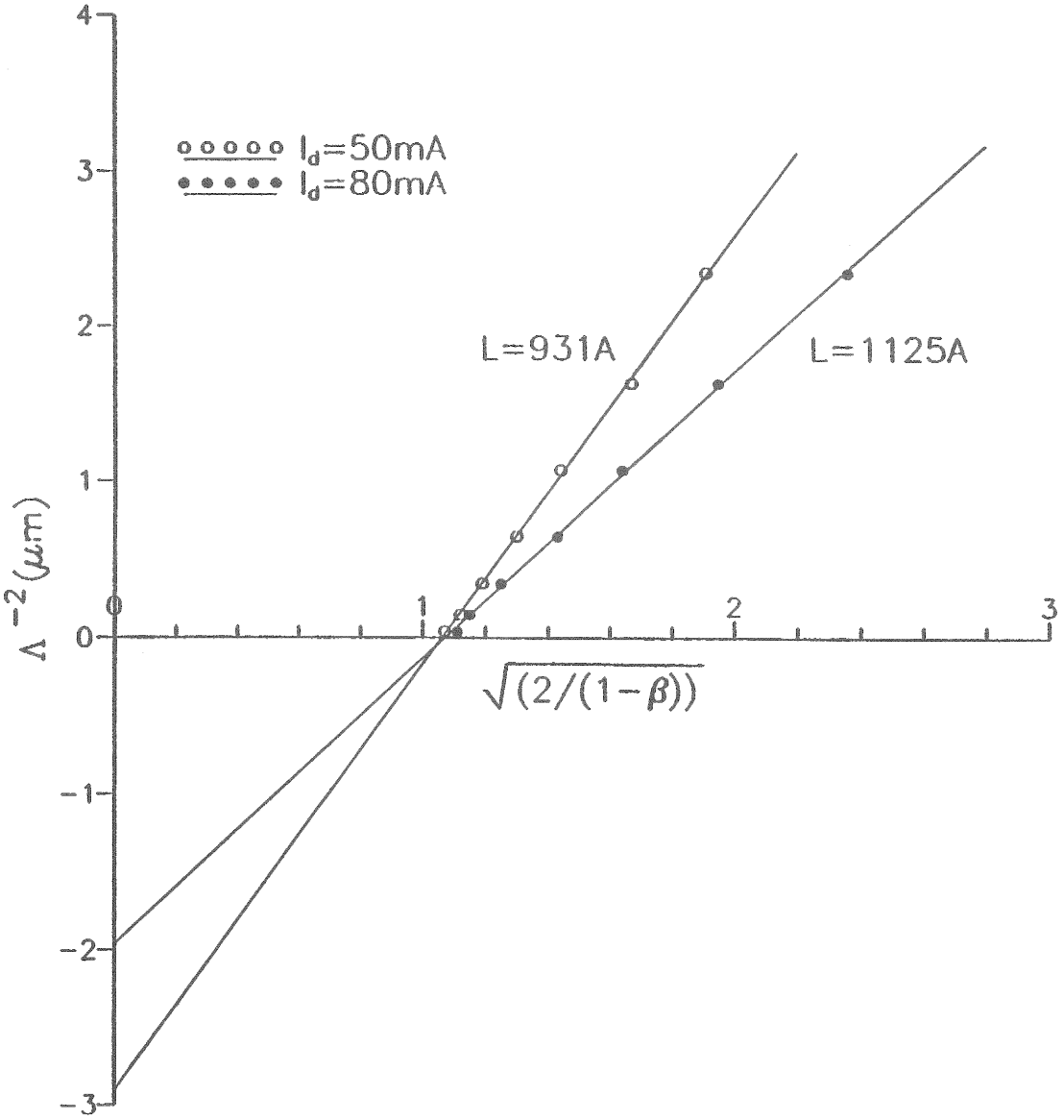

FIGURE 1-7 DIFFUSION LENGTH OF A SERIES OF a-SiGe FILMS AS A FUNCTION OF GERMANE FRACTION IN THE FILM.

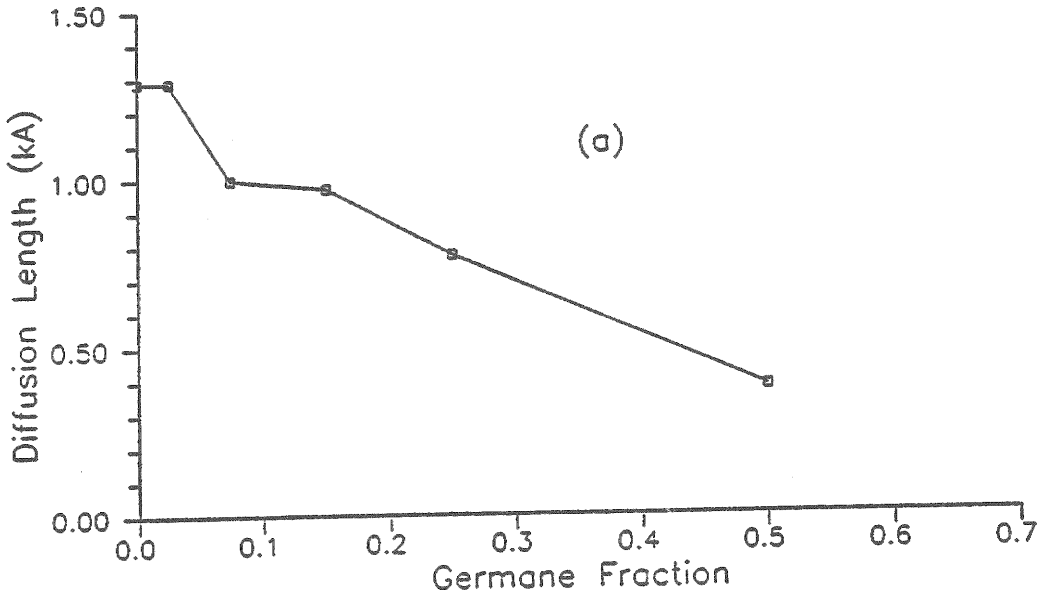

FIGURE 1 - 8 OPTICAL BANDGAP OF THE FILMS IN FIG. 1-7 AS A FUNCTION OF GERMANE FRACTION IN THE FILM.

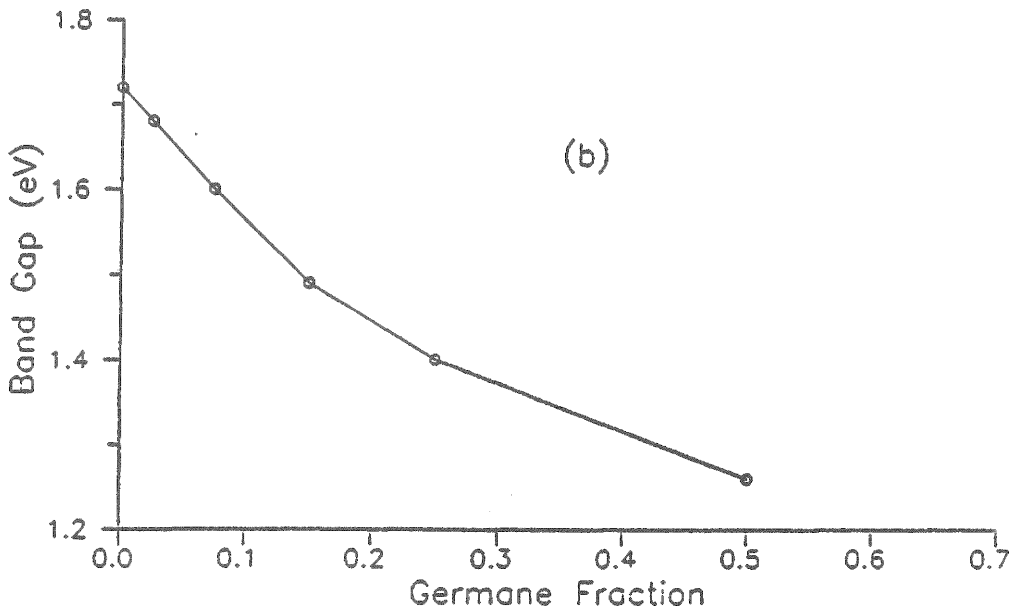

FIGURE 1-9 LIGHT INTENSITY DEPENDENCE OF AMBIPOLAR DIFFUSION LENGTH.

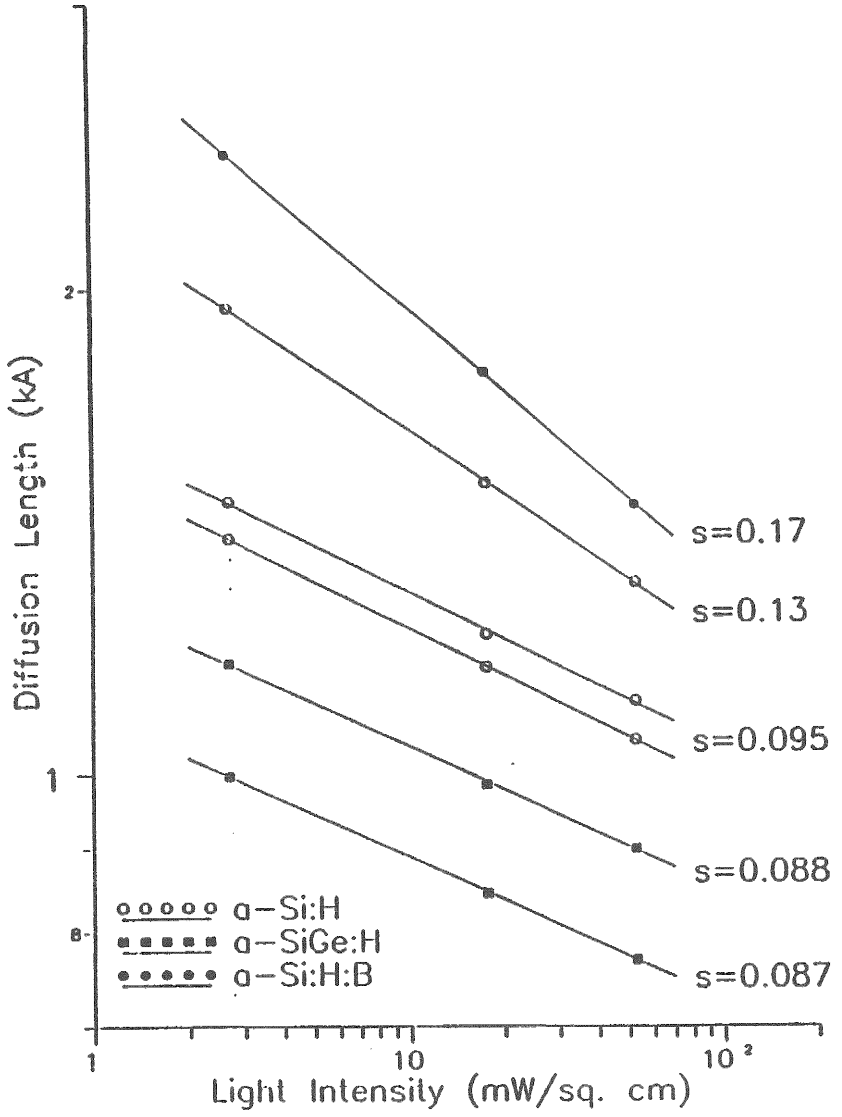

FIGURE 1-10 (A) DIFFUSION LENGTH OF a-Si:H FILMS AS A FUNCTION OF LOW-LEVEL BORON DOPING. (B) DIFFUSION LENGTH OF a-SiGe FILMS AS A FUNCTION OF LOW-LEVEL BORON DOPING.

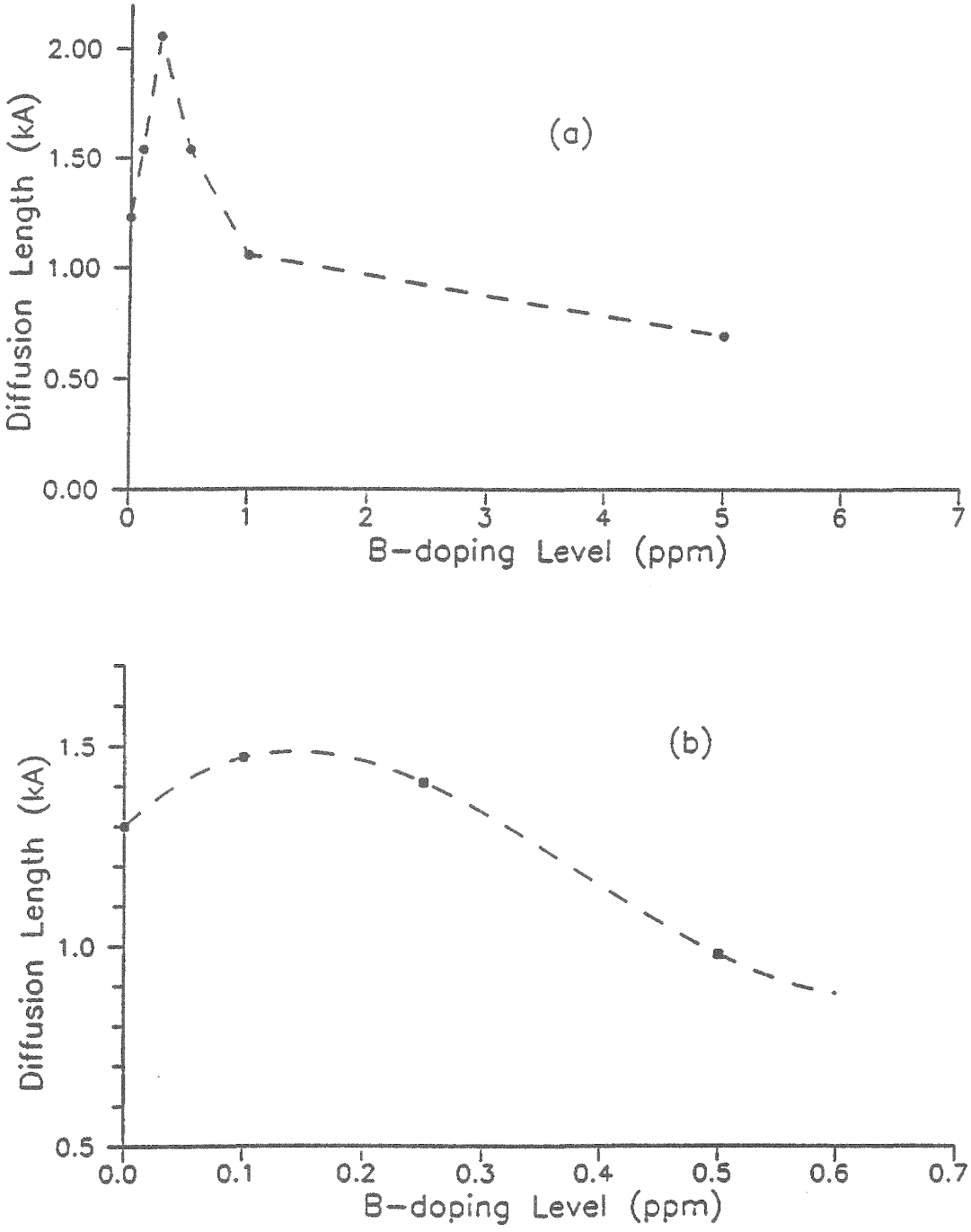

FIGURE 1-11 NORMALIZED DIFFUSION LENGTH L/L_0 AS A FUNCTION OF HOURS OF LIGHT SOAKING.

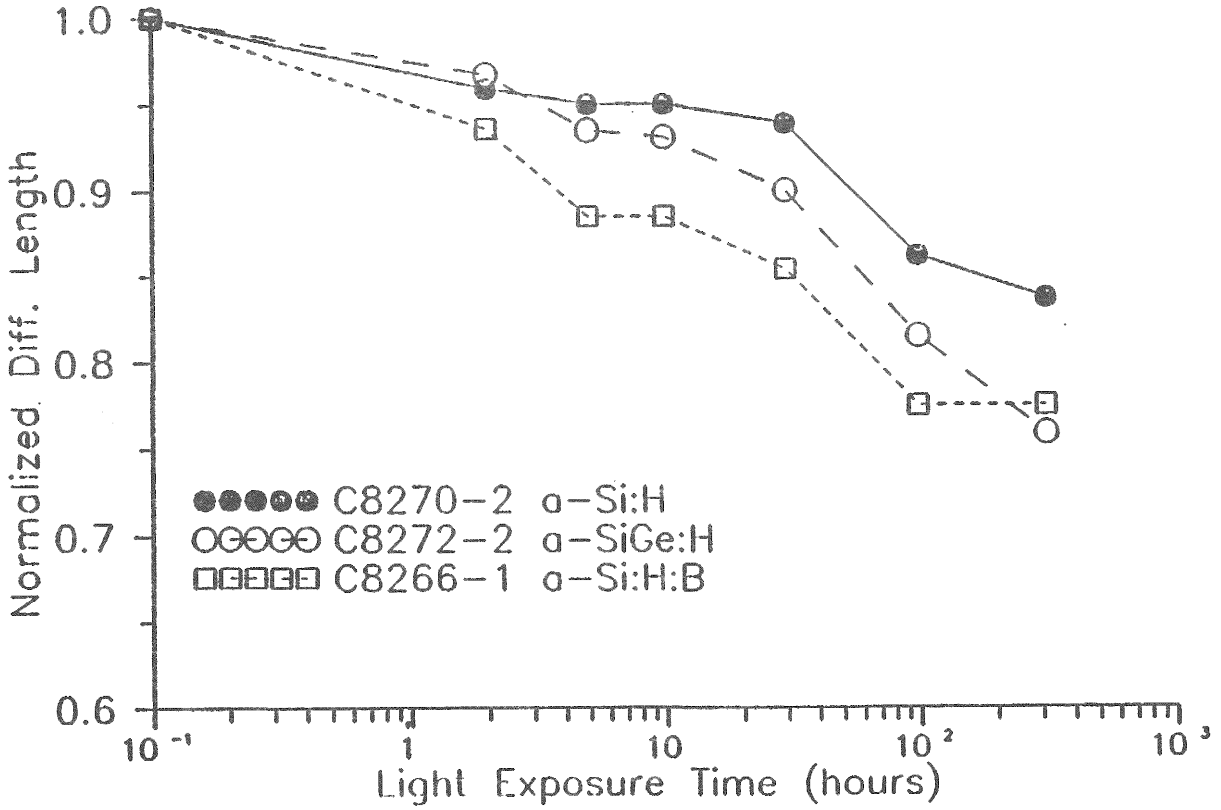

degrade less than a-SiGe:H with E_g = 1.6eV. The trace boron-doped a-Si:H, which had a larger initial diffusion length as shown in Figure 1-10(b), degraded the most. These samples are currently being further light soaked and their degradations are being monitored. Careful comparison of the degradation of diffusion length with that of solar cell parameters such as efficiency and fill factor will be made and their relationship will be explored.

In conclusion, we have investigated the use of ambipolar diffusion length measurements by SSPG technique as a new characterization tool for material studies. It has been shown that the technique is reliable and sensitive, and it correlates well with solar cell performance. The applications of this technique in areas such as SiGe alloy materials, low-level boron doping and light degradation have been explored.

1.5 RAMAN SPECTROSCOPY OF ALLOYS

We continue to use Raman spectroscopy to study the microscopic bonding structure in a-SiGe alloys. Preliminary results were summarized in the Semi-Annual report.

The basic approach we are taking is to use characteristic Raman scattering peaks for different types of bonding present in the alloys, i.e., Si-Si, Si-Ge and Ge-Ge as measures of densities of each respective type of bonds. Then we compare the measured bond densities, or more precisely, the density ratios of different types of bonds with those expected for a homogeneous alloy in which bonds are randomly distributed. If the measured values deviate from the random distribution, it indicates that preferential bonding takes place in a real alloy which might be significant source of damage to the optoelectronic properties of such an alloy. In fact, a number of researchers have long speculated the presence of Ge-Ge clustering in this alloy material based on the fact that germane decomposes much more readily than silane does and also on evidences from several transport as well as microscopy measurements. In this study, however, we use Raman as a microscopic probe to search for direct evidence of this effect.

We have measured Raman spectra of a series of a-$Si_{1-x}Ge_x$:H alloy films made by dc glow discharge of mixture of silane and germane. The spectra were decomposed into three distinctive peaks at 480cm^{-1}, 365cm^{-1} and 265cm^{-1}, corresponding to Si-Si, Si-Ge and Ge-Ge bonding respectively. Since the absolute magnitude of a Raman spectrum is meaningless, i.e., it depends on many uncontrollable experimental factors such as surface roughness, we used the ratios of integrated Raman intensities as measures of relative population of different types of bonds. In order to find if Ge-Ge bonding is more favored than Si-Ge bonding, we compared our measured ratio, I_{Ge-Ge}/I_{Si-Ge}, as a function of Ge concentration x with the density ratio of Ge-Ge bonds to Si-Ge bonds, $x/2(1-x)$, of an ideal randomly mixed alloy.

Assuming that at large Ge concentrations, e.g., x~0.8, real alloys are close to the randomly mixed state, we can normalize our measured ratios to the theoretical values by those at high concentrations. What came out immediately from this comparison was that the measured Raman intensity ratio, I_{Ge-Ge}/I_{Si-Ge}, for all samples with $0.10<x<0.50$ were significantly larger than those predicted by the random mixing model. This indicates that Raman experiments do support the Ge clustering model. By further using the difference between measured and predicted ratios and assuming that all Ge atoms form equally sized clusters, we estimated that in an a-SiGe alloy with x~0.11, an average cluster may contain as many as four Ge atoms. With increasing Ge concentration x, the relative deviation of the measured ratio from that of a random alloy became smaller due to the increasing fraction of Ge-Ge bonds originating from a random distribution. Thus, it is no longer appropriate to assume that all Ge atoms are involved in clustering at high Ge concentrations and make a similar estimate for the average cluster size as we did for x~0.11. Nevertheless, it is still significant that with Ge concentration x up to 0.5 the observed fraction of Ge-Ge bonds is in far excess of that predicted for an ideal alloy. This information about bonding structure of the SiGe alloy will hopefully assist us in the process of finding better alloy materials.

1.6 ADVANCED FEEDSTOCK RESEARCH

The p-layer in a p-i-n photovoltaic cell performs a variety of optical and electrical functions that directly affect cell efficiency. To improve the performance of the p-layer in cells, the compound trimethylboron ($B(CH_3)_3$) was investigated as an alternative boron source to replace diborane (B_2H_6). Trimethylboron is a monomeric boron containing compound which is reported to give an amorphous silicon film with a lower concentration of unfavorable boron-boron bonds than diborane. Trimethylboron is more thermally stable than diborane and thus is easier to handle during deposition studies. The goal of the work is to show that the different structure of trimethylboron leads to a different deposition chemistry that improves p-layer film properties.

An initial small scale preparation of $B(CH_3)_3$ was undertaken to make a gram of material using the following synthetic route:

$$Al(CH_3)_3 + B(OCH_3)_3 \text{ ----> } B(CH_3) + (Al(OCH_3)_3)_n$$

Using a standard vacuum line and glassware to prepare this air sensitive compound, the synthesis was successfully scaled up to yield over six grams of product. There appears to be no factor that would limit further scale up. The synthesis and purification gave product in about 50% yield and 99% purity. After distillation and further purification the product was 99.6% pure as determined by gas chromatography/mass spectroscopy. The $B(CH_3)_3$ was diluted to a concentration of 1-5% in silane for depositions.

A series of 1000-5000Å thick boron doped amorphous silicon layers were deposited using a DC glow discharge. The films were then analyzed to obtain Tauc bandgaps and conductivity, and the results were plotted to highlight the important optical and electrical properties of the material. On selected films PDS and SIMS analyses were carried out. The results from the materials studies were then incorporated into the construction of photovoltaic cells.

Figure 1-12 plots the bandgap (X-axis) and the conductivity (Y-axis) as a function of boron in the feed gas. As a reference point, typical p-layer material has a bandgap of around 2.0eV and a conductivity of $10^{-6}(ohm\text{-}cm)^{-1}$. The plot confirms that diborane and trimethylboron have the same effect as p-dopants. Increasing the boron concentration increases the conductivity. At higher boron concentrations the bandgaps shows a significant decrease as boron become a major component in the film. It is also clear that the methyl groups on the trimethylboron contribute less than a 0.01eV increase in bandgap.

Because the p-layer in a p-i-n photovoltaic cell must also function as a window to allow light into the i-layer, carbon in the form of methane is added to the deposition. Figure 1-13 shows the variation in conductivity and bandgap of films deposited with more methane in the feed gas while the amount of trimethylboron was kept constant. Figures 1-12 and 1-13 point out the inherent compromise that is necessary in cell preparation. Adding trimethylboron decreases the bandgap and increases the conductivity. Adding carbon increases the bandgap and decreases the conductivity. The optimum cell performance will be found where the p-layer has enough carbon and boron to increase the bandgap without significantly reducing the p-layer conductivity.

The results of materials studies indicate that under typical cell deposition conditions there is no apparent difference between using trimethylboron or diborane in the p-layer. By solely adjusting flow rates of methane and of trimethylboron it was not possible to improve over the p-layer material obtained with diborane as the boron source.

However, when the deposition current was reduced to one quarter that normally used, it was possible to observe significant improvements in the p-type material. Figure 1-14 clearly demonstrates that at lower current it is possible to obtain materials with similar conductivities but with a bandgap of 2.15eV versus 1.98eV for

FIGURE 1-12 EFFECT OF DOPING DIBORANE AND TRIMETHYLBORON INTO AMORPHOUS SILICON ON THE CONDUCTIVITY AND TAUC BANDGAP.

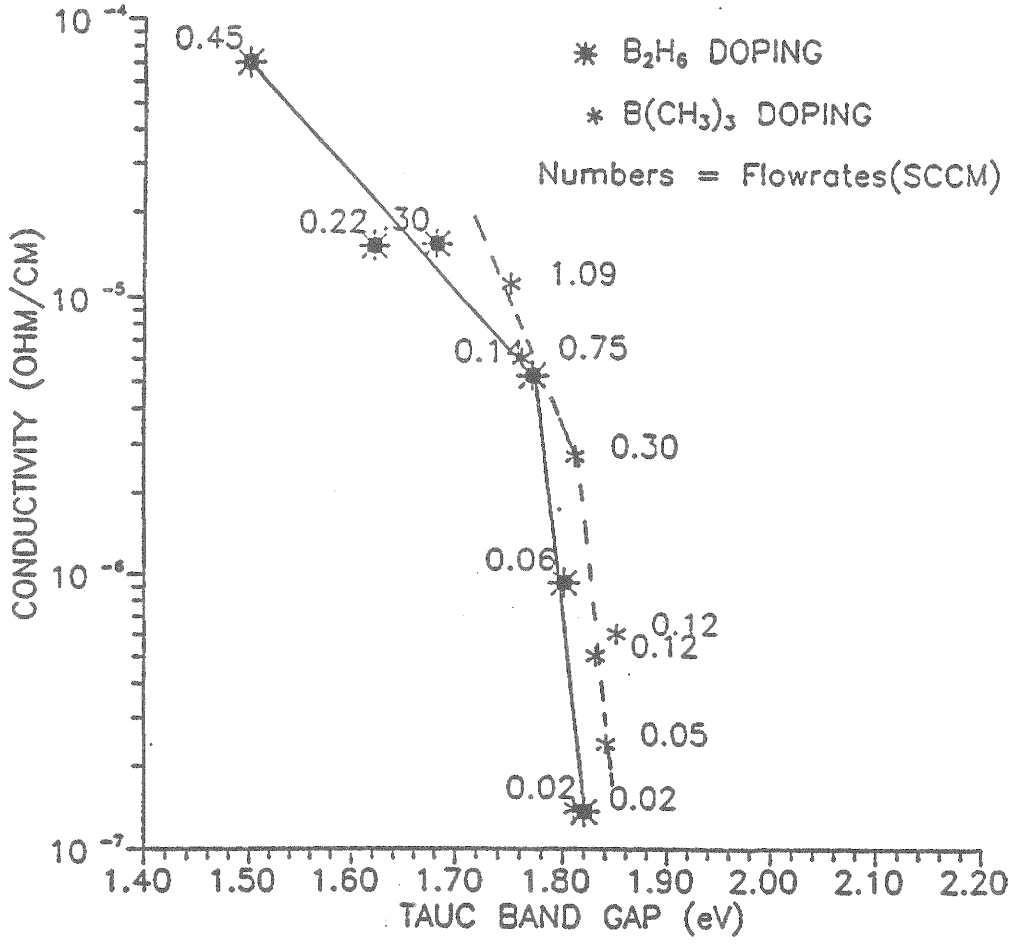

FIGURE 1-13 EFFECT OF ADDING DIFFERENT AMOUNTS OF METHANE TO FORM AN a-Si/C ALLOY WHEN THE TRIMETHYLBORON:AND SILANE FLOWS ARE HELD CONSTANT.

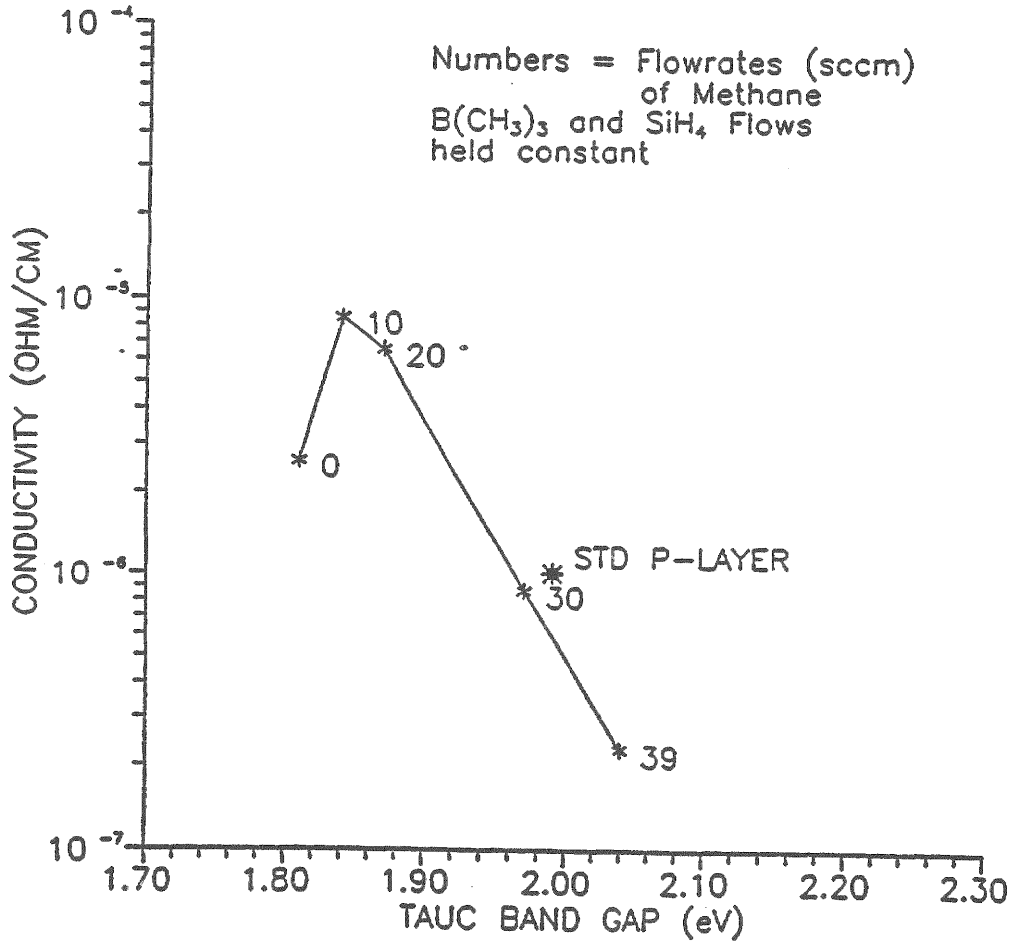

FIGURE 1-14 EFFECT OF ADDING TRIMETHYLBORON AS A DOPANT INTO AMORPHOUS SILICON WHEN THE SILANE AND METHANE FLOW RATES ARE HELD CONSTANT.

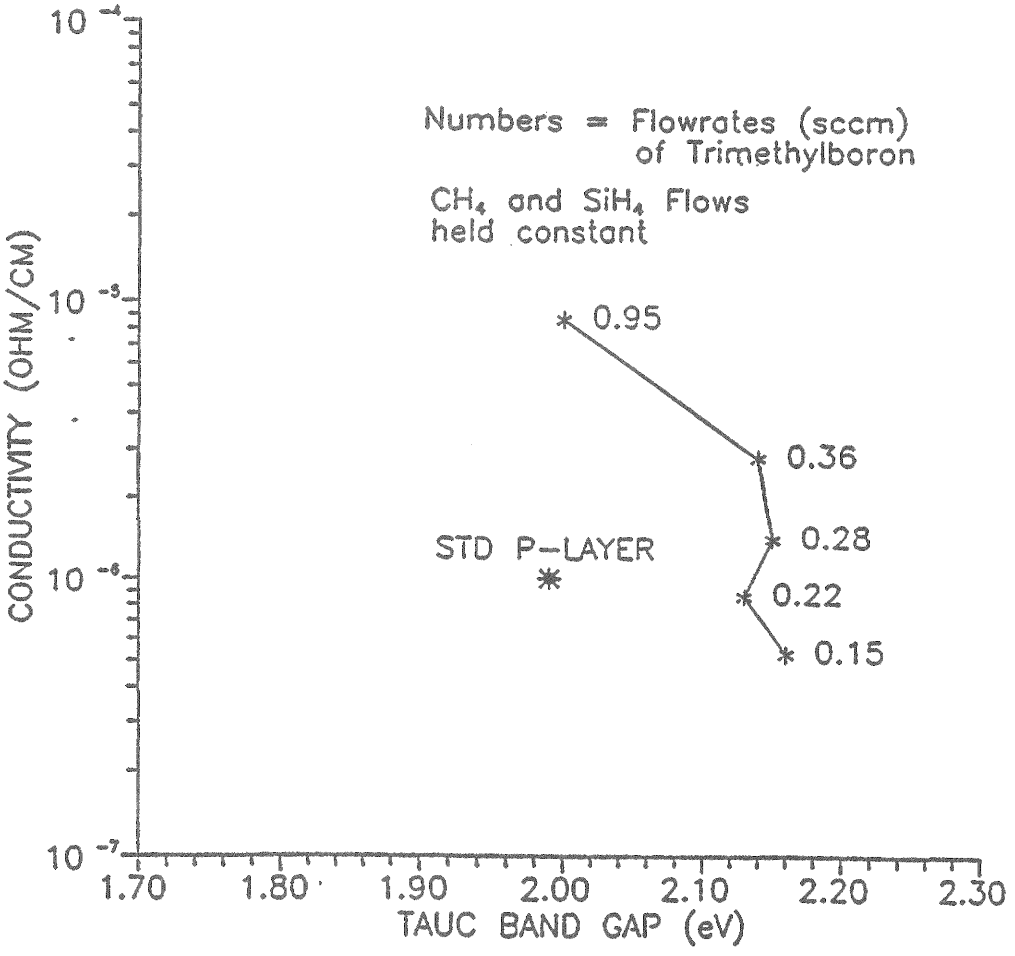

typical p-layers. It is worth noting that films deposited with diborane also showed an increase in bandgap with similar conductivities. However, the increase in bandgap is about half that observed at similar conductivities with trimethylboron.

The differences in materials deposited with trimethylboron or diborane at low and high currents is most clearly observed in the PDS shown in Figures 1-15 and 1-16. For the two boron (from $B(CH_3)_3$)) doped a-SiC films shown in Figure 1-15, the samples deposited at low current show a greatly reduced, defect density of midgap states compared with a similar deposition at higher currents. Figure 1-16 compares the PDS spectra for typical p-layers using diborane as the boron source at high current and a similar deposition run at low current. The two curves are similar at low energies.

Several of the films have been sent for SIMS analyses and the results are being awaited. Fabrication of cells employing $B(CH_3)_3$ doped p-layers is underway and shall be reported upon in the next Semi-Annual report.

1.7 MICROCRYSTALLINE p+ SiC:H RESEARCH

During the period covered by this report the characterization of p+ microcrystalline SiC:H layers was expanded, and, at the same time, attempts to improve solar cell performance through the incorporation of such layers into solar cells was vigorously pursued. The significant results of these efforts are summarized and briefly discussed in thsi section.

1.7.1 Microcrystalline p+ SiC:H layers by RF

A series of experiments was performed to compare methane and disilylmethane in the preparation of microcrystalline p+ material. It was found that using the same hydrogen-diluted, RF, high power glow discharge, microcrystalline p+ SiC can be made using methane except that more carbon can be incorporated into microcrystalline film using disilylmethane before the microcrystallinity is suppressed. Where relatively high-conductivity, partially microcrystalline films containing up to 6% carbon can be made with DSM such films can be made with only 3-4% C when CH_4 is used as the feedstock. It is speculated that this may be due to the fact that the feedstock molecule already contains bonded C and Si for the case of DSM, and can thus be more effectively incorporated into the lattice with less bond-breaking.

A model for the deposition of microcrystalline Si:H has been proposed by Veprek which involves, among other things, the beneficial presence of H atoms on the substrate and then subsequently on the grown layer, which aids and abets the nucleation of crystallites by bringing the growth of layers closer to chemical equilibrium with the depositing vapor. We suggest that this might explain why microcrystalline material deposits on α-Si:H, but not on CTO (or any other known oxide), see Figure 2-40 of 1987 Annual Report.

Since the only substrate on which we have been able to grown microcrystalline p+ SiC:H is amorphous Si:H, we have interposed an amorphous layer of SiC:H (10% C) ~100-150Å thick between the CTO and the p+ microcrystalline layer in our test solar cell structures. Our success in growing such structures is directly demonstrated by the Transmission Electron Micrograph, shown in Figuere 1-17, of a section of such a structure taken by P. Hruskoci at Amoco's corporate research facility, Naperville, Illinois. Magnification is 185,000. Clearly evident are the CTO, α-SiC:H, μc-p+ SiC:H, i-layer (α-Si:H), and μc-n+ SiC:H. Grain size in the microcrystalline layers is 50-100Å in agreement with values calculated from the Raman data (see earlier reports). It is clear that the degree of microcrystallinity is considerably better for the n+ layer than for the p+ layer. This is most likely due to the (apparently) well-known crystallization-enhancing action of phosphorous. Accordingly, we have attempted to improve the microcrystalline quality of the p+ layer, all the while looking for some significant improvement in cell performance that would reflect the superior electrical properties of microcrystalline p+ material. We have counterdoped the p+ layer with phosphorus (while, of course, keeping its level below that of B). We have increased the levels of both B and P in the p+ layer to help initial

FIGURE 1-15 PDS OF p-LAYERS MADE WITH $B(CH_3)_3$ AND SiH_4 UNDER LOW AND HIGH CURRENTS.

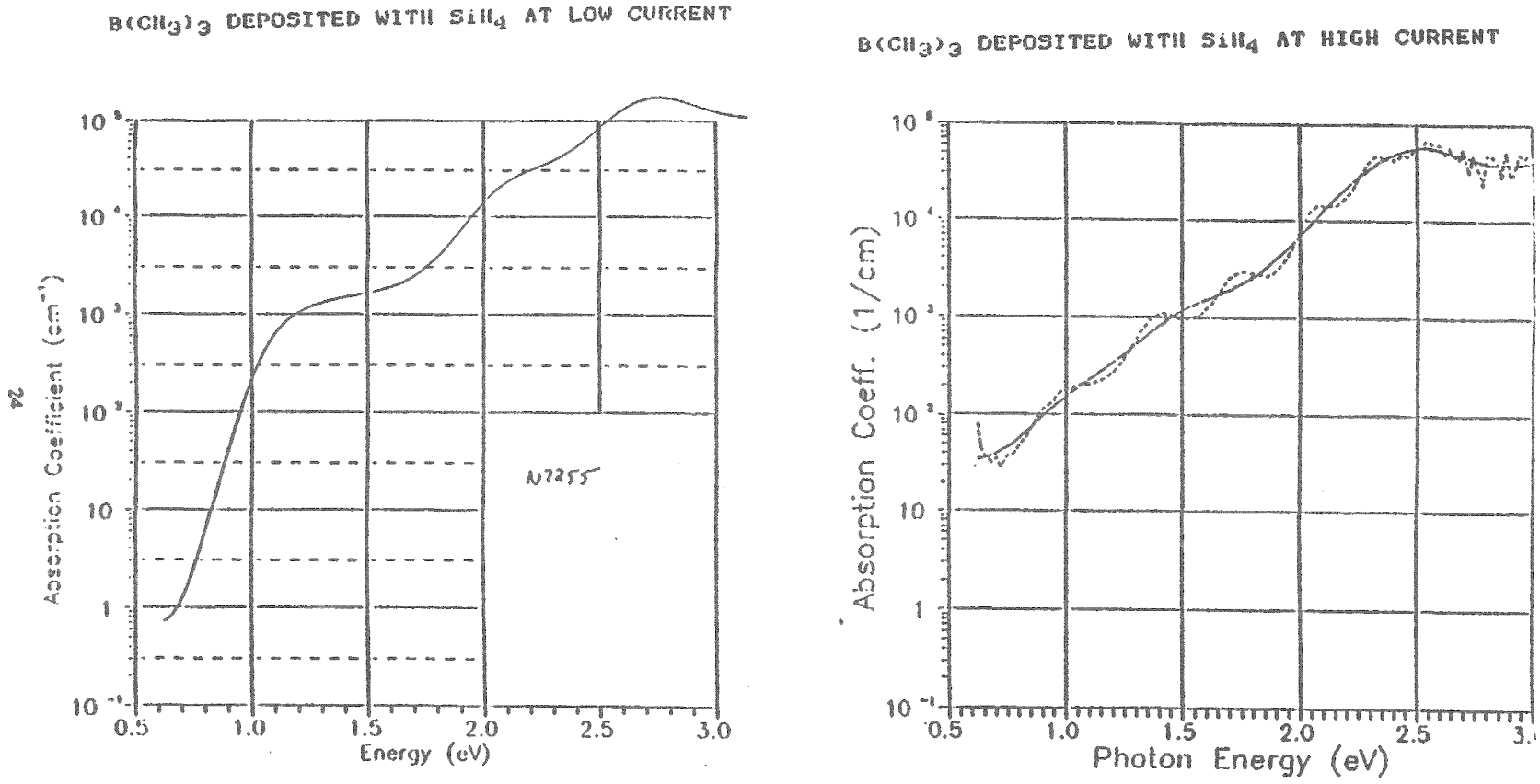

FIGURE 1-16 PDS OF p-LAYERS MADE WITH B_2H_6 AND SiH_4 UNDER LOW AND HIGH CURRENTS.

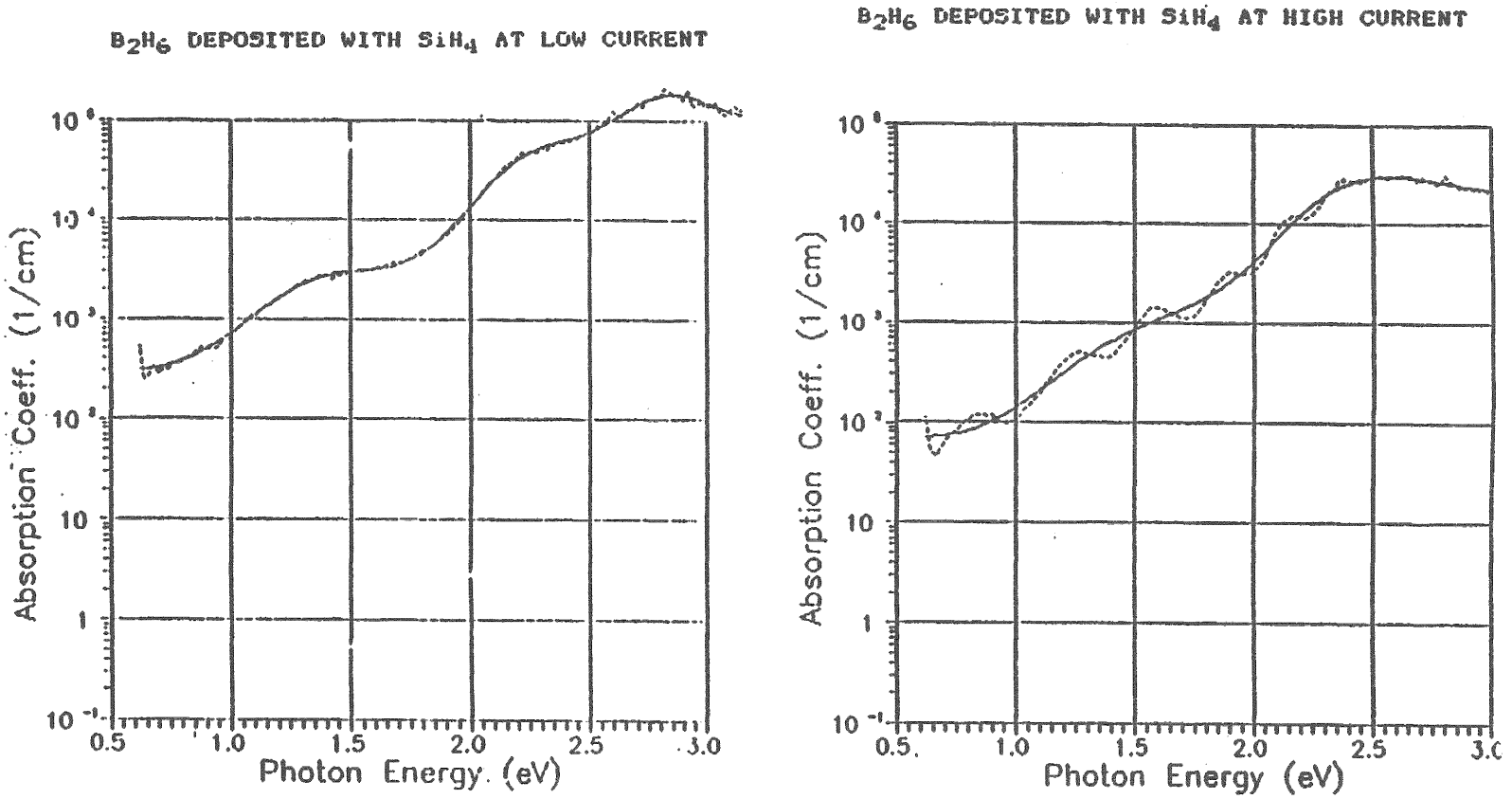

FIGURE 1-17 TEM PHOTOGRAPH OF A MICROCRYSTALLINE p-i-MICROCRYSTALLINE n SOLAR CELL.

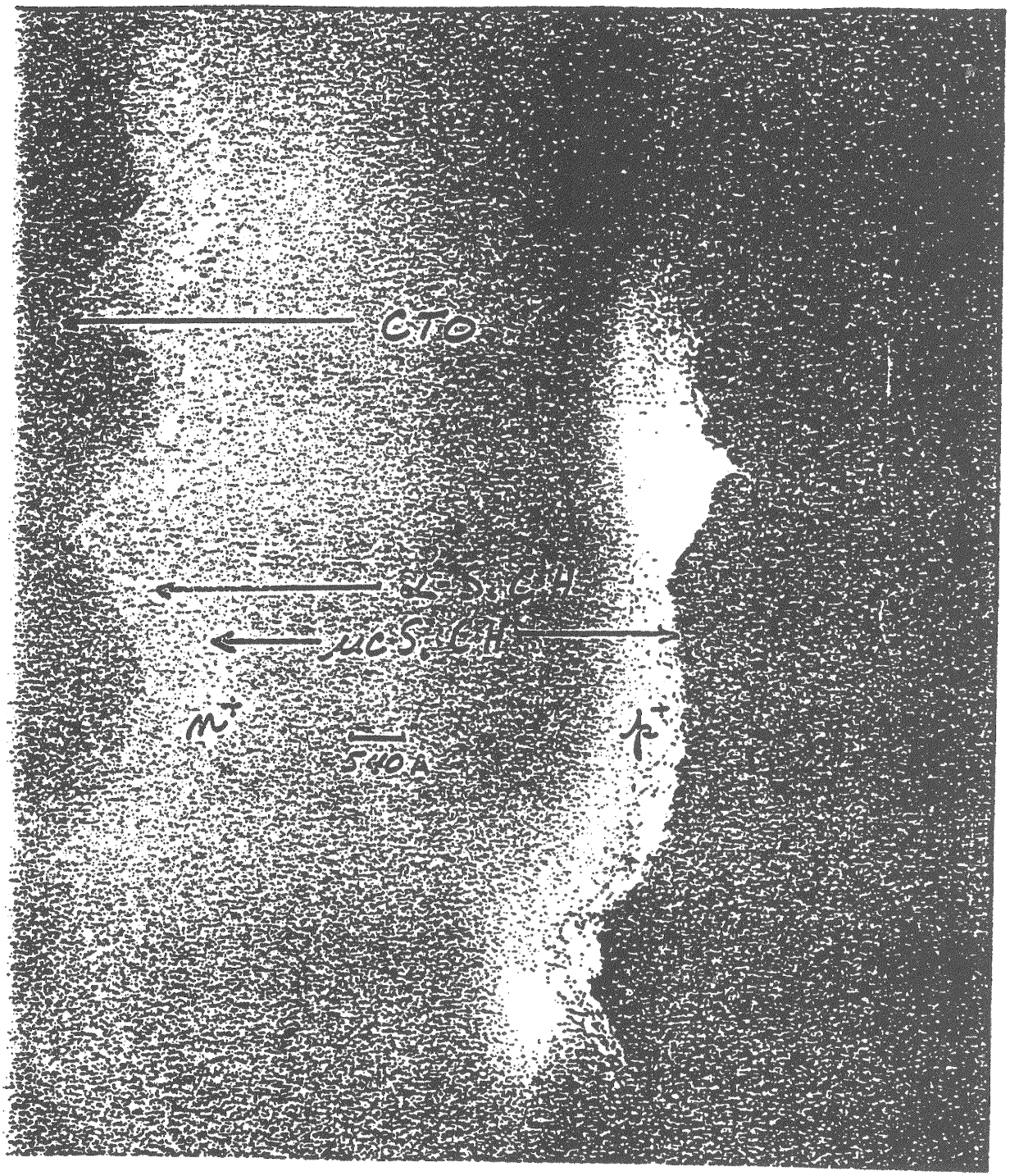

nucleation. We have increased the H_2 dilution in the discharge. We have interposed a 30-50Å thick (tunnelable) phosphorus-doped microcrystalline layer to act as a seed bed for the p+ layer. We have even made a series of n-i-μc-p structures (in which the μc-p+ layer grows on ~5000Å of amorphous i-material) using both Al and ITO as contacts. All to no avail. While evidence remains strong that we are indeed making microcrystalline layers, no worthwhile improvement in any solar cell property reflecting the action of microcrystalline layers has yet been observed. Such an improvement would be, for example, a V_{oc} of 0.95-1.0V.

In addition to our attempts to incorporate the desirable action of μc-p+ layers into solar cells as described above, basic p-i-n cell structures were grown that included bandgap grading between the μc-p+ layer and the i-layer in order to minimize interfacial recombination from possibly limiting V_{oc}. In the graded case V_{oc} increased significantly over that of the ungraded reference; maximum values of 0.88V were reached, but such values are really no better than those occasionally achieved with grading using amorphous SiC layers. Furthermore, evidence is accumulating that the combination of necessary buffer layer and thicker-than-usual μc-p+ layer may (even with wide bandgaps) be significantly reducing J_{sc}.

In summary, after some considerable effort we have yet to observe any indication of significantly improved solar cell performance through the incorporation of microcrystalline doped layers grown during the fabrication of traditional p-i-n structures.

1.7.2 Thermal recrystallization of p+ a-SiC:H films

Several means to produce highly conductive, p+ type, microcrystalline SiC were explored, including direct deposition using hydrogen dilution in a DC plasma from methylsilane and B_2H_6/SiH_4, directly from Dimethylsilane and B_2H_6/SiH_4, and indirectly by high temperature recrystallization of SiC films made by the direct processes. Although a wide variety of deposition conditions were used in the direct processes a highly conductive material could not be made. These materials were generally very transparent, some having effective band gaps over 3.0eV and appearing virtually invisible over the quartz substrates. High temperature (600 to 900° C) recrystallization imparted fairly good conductivity to some of these materials (0.28eV conductivity activation energy) (Figure 1-18) with only moderate loss in optical transparency (Figure 1-19), however no process could be found to yield truly microcrystalline SiC, as evidenced by a strong Raman line at 790cm^{-1}. The Raman spectrum typically indicated the dominance of Si-Si (300 - 500cm^{-1})and C-C bonds (1300 - 1500cm^{-1}) over Si-C bonds (600 - 850cm^{-1}) (Figure 1-20) even though Rutherford backscattering and secondary ion mass spectroscopy indicated that nearly stoichiometric SiC had been formed. Other measurements (X-ray photoelectron spectroscopy) confirmed the implication that a substantial amount of the carbon in the material was bonded to other carbon, and not to silicon. The Si-C bonding may be greater than appears from the Raman spectrum, however, because the matrix element governing the Stokes shift process for the Si-C bond is generally thought to be smaller than the comparable probability associated with either the Si-Si or C-C bond. The Raman spectrum is also complicated by a large background level, probably due to photoluminescence in the highly defective, wide bandgap material.

In general proper stoichiometry was more easily obtained using dimethylsilane rather than methylsilane, however the SiC deposited with dimethylsilane suffered from high concentrations of oxygen impurity. The oxygen content in the film was linked to an oxygen containing impurity in the dimethylsilane feedstock, later identified as $(CH_3)_2H\text{-}Si\text{-}O\text{-}Si\text{-}H(CH_3)_2$.

Recrystallization of the film using high temperature exposure subsequent to film deposition also increased the oxygen content of the SiC. This effect persisted at a slower rate even when recrystallization was attempted in a vacuum furnace. Attempts to prevent diffusion of oxygen into the SiC during recrystallization by using a protective overlayer of metal, a-Si or a-Si with metal were unsuccessful because the protective overlayers would not remain intact during the large temperature excursions produced during the recrystallization process.

FIGURE 18 CONDUCTIVITY VS. 1000/T FOR STOICHIOMETRIC SiC AFTER HIGH TEMPERATURE ANNEAL TO PROMOTE RECRYSTALLIZATION. ACTIVATION ENERGY IS 0.28eV.

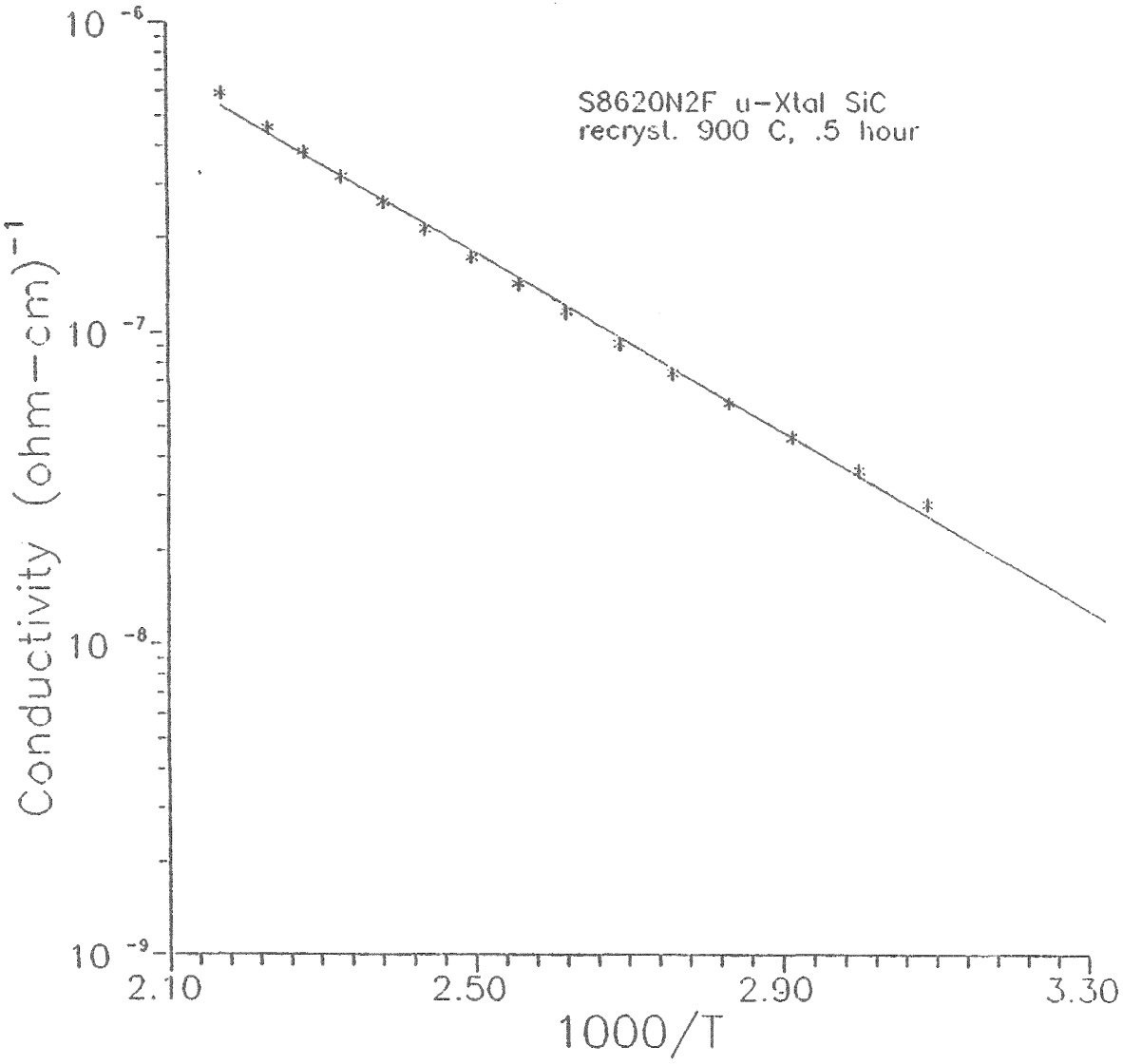

FIGURE 19 OPTICAL TRANSMISSION OF A 4400Å THICKNESS OF STOICHIOMETRIC SiC BEFORE AND AFTER HIGH TEMPERATURE ANNEAL. THE HIGH TEMPERATURE ANNEALS WERE USED TO ATTEMPT RECRYSTALLIZATION OF THE SiC TO MICROCRYSTALLINE SiC.

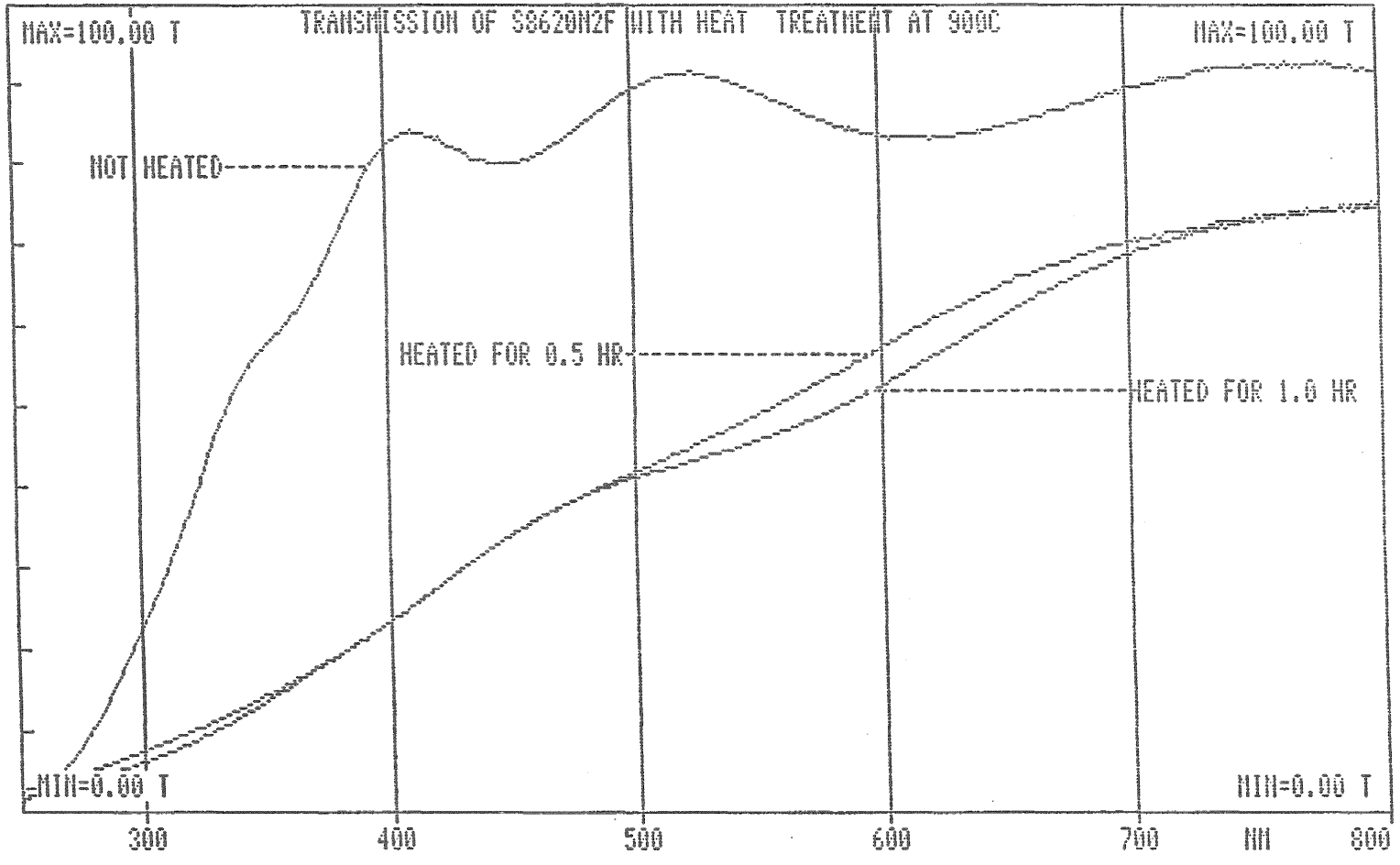

FIGURE 20 RAMAN SPECTRUM TYPICAL OF SiC DEPOSITED UNDER CONDITIONS WHICH ENCOURAGE MICROCRYSTALLINITY

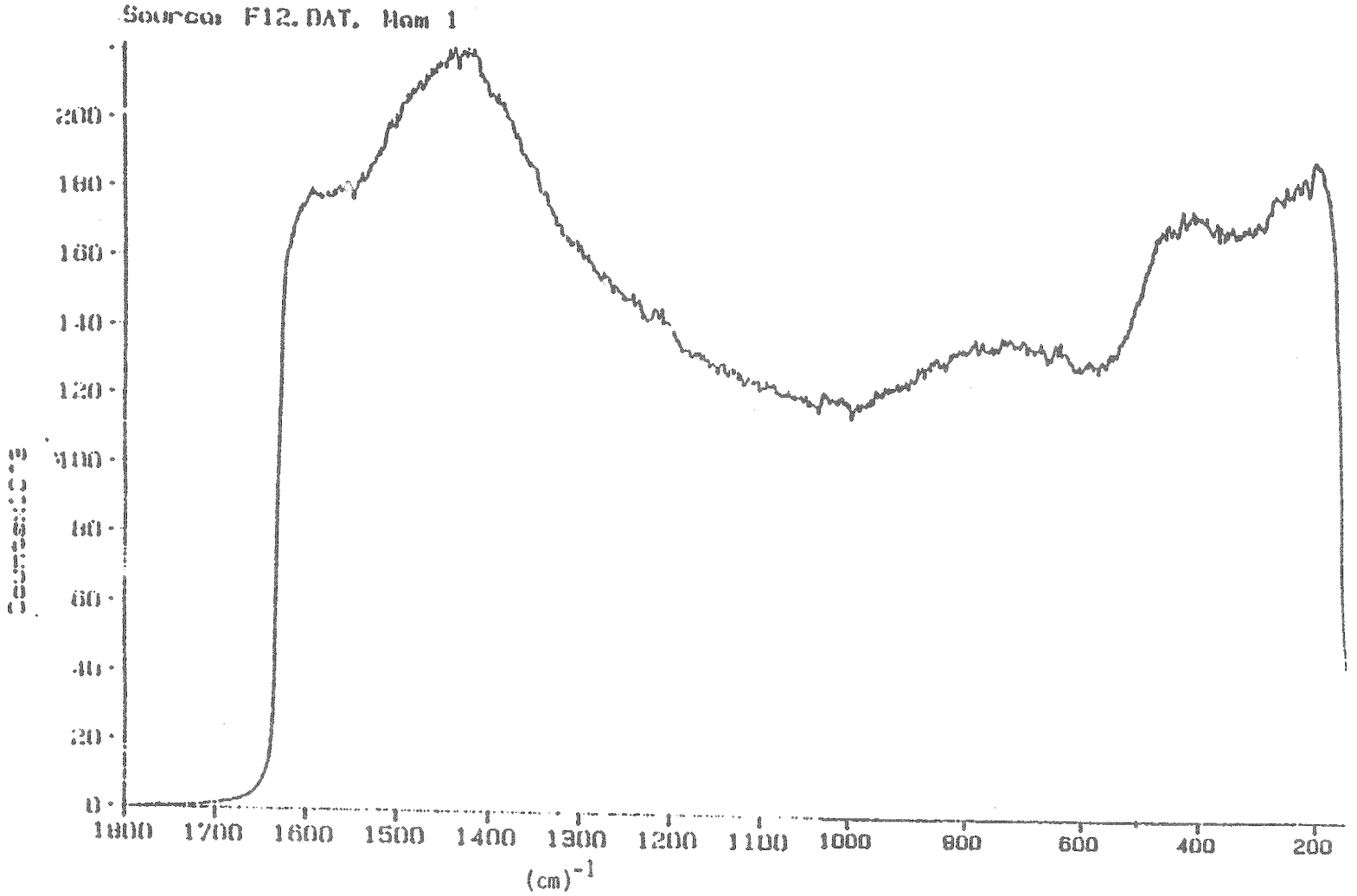

Efforts to produce highly conductive microcrystalline p+ Si in thin (less than 400Å) were successful. This is evidenced by the Raman spectrum (Figure 1-21) of a 180Å thick p+ microcrystalline layer compared to the spectrum of single crystal Si (Figure 1-22) and that of typical boron doped a-Si (Figure 1-23). Unfortunately, the highest degree of crystallinity occurred only when deposited on Nichrome. Identical deposition conditions did not produce material of the same high crystallinity over quartz, possibly due to substrate dependent nucleation differences. It was anticipated that this also occurred over textured ZnO/CTO/glass, thus preventing the desired p-i-n device performance. Because of the difficulty in transferring material (film) properties to device results, research has been emphasized recently which attempts to optimize the microcrystalline p+ layer directly in device studies.

Conventional, PECVD deposition methods have so far not yield highly conducting, p-type SiC films that could be verified as being crystalline by Raman Spectroscopy. Hence, we have looked at an alternative means, laser recrystallization of the amorphous film to provide the necessary electrical and optical properties.

1.7.3 Laser crystallized SiC films

Accordingly, we have recently turned our attention to another approach for introducing microcrystalline layers into a solar cell structure; this centers on the fact that laser-solid interactions are known to recrystallize amorphous or polycrystalline or heavily damaged silicon. The basic idea here is to deposit a layer of amorphous p+ SiC:H on a CTO substrate, recrystallize it by laser irradiation, and then grow the remainder of the cell (i.e., the amorphous i and n layers) onto it. It is worth noting that with this process (1) recrystallization need not be limited to carbon concentrations of less than about 6% as reported earlier, (2) a substrate of amorphous Si:H is not necessary (3) proper choice of laser wavelength can restrict the action of the laser to only silicon, and (4) excimer lasers can produce beams ~0.5-1cm^2 in area. In order to establish whether lasers can indeed convert amorphous p+ SiC:H to microcrystalline material a layer of such material 3000Å thick and containing about 25% carbon (Tauc bandgap 2.57eV) was deposited onto a quartz substrate and then rastered with a beam from a Q-switched Nd-YAG laser, frequency doubled to operate at 5230Å. The beam was ~1mm in diameter, had a power of 0.6W, and was pulsed at 5000Hz. The power density in the beam could be most effectively varied over a broad range by changing the beam focus i.e., diameter. Figure 1-24a is a Raman scattering spectrum of an unirradiated portion of the film showing the typical broad peak of amorphous silicon at about 476cm^{-1}; Figure 1-24b is such a spectrum from an adjacent area that had been laser-irradiated, showing the characteristic shifted and narrower peak of microcrystalline silicon at about 518cm^{-1}. Note that Figure 1-24b has no sign of an amorphous silicon shoulder in the spectrum, indicating at least 95% conversion to microcrystalline. So far, only the Si-Si vibration peak has been detected in the Raman spectrum; no Si-C line has yet been observed. The next series of measurements will entail conductivity and optical property changes.

Progress was made in our understanding of the annealing effect reported earlier in which both the resistivity and Fermi-level of μc-p+ layers deposited at low temperature decreased markedly upon annealing at 225° C. (1) It was determined that the deposition temperature has to be below 125° C for the effect to be observed and (2) the IR vibrational spectrum for these low temperature films contains no sign of the CH_3 radical, while after annealing both the rocking and bending modes of CH_3 attached to silicon are clearly seen, see Figure 1-25. (Films deposited above 125° C show the modes associated with CH_3 without subsequent annealing.) Bearing in mind that the total hydrogen content actually increases as the deposition temperature decreases, we suggest that hydrogen appears to be the common factor between the formation of the Si-CH_3 complex and, through its interaction with dangling bond states and boron, the increases in B doping efficiency indicated by the effect. We suggest that at low temperature the hydrogen has not yet either complexed with carbon or interacted with

FIGURE 21 RAMAN SPECTROSCOPY RESULTS SHOWING HIGH DEGREE OF MICROCRYSTALLINITY (NARROW LINE WIDTH) FOR A THIN LAYER OF p+ MICROCRYSTALLINE Si (COMPARE TO FIG. 1.2.6-6.

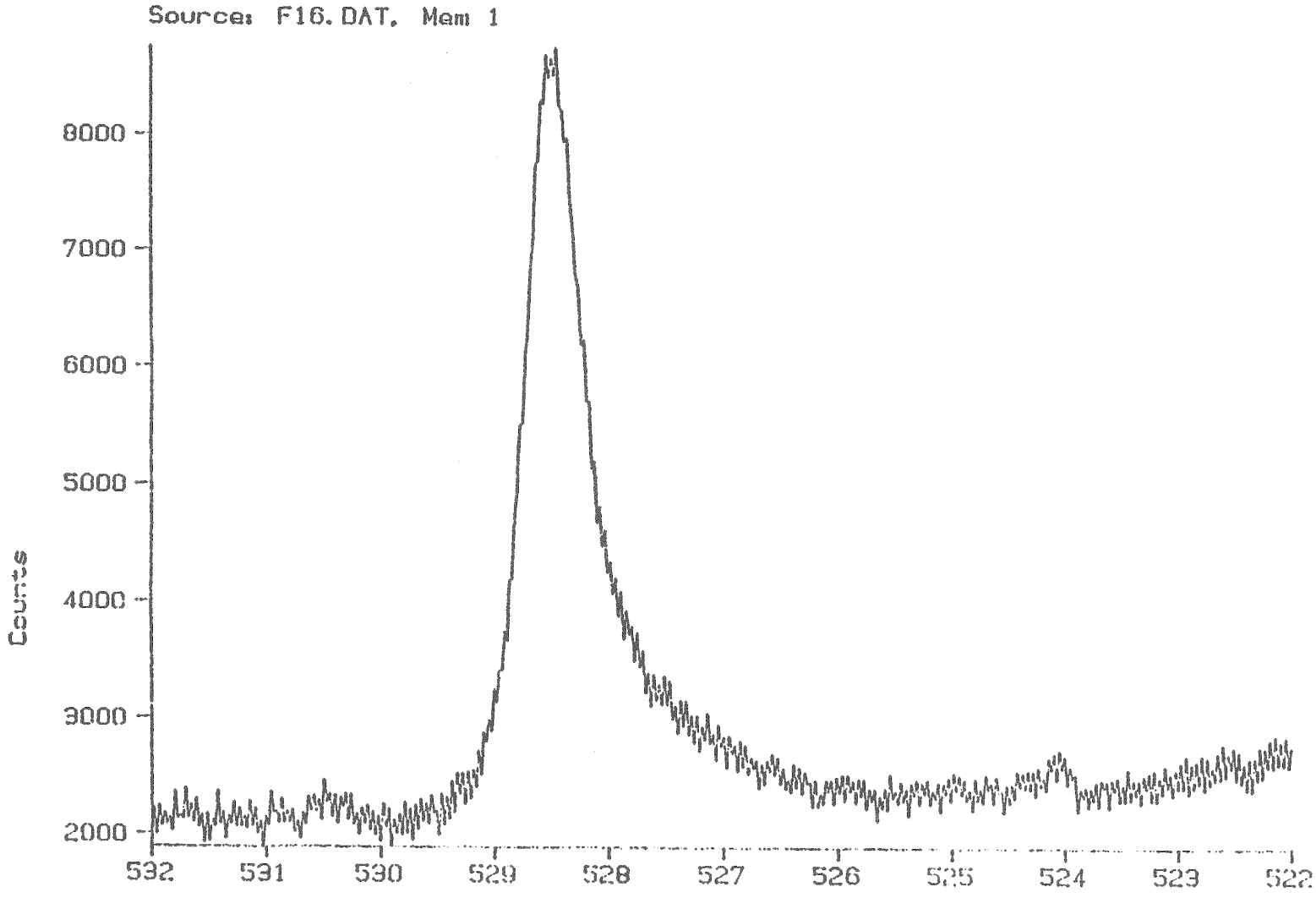

FIGURE 22 RAMAN SPECTROSCOPY RESULT FOR PURE CRYSTALLINE Si (WAFER) ON SAME SCALE AS FIGS. 20 & 21

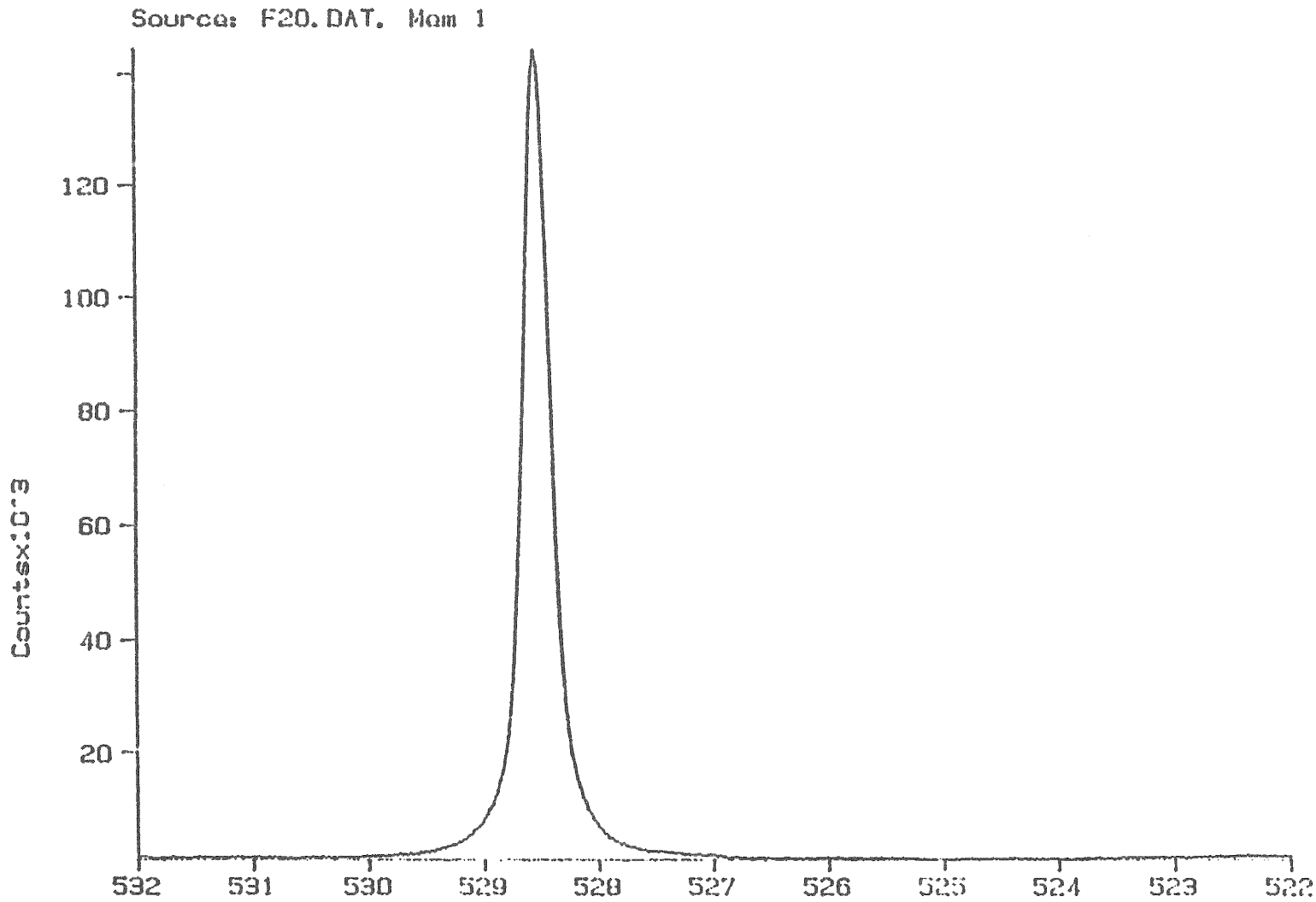

FIGURE 23 TYPICAL RAMAN SPECTRUM FOR p+ a-Si.

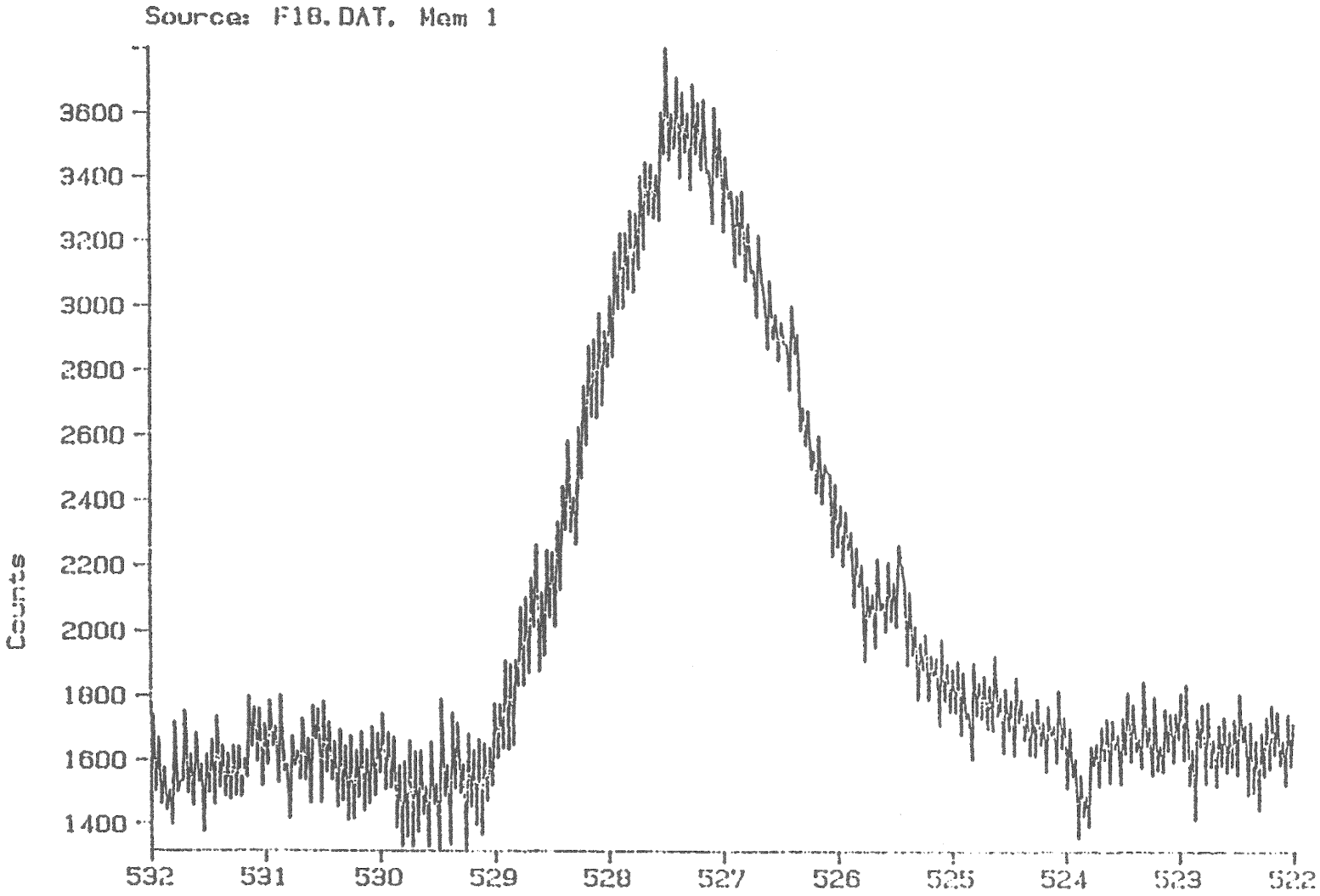

FIGURE 24 (A) RAMAN SPECTRA OF UNIRRADIATED a-Si:H FILM. (B) RAMAN SPECTRA AFTER LASER IRRADIATION.

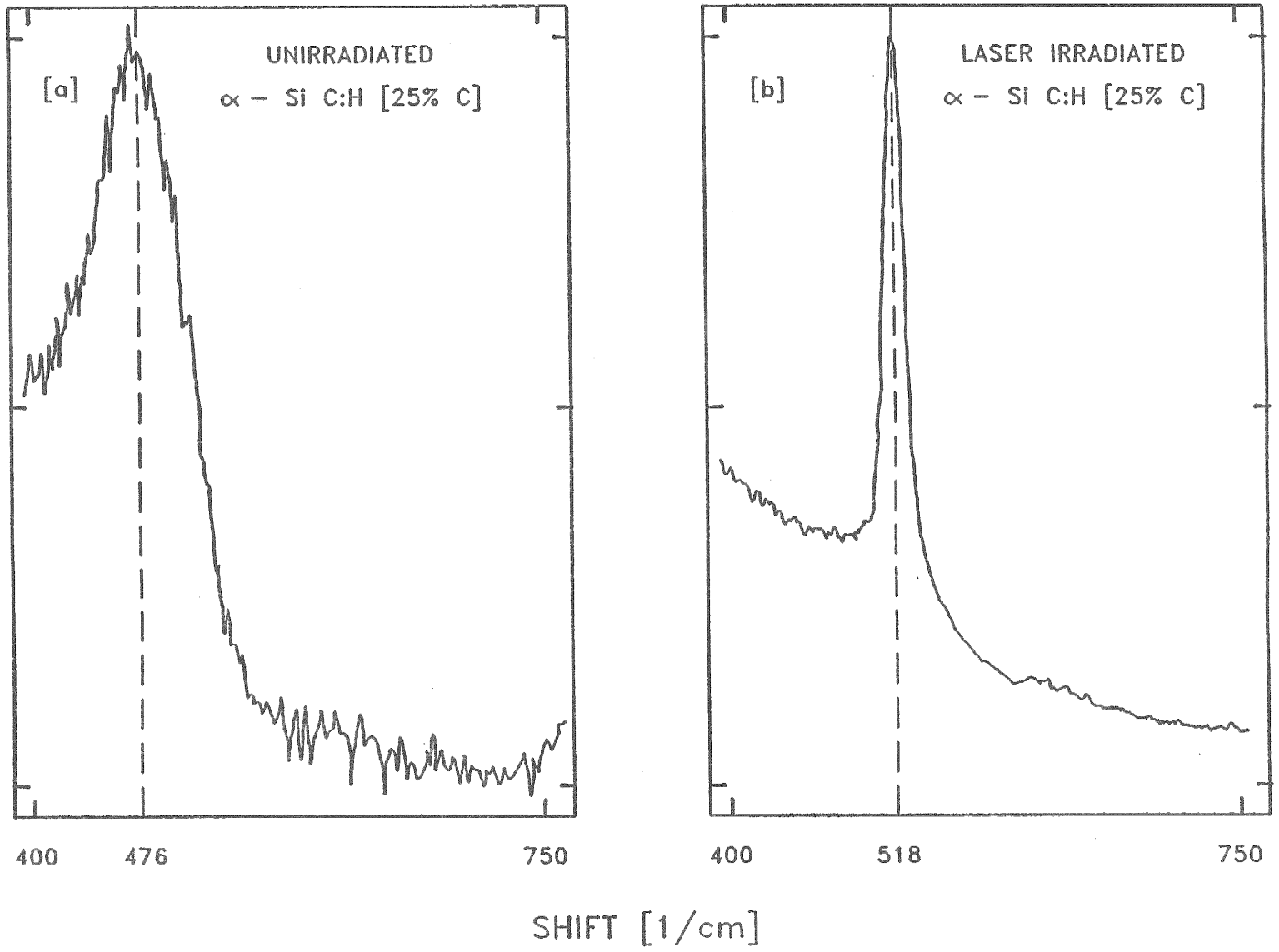

FIGURE 25 IR SPECTRA OF MICROCRYSTALLINE p+ FILMS (A) AS DEPOSITED (B) AFTER ANNEALING.

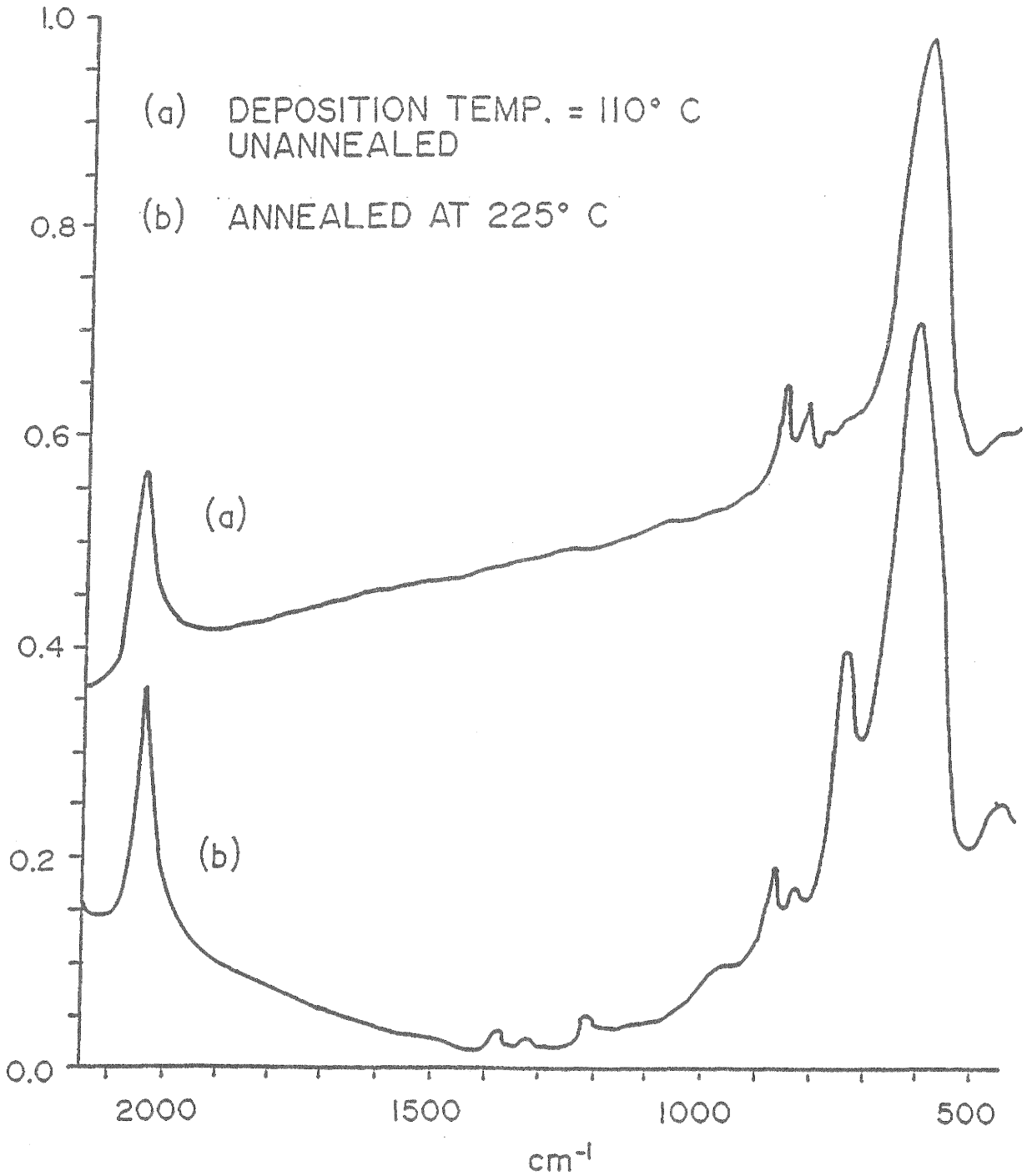

dangling bond states due to some barrier, and that some thermal energy is required to overcome this barrier - somewhat akin to the heat treatment required to "activate" ion-implanted dopant atoms in single crystal silicon. Even if the hydrogen needs to move one or two atoms distances for proper orientation for complexing, such thermally induced motion at ~200° C is quite reasonable and plausible considering its mobility at these temperatures.

2.0 HIGH EFFICIENCY DEVICE RESEARCH

2.1 INTRODUCTION

The high efficiency device research has focussed on developing alloy single junction and stacked junction solar cells. We have explored a-SiC:H single junction cells in the bandgap range of 1.7eV to 2.0eV, a-SiGe:H single junction cells in the bandgap range of 1.7eV to 1.5eV. Tandem cells have been fabricated employing these materials. Triple stacked cells have been fabricated employing 1.4eV bandgap a-SiGe:H back cells.

2.2 AMORPHOUS SILICON-CARBON SINGLE JUNCTION CELLS

During this period even though a large number of feedstocks were explored for intrinsic a-SiC:H alloys single junction solar cells were only fabricated with material deposited from silane and methane.

Single junction solar cells were fabricated in which the i-layer material consisted of a-SiC:H with optical bandgap from 1.8eV to 1.95eV. These cells had a conventional a-SiC:H p-layer and an a-Si:H n-layer. No p/i graded interface layers were employed. The intrinsic layer thickness was restricted to 2000Å since thicker i-layer cells are not needed for components of triple stacked cells. Figure 2-1 shows the J-V characteristics of three cells of different bandgap i-layer material. The photovoltaic parameters of these cells are tabulated in Table 2-1. Two trends are clear, as the optical bandgap of the i-layer increases the open-circuit voltage increases but the fill-factor decreases. This is consistent with a fall in the $\mu\tau$ product with an increase in the optical bandgap as discussed in an earlier section.

2.3 AMORPHOUS SILICON-GERMANIUM SINGLE JUNCTION CELLS

Efficient a-SiGe:H alloy p-i-n solar cells not only require the development of device quality intrinsic material but also require the development of appropriate doped layers and optimization of several interfaces in the device structure. We have attempted to optimize the performance of single junction a-SiGe:H p-i-n solar cells by addressing three items. First, the alloy composition of the n-layer, second, the importance of the effect of the i(a-SiGe:H)/n interface, and third, the modification of hole transport in the intrinsic layer by low-level boron doping. The doped layers establish the built-in field which influences the collection of carriers since their transport is field assisted. The interfaces are important because they can act as recombination centers or barriers to the transport of carriers. In a-SiGe:H alloys there is evidence that carrier transport is limited by transport of holes. We have explored low-level boron doping of the i-layer to shift the Fermi-level and change the charge state of the recombination centers within the gap in order to improve the hole transport. Improvements in hole transport may occur either due to a modification of the electric field profile or an increase in the $\mu\tau$ product of holes.

2.3.1 Alloy Composition of n-Layers

Phosphorous doped a-Si:H and a-SiGe:H films were characterized by optical bandgap (Tauc) measurements, photothermal deflection spectroscopy (PDS), dark conductivity and temperature dependence of dark

FIGURE 2-1 J-V CHARACTERISTICS OF a-SiC i-LAYER p-i-n SOLAR CELLS.

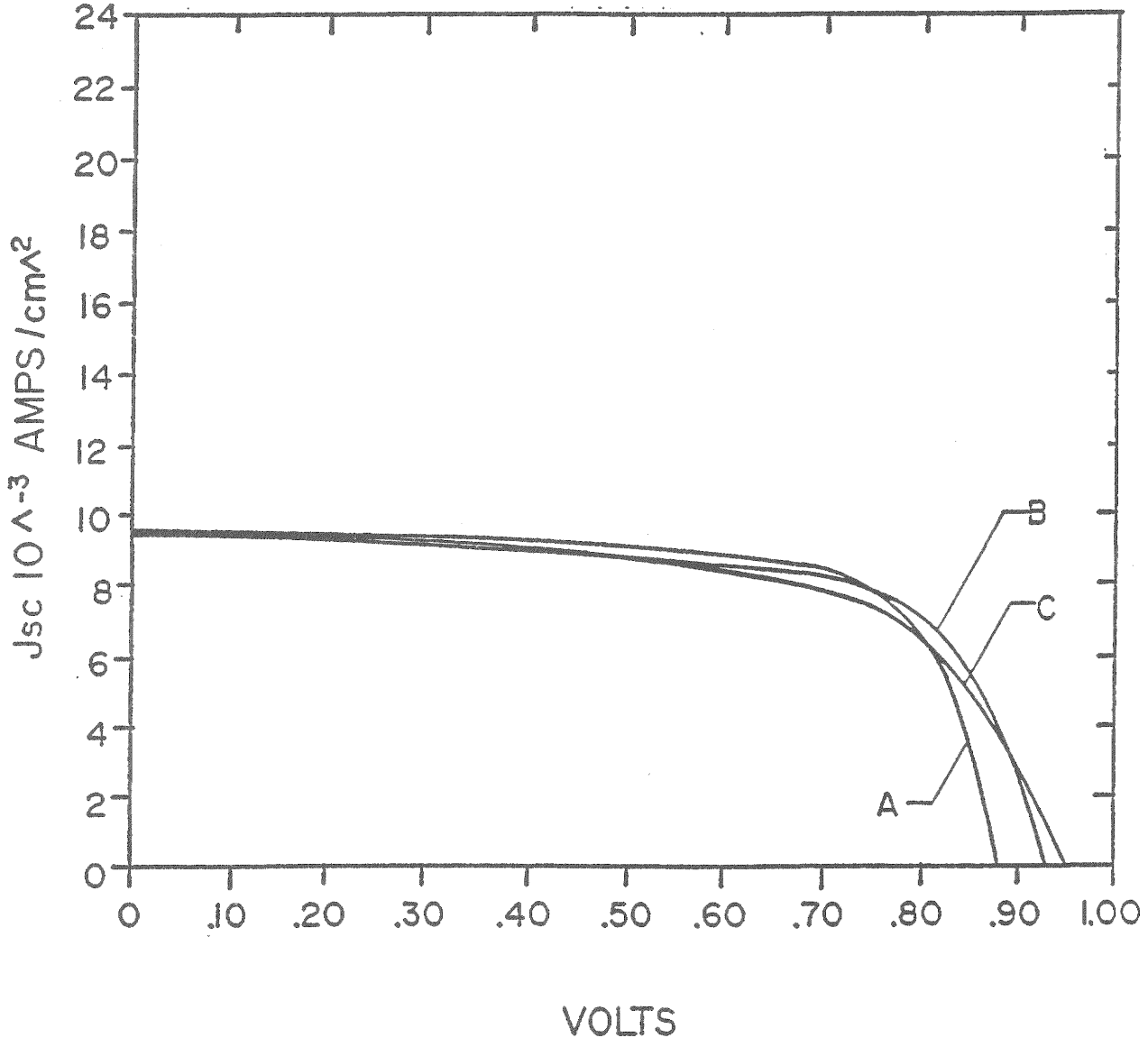

TABLE 2-1

PHOTOVOLTAIC PARAMETERS OF SOME a-SiC:H SINGLE JUNCTION CELLS

Cell #	Eg (eV)	Voc (mV)	Jsc (mA/cm2)	FF	Efficiency (%)
A817342M1	1.8	880	9.59	0.704	5.94
A819444S1	1.85	932	9.44	0.670	5.89
A820314S1	~1.90	952	9.52	0.605	5.48

conductivity. The electrical and optical properties of these n-layers are tabulated in Table 2-2. Figure 2-2 shows the PDS spectra of these two films which indicates that the bandgap of the a-SiGe:H n-layer is about 0.24eV lower than that of the a-Si:H n-layer. This is in good agreement with the optical bandgaps measured by the Tauc method. The PDS spectra indicate no large difference in the mid-gap density of states for these n-layers. The dark conductivity of the a-SiGe:H n-layer was found to be about an order of magnitude lower than that of a-Si:H n-layer. Moreover, the conductivity activation energy (E_a) of the a-SiGe:H n-layer was 0.299eV as compared to 0.207eV for the a-Si:H n-layer. This clearly indicates the inferior effective doping of a-SiGe:H n-layers. It is possible that in a-SiGe:H films the formation of defects with an energy in the mid-gap region compensates the dopant and pulls the Fermi level towards the mid-gap. In a-Ge:H, which has two orders of magnitude higher density of dangling bonds than a-Si:H, it has been reported that it takes a much higher level of dopants to shift the Fermi-level out of the dangling bond band into one of the band tails. A similar effect, to a lesser extent, seems to take place in a-SiGe:H alloys.

Single junction solar cells were fabricated with an identical device structure except that one cell had an a-SiGe:H n-layer while the other had an a-Si:H n-layer. The photovoltaic parameters of these cells are tabulated in Table 2-3. Figure 2-3 shows the J-V characteristics of these two devices under AM1.5 global conditions and Figure 2-4 shows their quantum efficiency versus wavelength measurements. It is clear from Table 2-3 that the short-circuit current density and the fill-factor of the device with the a-Si:H n-layer is far superior to that of the device with the a-SiGe:H n-layer. In these devices, the difference in the J_{sc} values can be explained in terms of the optical losses due to the absorption in the respective n-layers (E_g = 1.71eV for a-Si:H and E_g = 1.54eV for a-SiGe:H). The small difference in V_{oc} and the poor fill-factor are probably due to the inferior doping characteristics of the a-SiGe:H n-layer. A more resistive n-layer can lead to less band-bending at the i/n interface or a resistive n/metal contact and consequently a lower value of fill-factor. In this device structure light enters from the p-side, hence, changes in the conductivity of the n-layer do not affect the open-circuit voltage very much. The hypothesis of less band banding at the i/n interface is supported by the bias dependency of the quantum efficiency measurements which measures carrier collection as the built-in field is changed. If this reduction in field strength with applied bias is uniform, one would expect little wavelength dependence in the collection of carriers. In a-SiGe:H devices there is a strong bias dependence on the collection of long wavelength generated carriers which indicates hole transport limits the performance. In these devices the same trend is seen but cells with a-SiGe:H n-layers have a much larger bias dependence than cells with a-Si:H n-layers. This is shown in Figure 2-5 where the ratio of quantum efficiency versus wavelength measurements at 0.6V to that at 0V is plotted for cells with the two different n-layers. Hence, the performance of a-SiGe:H single junction solar cells can be significantly improved by using a-Si:H n-layers.

2.3.2 Inverse graded layer (IGL) at the i/n interface

We have also studied the effect of depositing an inverse graded layer (IGL) at the i(a-SiGe:H)/n(a-Si:H) interface. This interface is between 50-100Å thick and is deposited by changing the gas ratio of silane and germane such that the bandgap changes from 1.55eV to 1.7eV over this interface. The device structure is shown in Figure 2-6. The effect of employing an IGL can be seen in Table 2-4 where the photovoltaic parameters of two identical a-SiGe:H cells with and without IGL are tabulated. These devices had Ti/Ag rear contacts. Clearly, by employing an IGL the fill-factor improves. We speculate that this occurs for two reasons. First the n-layer now contacts an a-Si:H i-layer which is superior to the a-SiGe:H i-layer and second, the junction is not abrupt but is graded in bandgap. Similar improvements have been reported by Ishihara et al. and Yoshida et al.

2.3.3 Low-level boron doping

In order to improve the hole transport properties of a-SiGe:H alloys we have explored low-level boron doping of intrinsic layers and studied its effect on transport properties of films as well as on the performance of devices. We chose trifluoroboron (BF_3) as a p-type dopant instead of the more traditional diborane (B_2H_6) as

FIGURE 2-2 PDS SPECTRA OF a-Si:H AND a-SiGe:H n-LAYER.

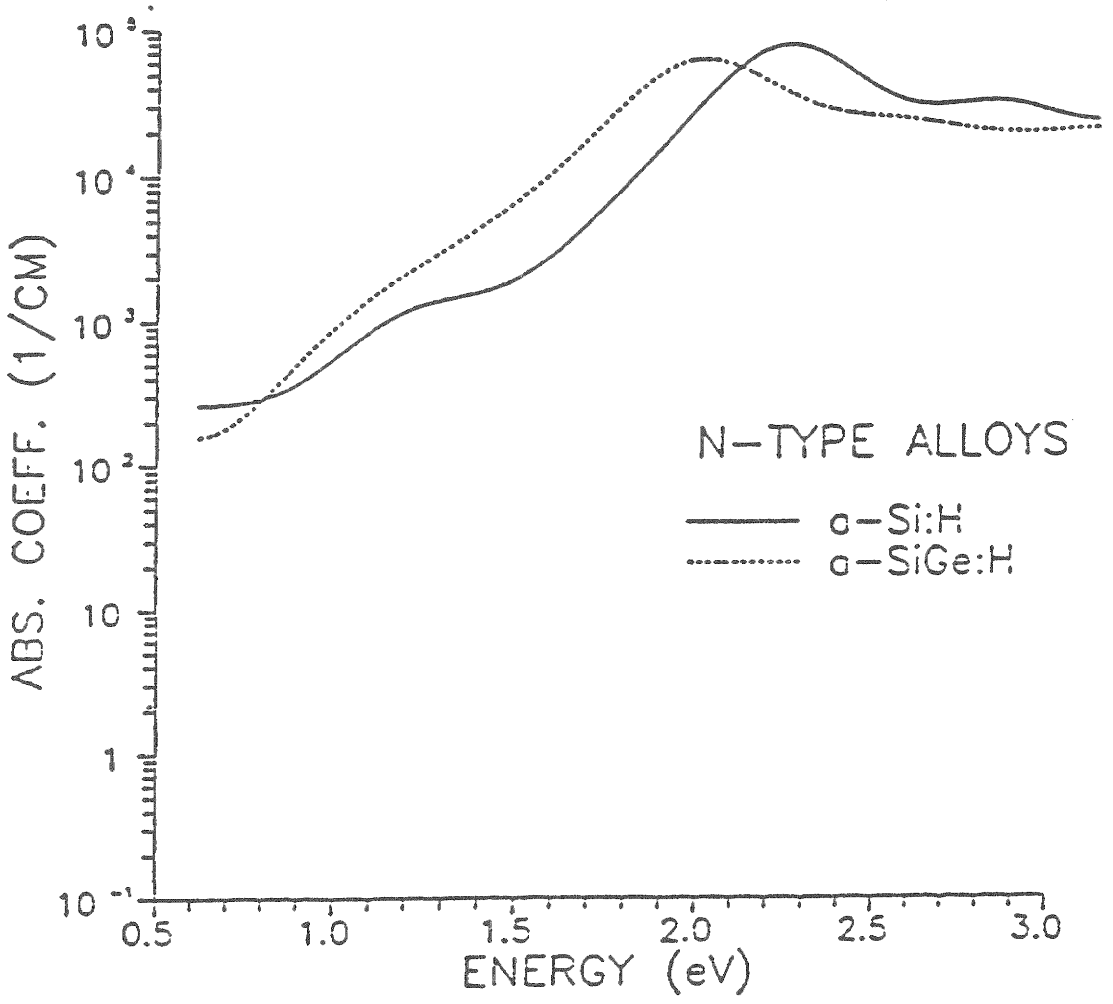

TABLE 2-2

ELECTRICAL AND OPTICAL PROPERTIES OF n-LAYERS

Property	a-Si:H	a-SiGe:H
Optical Bandgap	1.71eV	1.54eV
Dark Conductivity	$6.4 \times 10^{-3} (\Omega\text{-cm})^{-1}$	$3.1 \times 10^{-4} (\Omega\text{-cm})^{-1}$
Activation Energy	0.207eV	0.299eV

TABLE 2-3

PHOTOVOLTAIC PARAMETERS OF CELLS WITH DIFFERENT n-LAYERS

Cell #	Voc (mV)	Jsc (mA/cm2)	FF	Efficiency (%)	n-Layer
LL724422	834	19.23	0.629	10.08	a-Si:H
LL724431	822	18.03	0.519	6.69	a-SiGe:H

FIGURE 2-3 J-V CHARACTERISTICS UNDER SIMULATED AM1.5 CONDITIONS OF IDENTICAL a-SiGe:H SOLAR CELLS WITH (a) a-Si:H LAYER AND (b) a-SiGe n-LAYER.

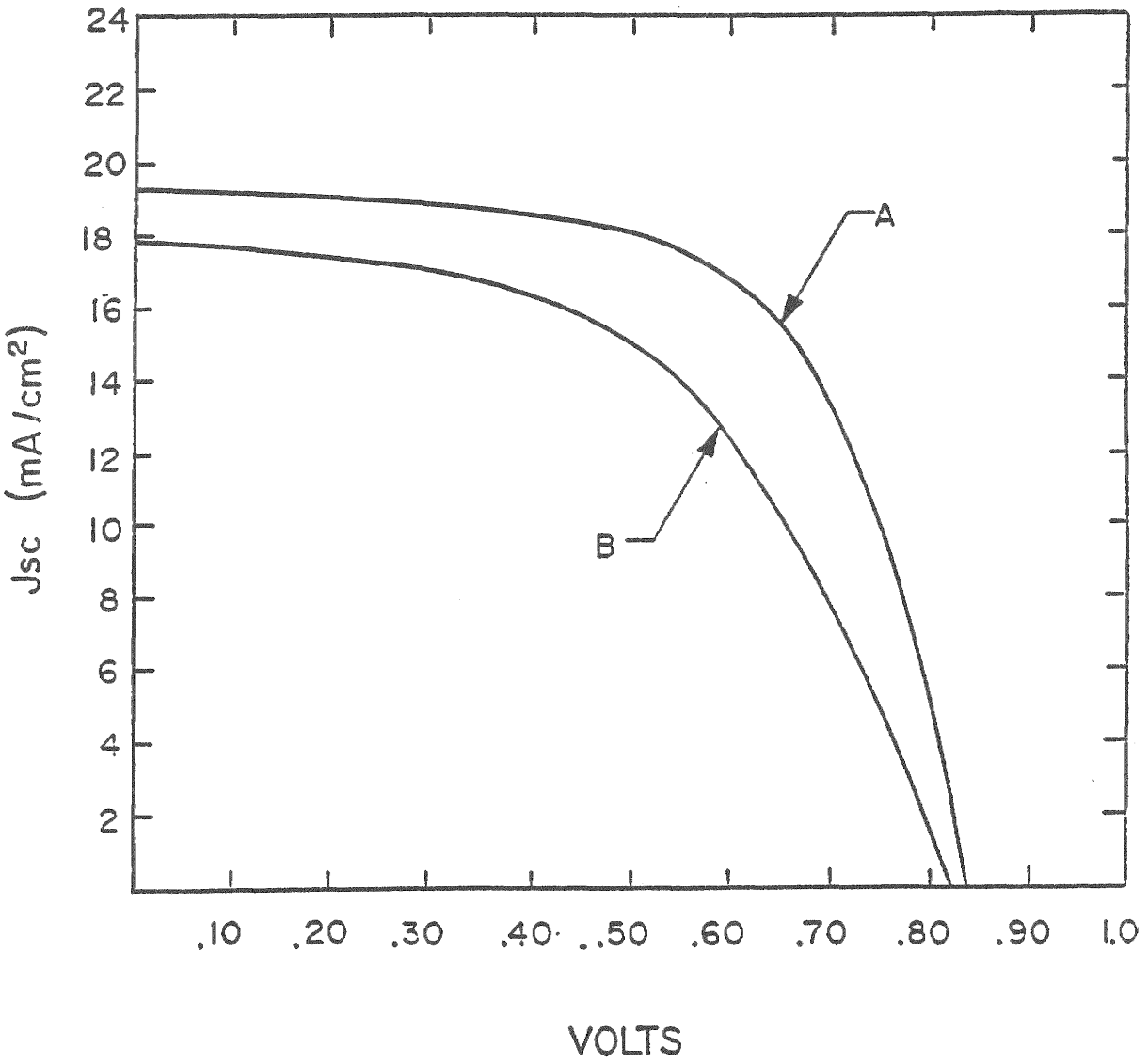

FIGURE 2-4 QUANTUM EFFICIENCY VERSUS WAVELENGTH MEASUREMENTS OF THE DEVICES SHOWN IN FIG. 2.2.2-2.

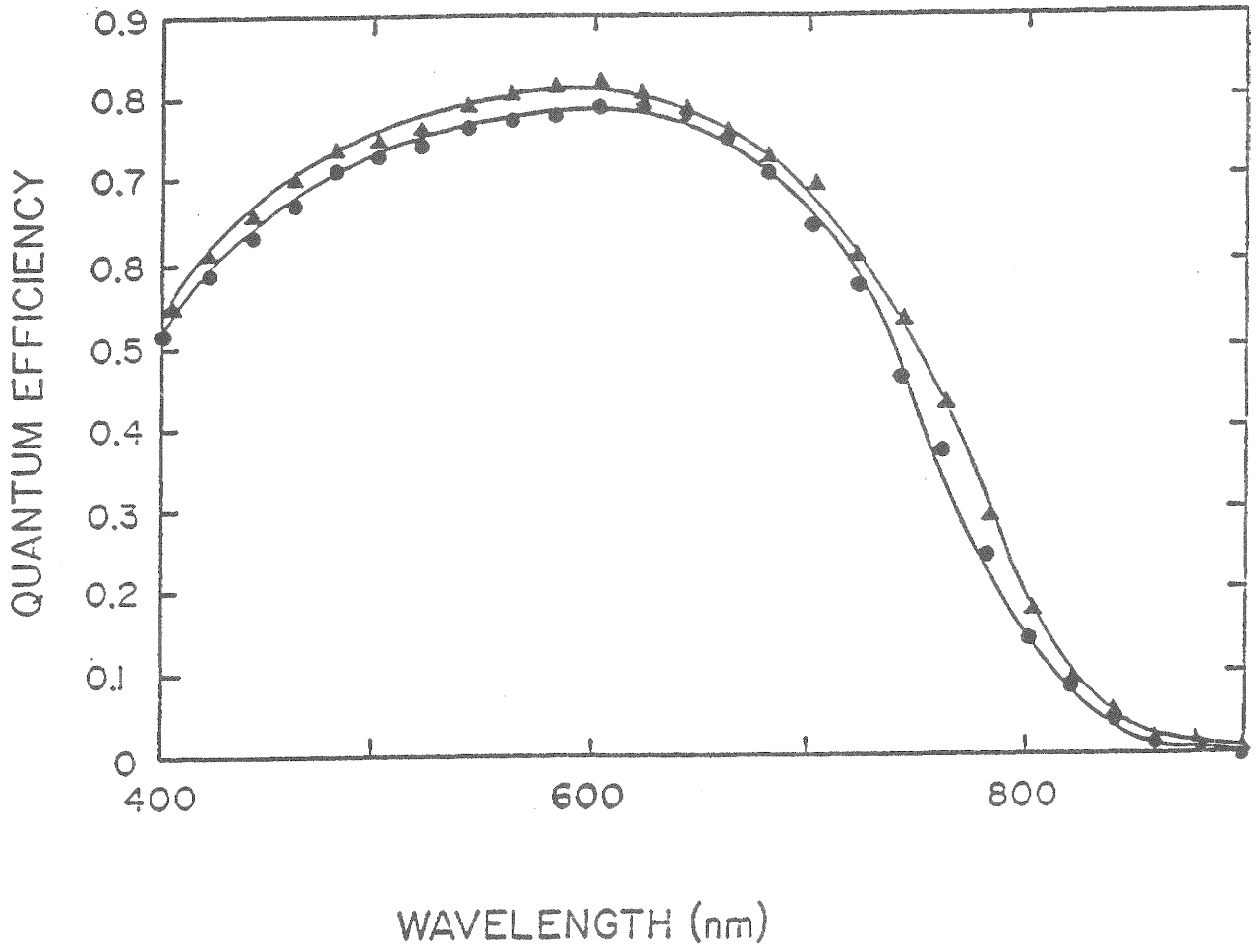

FIGURE 2-5 RATIO OF QUANTUM EFFICIENCY (0.6V/0V) AS A FUNCTION OF WAVELENGTH OF DEVICES SHOWN IN Fig. 2-3.

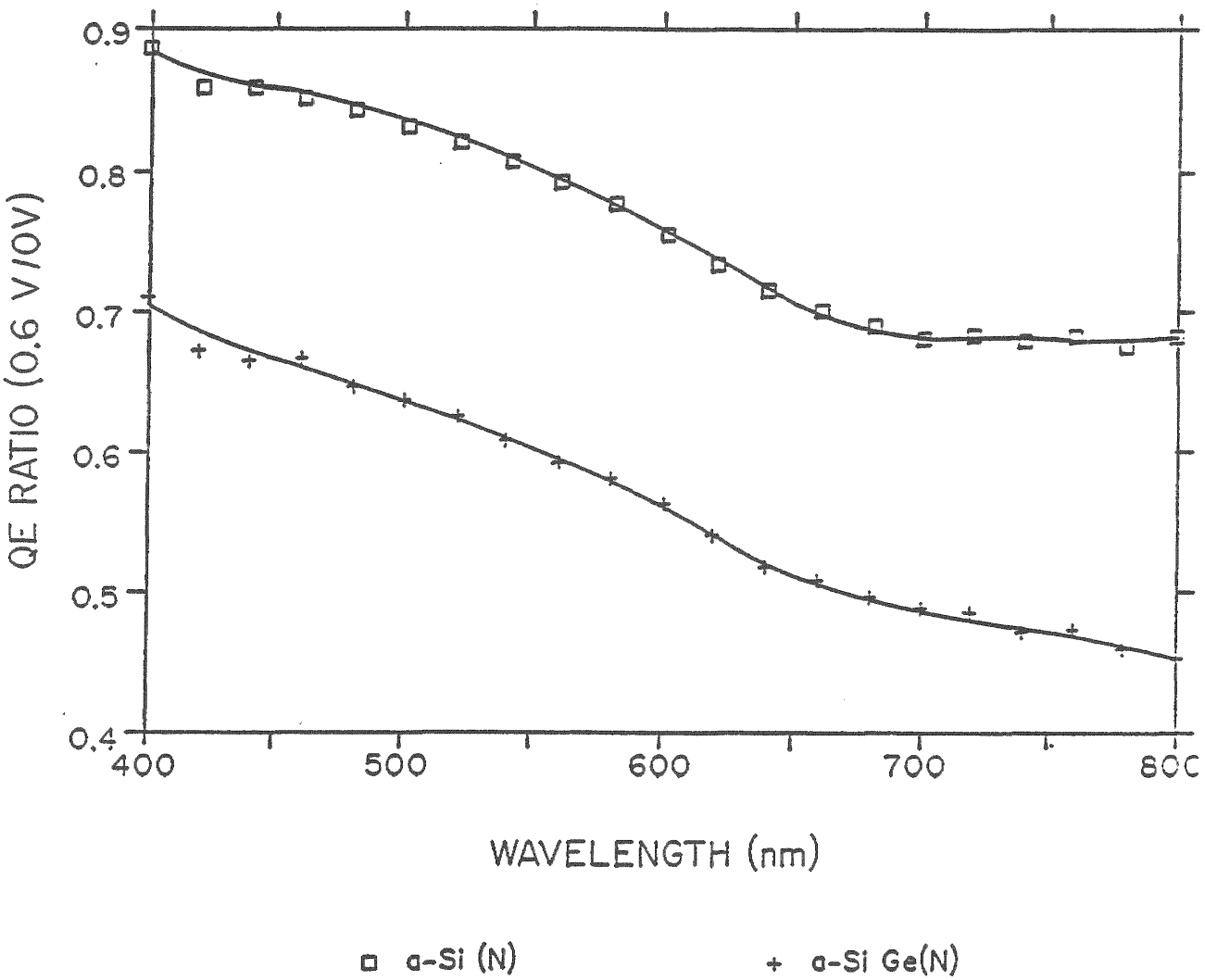

FIGURE 2-6 DEVICE STRUCTURE OF a-SiGe:H SINGLE JUNCTION SOLAR CELLS.

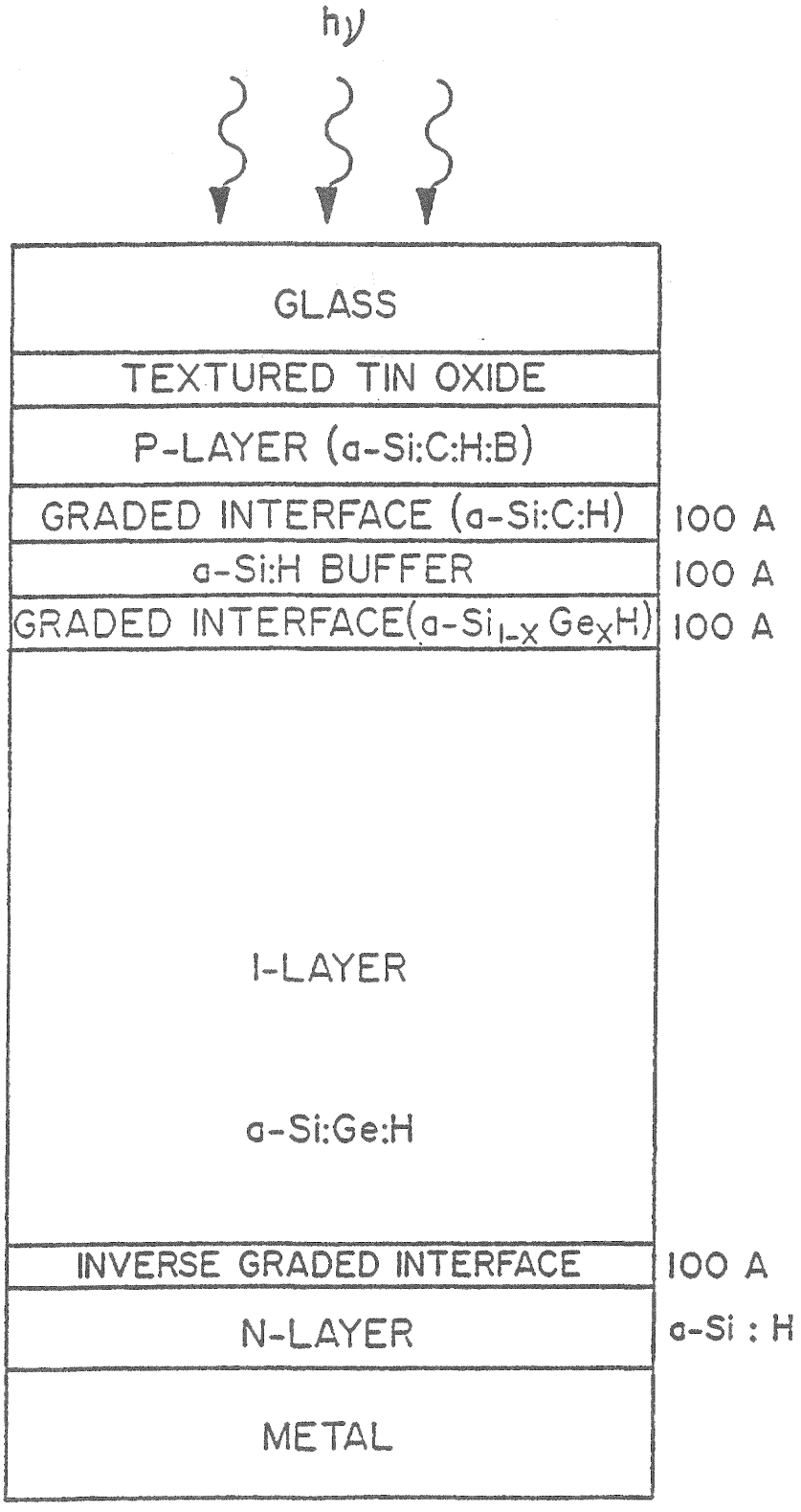

TABLE 2-4

PHOTOVOLTAIC PARAMETERS OF CELLS WITH AND WITHOUT IGL

Cell #	Voc (mV)	Jsc mA/cm2)	FF	Efficiency (%)	Remarks
LL724423	852	17.7	0.548	8.26	No IGL
LL724443	842	17.7	0.584	8.70	With IGL

a boron source because it is a monomeric form of boron and reduces the changes of forming undesirable boron-boron bonds in the a-SiGe:H film during plasma decomposition. The small amount of fluoride introduced with the boron would be expected to have minimal affect on the film. Moreover, boron trifluoride is readily available with high purity and is quite stable chemically in the absence of water. The greater stability of BF_3 relative to B_2H_6 makes it possible to prepare and more reliably handle dilute mixtures (less than 100ppm) of BF_3 in silane and other diluents.

Boron doping was carried out on 1.55eV bandgap a-SiGe:H material in the range of 0-10ppm of BF_3 in the gas phase. This was accomplished by deposition from a gas mixture of silane, germane, and 40ppm BF_3 mixed with silane. Figures 2-7(a) and (b) show the effect of boron doping on the dark conductivity and conductivity activation energy. As the doping is increased from 0 to 10ppm the dark conductivity decreases from $2x10^{-10}(\Omega\text{-cm})^{-1}$ to $8x10^{-12}(\Omega\text{-cm})^{-1}$ and the activation energy increases from 0.76eV to 0.89eV. The dark conductivity data indicates that the undoped material is slightly n-type and that doping moves the Fermi level towards the valence band. Figures 2-8(a) and (b) show the effect of boron doping on the photoconductivity and the ratio of dark to photoconductivity. The photoconductivity decreases from $2x10^{-6}(\Omega\text{-cm})^{-1}$ to $4x10^{-7}(\Omega\text{-cm})^{-1}$ but the ratio of photo to dark conductivity increases from $8x10^{3}$ to $5x10^{4}$.

Single junction a-SiGe:H devices were fabricated with uniform boron doping of the i-layer. Figure 2-9 shows the quantum efficiency versus wavelength measurements of two otherwise identical devices, one with no boron doping and the other in which the i-layer was deposited with 6ppm BF_3 in the i-layer. Clearly, boron doping lowers the blue response but increases the red response of the device. Figures 2-10(a) and (b) show the J-V characteristics of the same two devices under long wavelength illumination (beyond 600nm) to simulate its use in tandem cells. The cell with boron doping not only has a higher short-circuits current density but also has a superior fill-factor. Hence, low-level boron doping of intrinsic a-SiGe:H should be useful in stacked junction devices where the back cell sees only long wavelength illumination.

Employing the device structure shown in Figure 2-6 with an a-SiGe:H i-layer of bandgap 1.55eV with an inverse graded interface and an a-Si:H n-layer, the highest conversion efficiency achieved was 10.1%. This device had a short-circuit current density of $20.1mA/cm^2$. Figure 2-11 shows the J-V characteristic of this device under global AM1.5 conditions and Figure 2-12 shows the corresponding quantum efficiency versus wavelength measurement.

The best single junction cell fabricated in which the i-layer had an optical bandgap of 1.5eV had a conversion efficiency of 7.93%. Figure 2-13 show the J-V characteristics of this device and Figure 2-14 shows the quantum efficiency versus wavelength measurement on this device which shows a response greater than 30% at 800nm. This device generates more than $21mA/cm^2$ current as shown in Figure 2-15 where the quantum efficiency measurement was made under an applied reverse bias. Figure 2-16 shows the J-V characteristics of a 1000Å thick a-SiGe:H single junction cell with an optical bandgap of 1.4eV. Figure 2-17 shows the corresponding quantum efficiency versus wavelength measurement which indicates a response of 45.4% at 800nm and 12% at 900nm respectively.

2.4 MULTI-JUNCTION (STACKED) CELLS

Multi-junction (tandem) solar cells in which the top cell has an i-layer of a-SiC:H and the bottom cell has an i-layer of either a-Si:H or a-SiGe:H have resulted in conversion efficiencies above 10%.

Figure 2-18 shows the J-V characteristics of an a-SiC:H/a-Si:H stacked junction cell which had a conversion efficiency of 10.2% with the following photovoltaic parameters: V_{oc} = 1.752V, J_{sc} = $8.16mA/cm^2$, and fill-factor = 0.712. Figure 2-19 shows the quantum efficiency versus wavelength measurement of this device. Figure 2-20 shows the J-V characteristics of an alloy stacked junction cell in which the top cell has an i-layer of a-SiC:H and the bottom cell has an i-layer of a-SiGe:H. This cell had a conversion efficiency of 10.5% with

FIGURE 2-7 (A) DARK CONDUCTIVITY AS A FUNCTION OF LOW LEVEL BORON DOPING a-SiGe:H i-LAYERS. (B) ACTIVATION ENERGY AS A FUNCTION OF LOW LEVEL BORON DOPING OF a-SiGe:H i-LAYERS.

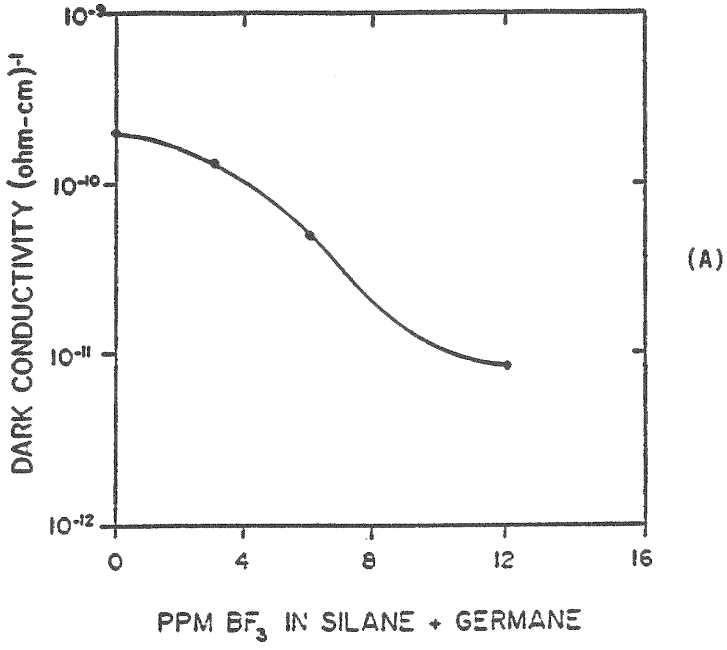

(A)

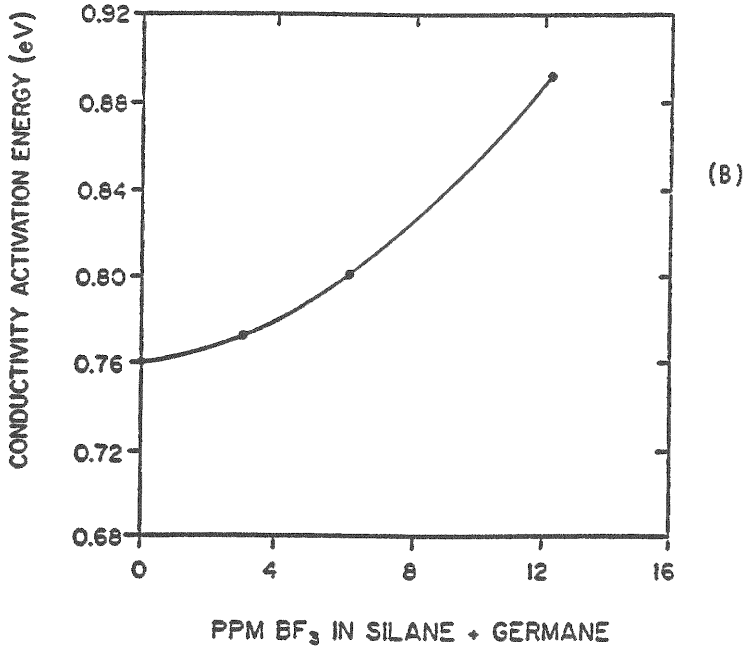

(B)

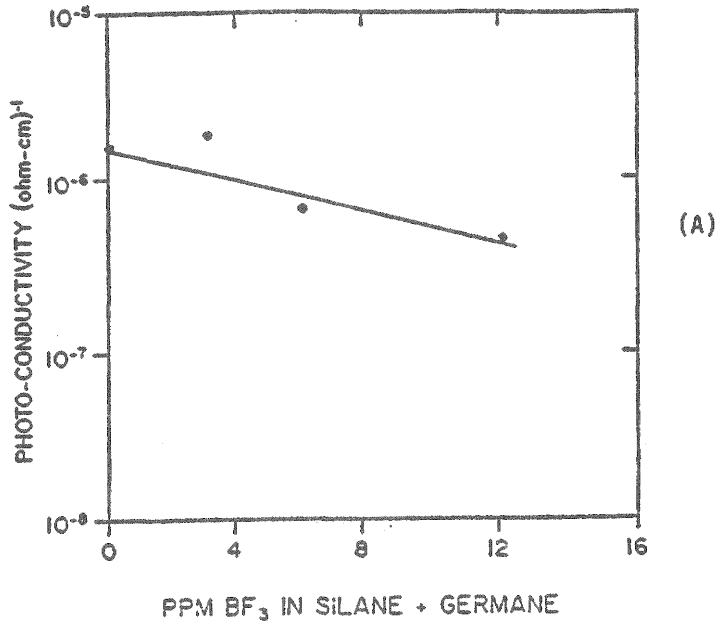

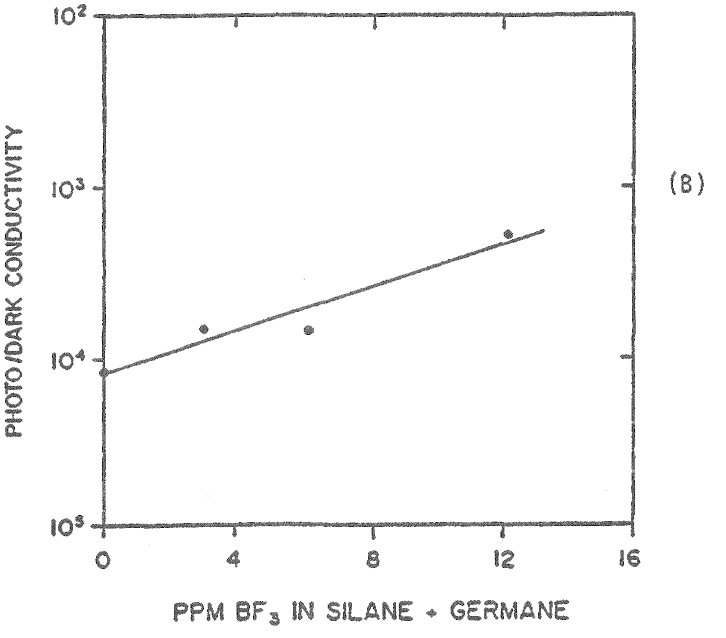

FIGURE 2-8 (A) PHOTOCONDUCTIVITY AS A FUNCTION OF LOW-LEVEL BORON DOPING OF a-SiGe:H i-LAYERS. (B) RATIO OF PHOTO/DARK CONDUCTIVITY OF a-SiGe:H i-LAYERS AS A FUNCTION OF LOW-LEVEL BORON DOPING.

FIGURE 2-9 · QUANTUM EFFICIENCY VERSUS WAVELENGTH MEASUREMENTS OF IDENTICAL DEVICES WITH AND WITHOUT BORON DOPING.

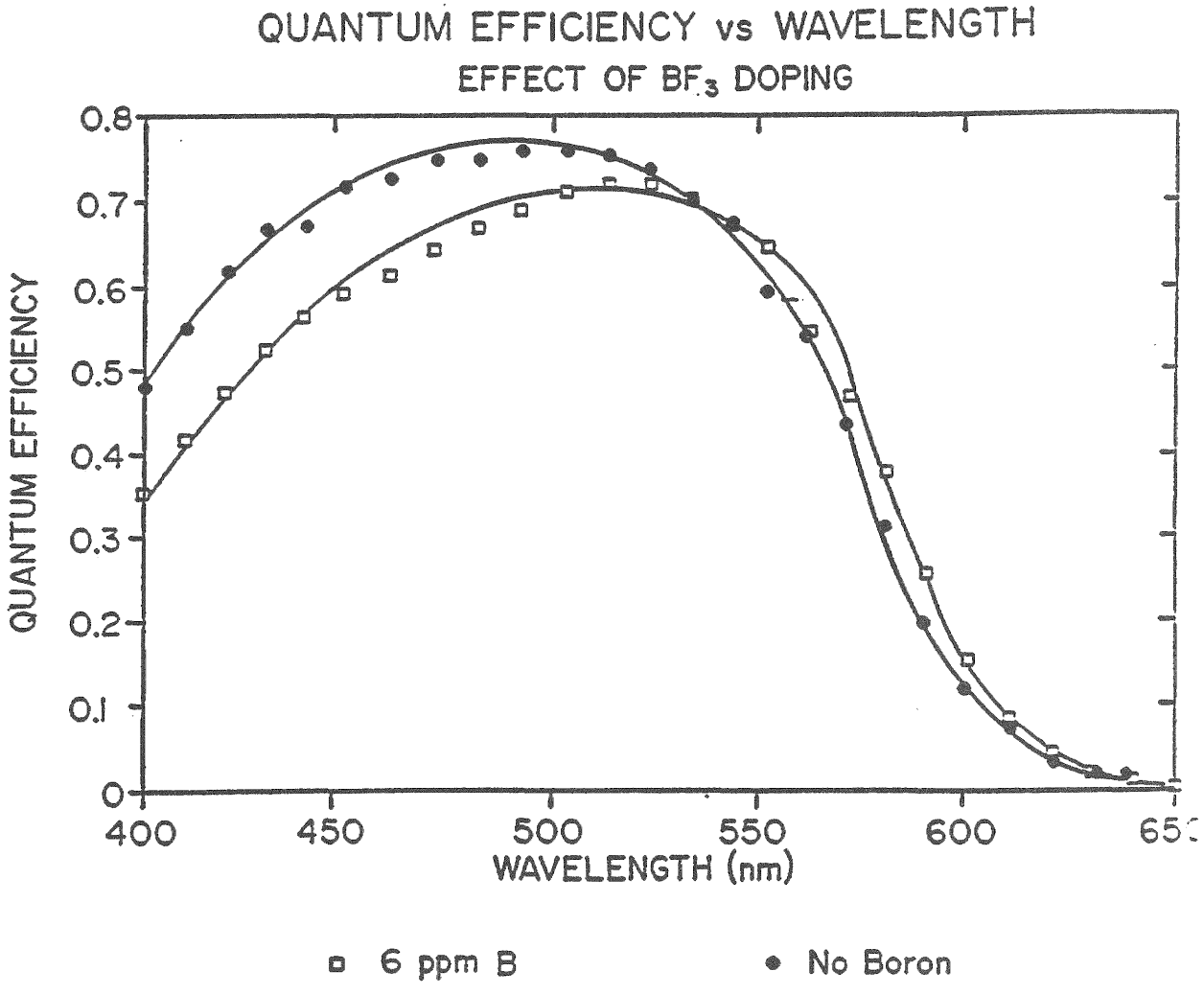

FIGURE 2-10 J-V CHARACTERISTICS UNDER LONG WAVELENGTH ILLUMINATION OF IDENTICAL a-SiGe:H SOLAR CELLS WITH AND WITHOUT BORON DOPING OF THE i-LAYER.

Cell No. =	BF_3 = 0 Orange	Date =	5/5/88
Voc =	-.761 Volts	Jsc =	8.65 ma/cm^2
F.F. =	.579	Eff =	3.82 %
Power =	3.82 mw/cm^2	Illum. =	102.61 mw/cm^2
V (max) =	-.551 Volts	J (max) =	5.92 ma/cm^2
Rs =	1.46E + 01 ohm-cm^2	Rsh =	1.15E + 03 ohm-cm^2

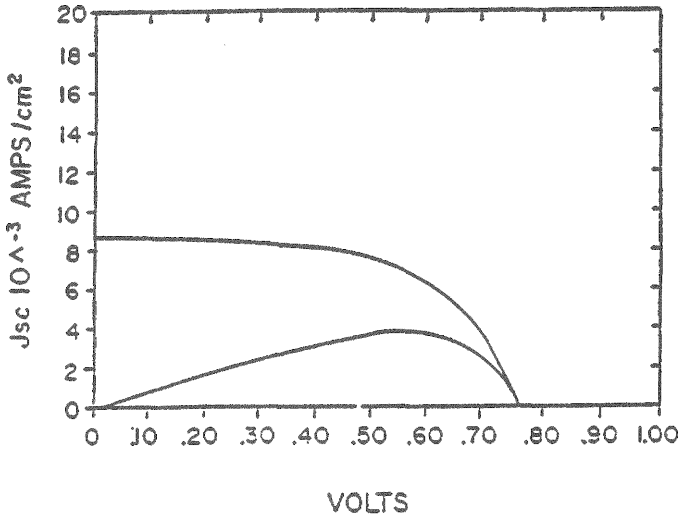

Cell No. =	BF_3 = 30 Orange	Date =	5/5/88
Voc =	-.741 Volts	Jsc =	9.06 ma/cm^2
F.F. =	.620	Eff =	4.16 %
Power =	4.16 mw/cm^2	Illum. =	102.58 mw/cm^2
V (max) =	-.563 Volts	J (max) =	7.40 ma/cm^2
Rs =	1.10E + 01 ohm-cm^2	Rsh =	5.93E + 02 ohm-cm^2

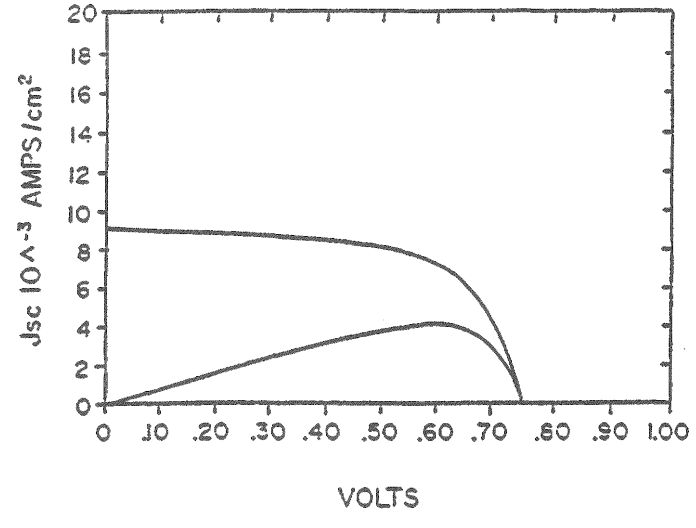

FIGURE 2-11 J-V CHARACTERISTICS UNDER AM1.5 GLOBAL ILLUMINATION OF AN a-SiGe:H SINGLE JUNCTION SOLAR CELL.

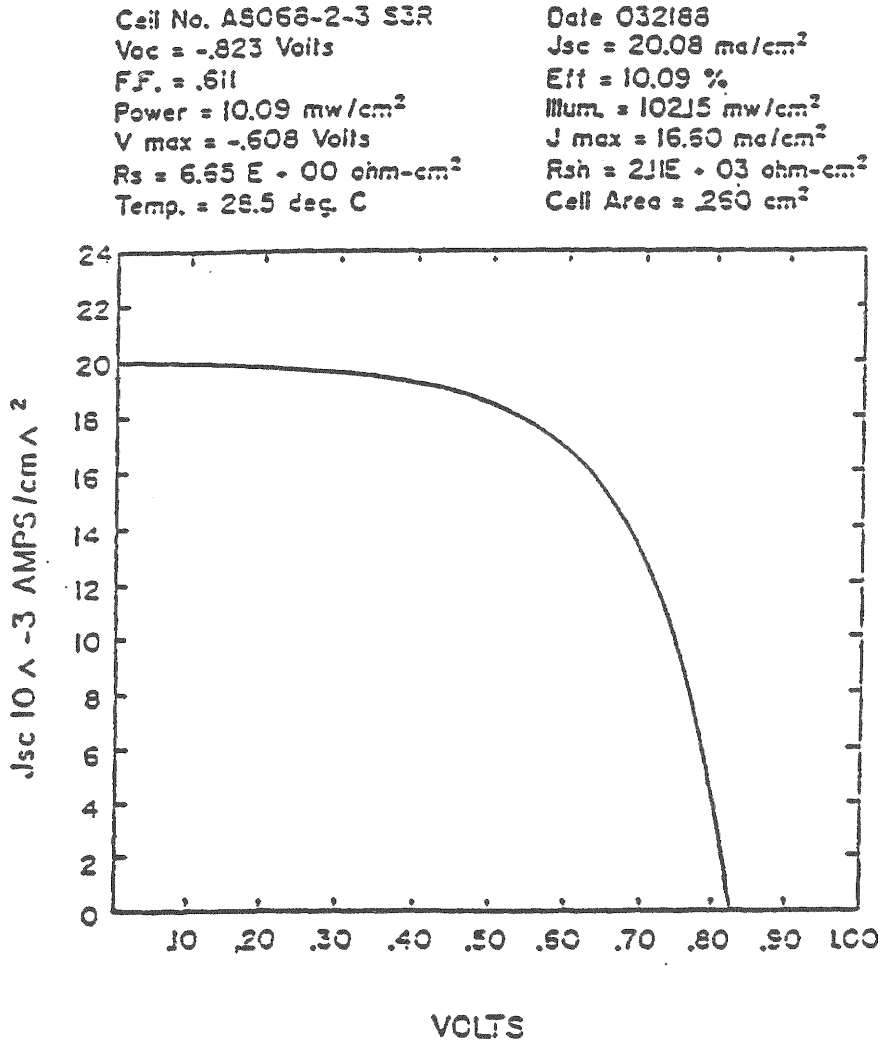

FIGURE 2-12 QUANTUM EFFICIENCY VERSUS WAVELENGTH MEASUREMENTS OF THE DEVICE SHOWN IN FIGURE 2-11.

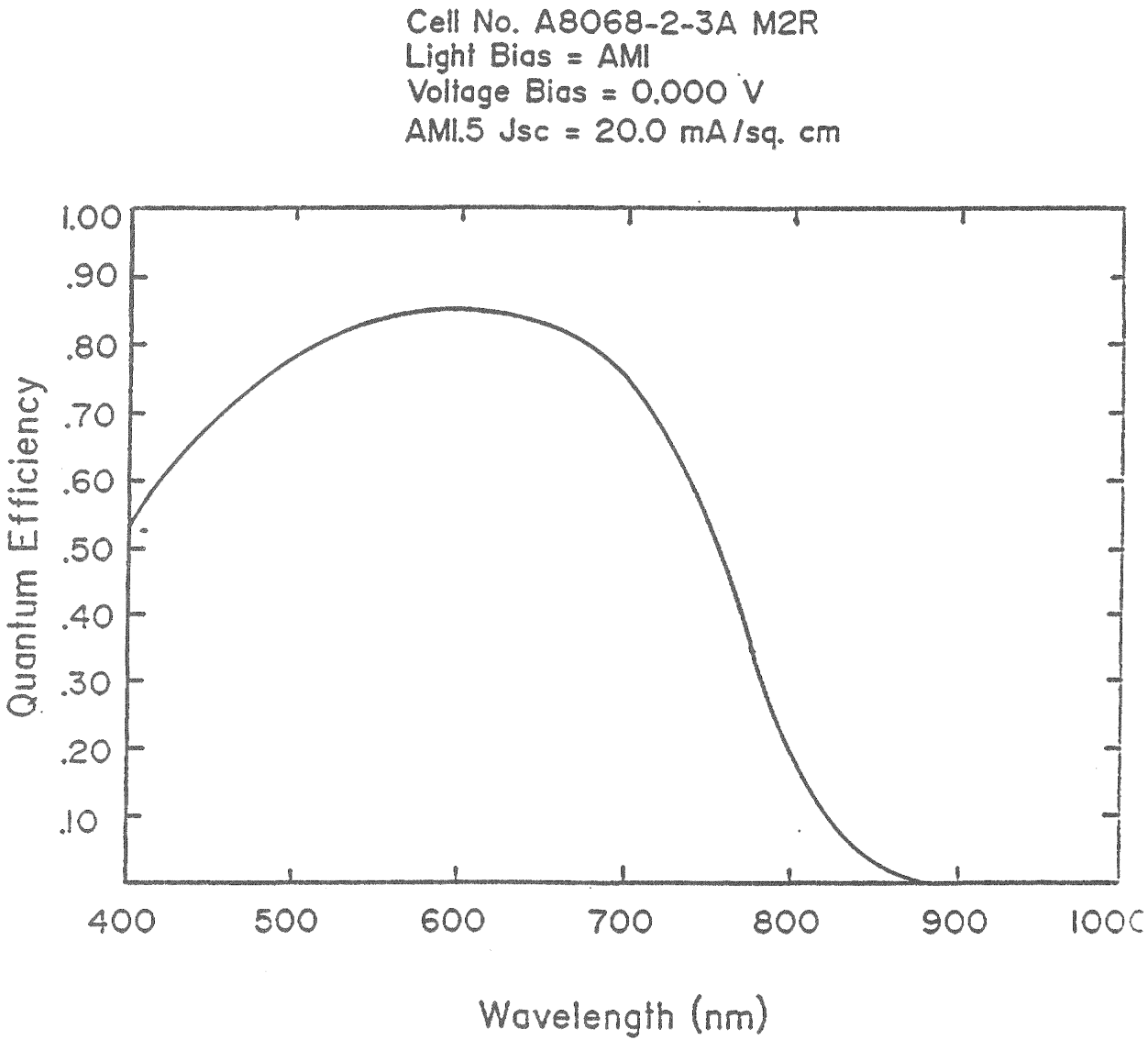

FIGURE 2-13 J-V CHARACTERISTICS OF AN a-SiGe SOLAR CELL WITH BANDGAP 1.5eV.

Cell No. = A8069-2-4 M2

Cell Area	= .620 cm^2	Date	= 3/21/88
Voc (I)	= -.756 Volts	No. of Segments	= 1
Voc	= -.752 Volts	Jsc	= 19.29 ma/cm^2
F.F.	= .547	Eff	= 7.93 %
Power	= 7.93 mw/cm^2	Illum.	= 102.11 mw/cm^2
V (max)	= -.523 Volts	J (max)	= 15.17 ma/cm^2
Rs	= 8.62E + 00 $ohm-cm^2$	Rsh	= 4.46E + 02 $ohm-cm^2$
Rscc	= 1.00	Rshcc	= 0.00
Temp	= 26.6° C	ITO	= 0.00E + 00 ohm/cm^2

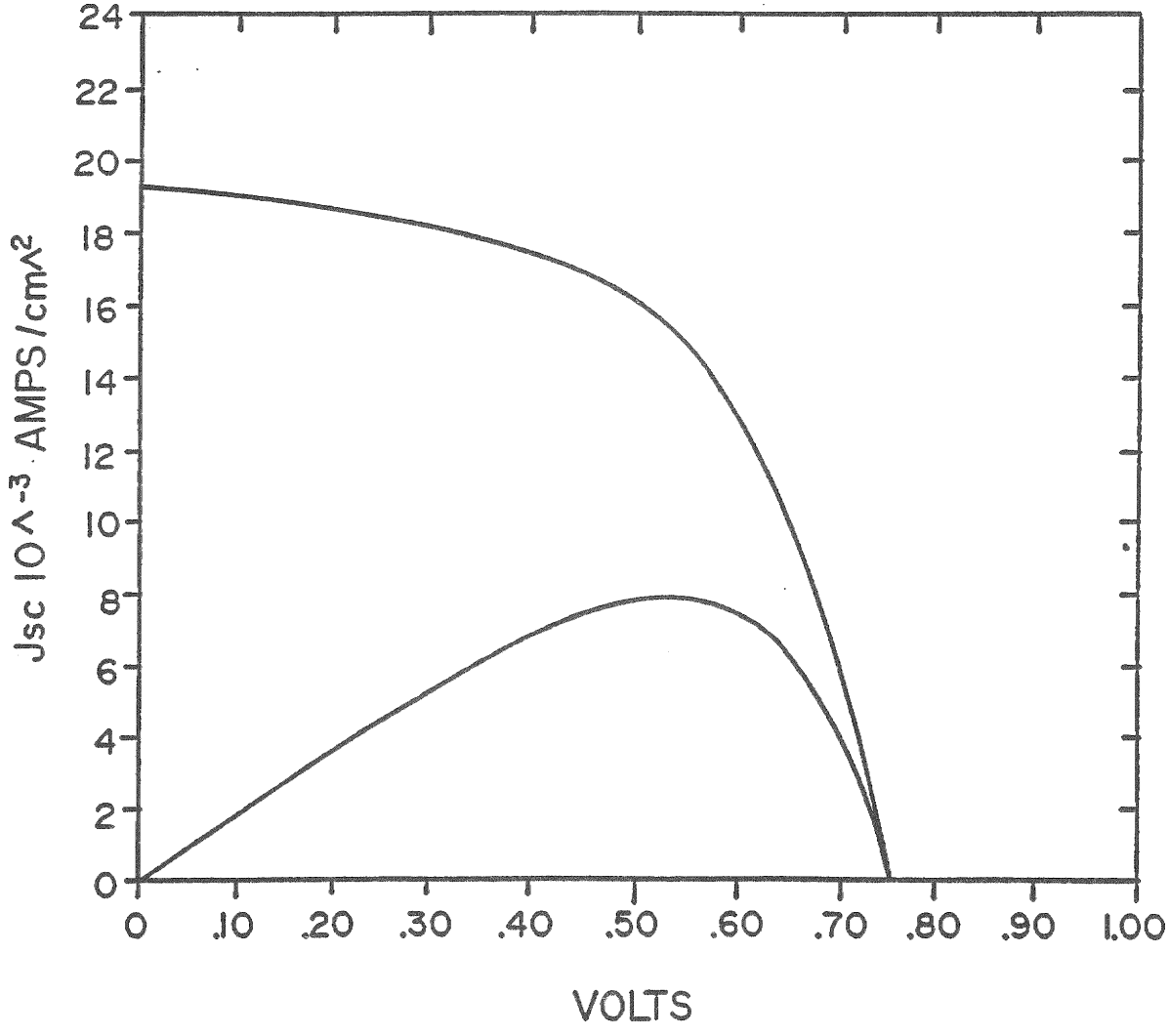

FIGURE 2-14 QUANTUM EFFICIENCY VERSUS WAVELENGTH MEASUREMENT OF CELL IN FIG. 2-13 MEASURED UNDER REVERSE BIAS.

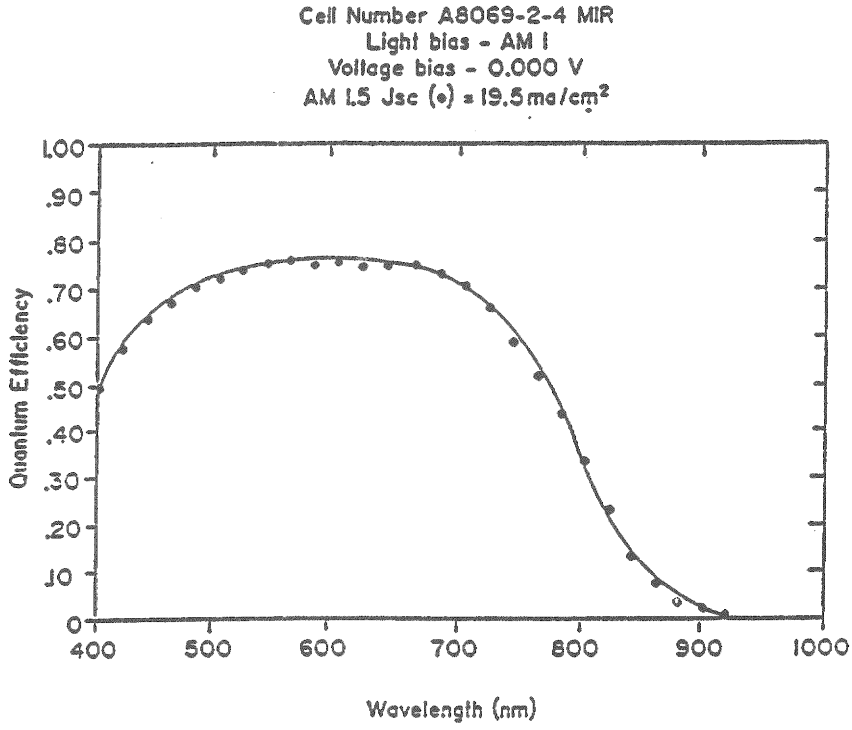

FIGURE 2-15 QUANTUM EFFICIENCY VERSUS WAVELENGTH MEASUREMENT OF CELL IN FIG. 2-13 MEASURED UNDER REVERSE BIAS.

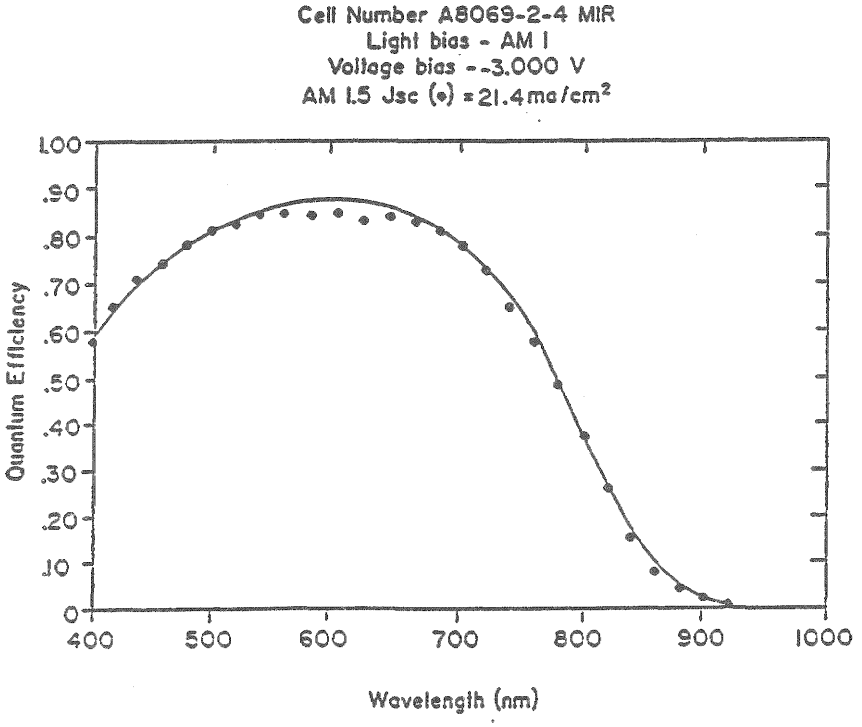

FIGURE 2-16 J-V CHARACTERISTIC OF A 1000Å THICK a-SiGe SOLAR CELL WITH BANDGAP 1.4eV.;

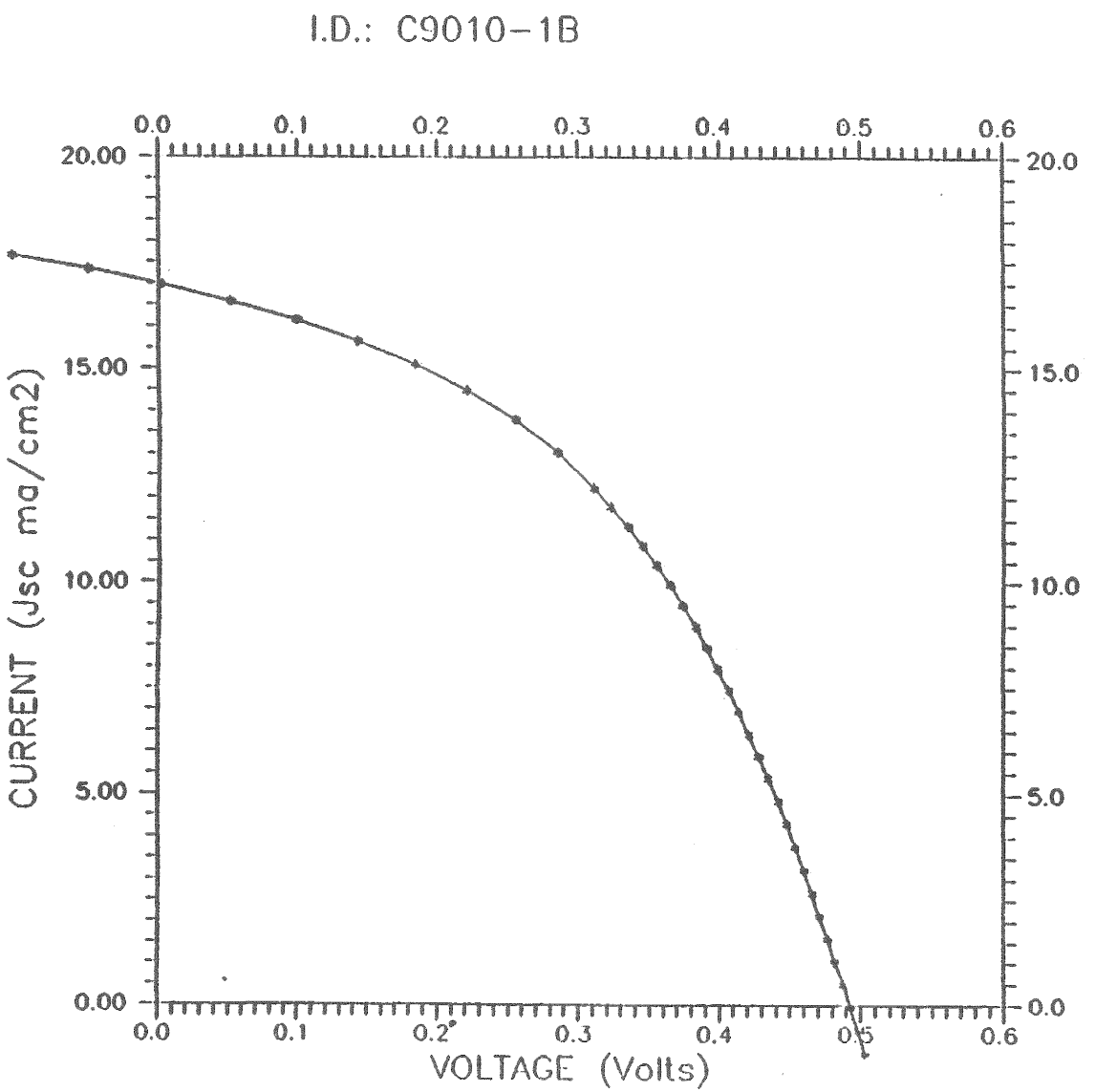

Voc : -0.495 Volts
Jsc : 16.9 ma/cm2
F. F. : 45.5 %
Eff : 3.8 %

Isc : 4.489 ma
Pmax : 3.815 mw/cm2
Imax : 3.125 ma
Vmax : -0.323
Jmax : 11.793 ma/cm2
Rs : 9.32E+00ohm/cm2
Rsh : 1.37E+02ohm/cm2

Intensity:103.1 mw/cm2
Temp : 24.6 C
Cell Area: 0.265 cm2
Segment: 1
Total Area: 0.265 cm2

DATE :01-27-1989
TIME :09:21:17

FIGURE 2-17 QUANTUM EFFICIENCY VERSUS WAVELENGTH OF CELL IN FIG. 2-16

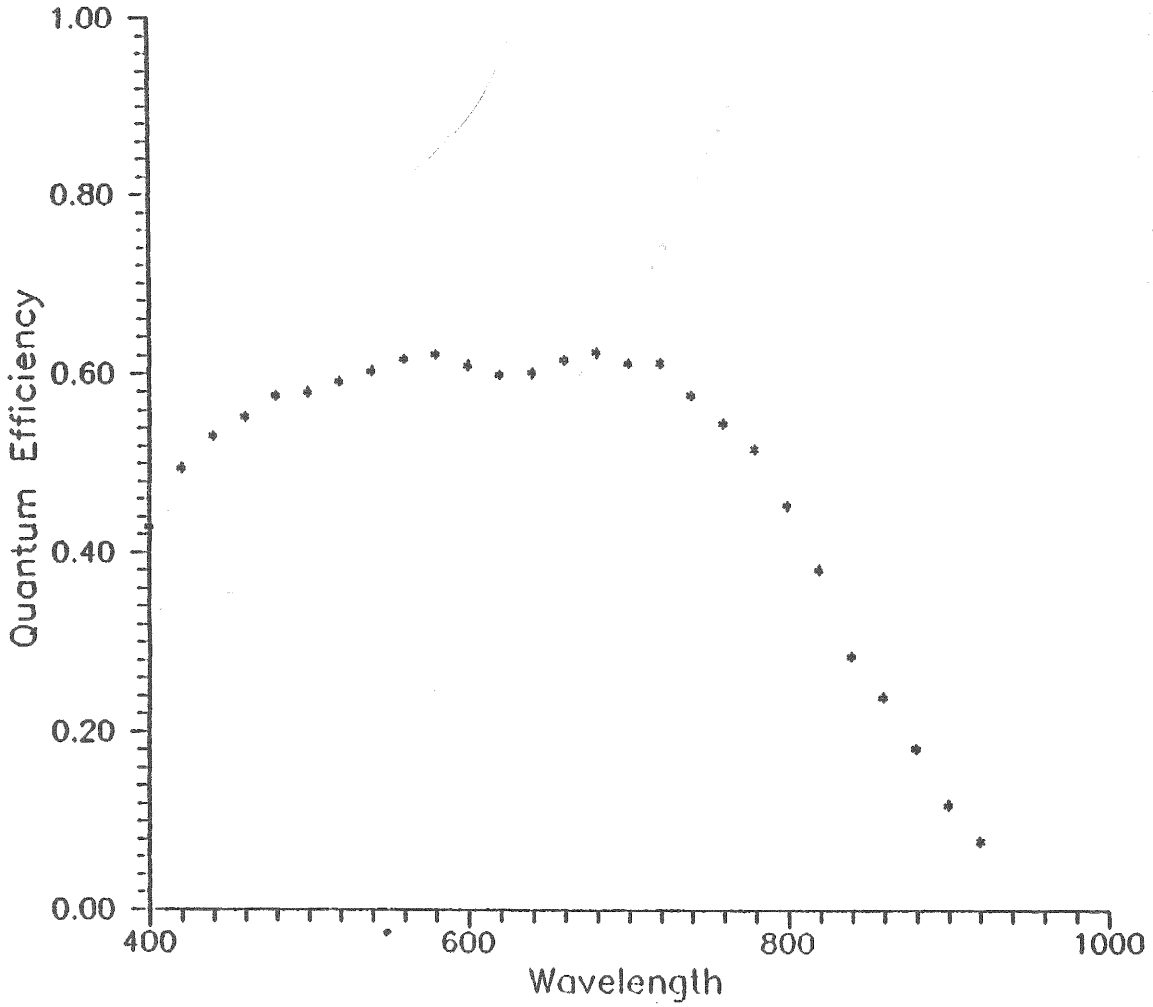

01-19-1989
C9010-1B
S2

400	.429
420	.496
440	.532
460	.554
480	.577
500	.581
520	.593
540	.604
560	.617
580	.622
600	.610
620	.600
640	.602
660	.616
680	.624
700	.612
720	.613
740	.578
760	.547
780	.518
800	.454
820	.382
840	.286
860	.240
880	.183
900	.120
920	.079
Vbias	0.000
Lbias	AM1
Jsc	18.13

FIGURE 2-18 J-V CHARACTERISTICS OF a-SiC:H/a-Si:H STACKED CELL WITH AN EFFICIENCY OF 10.2%.

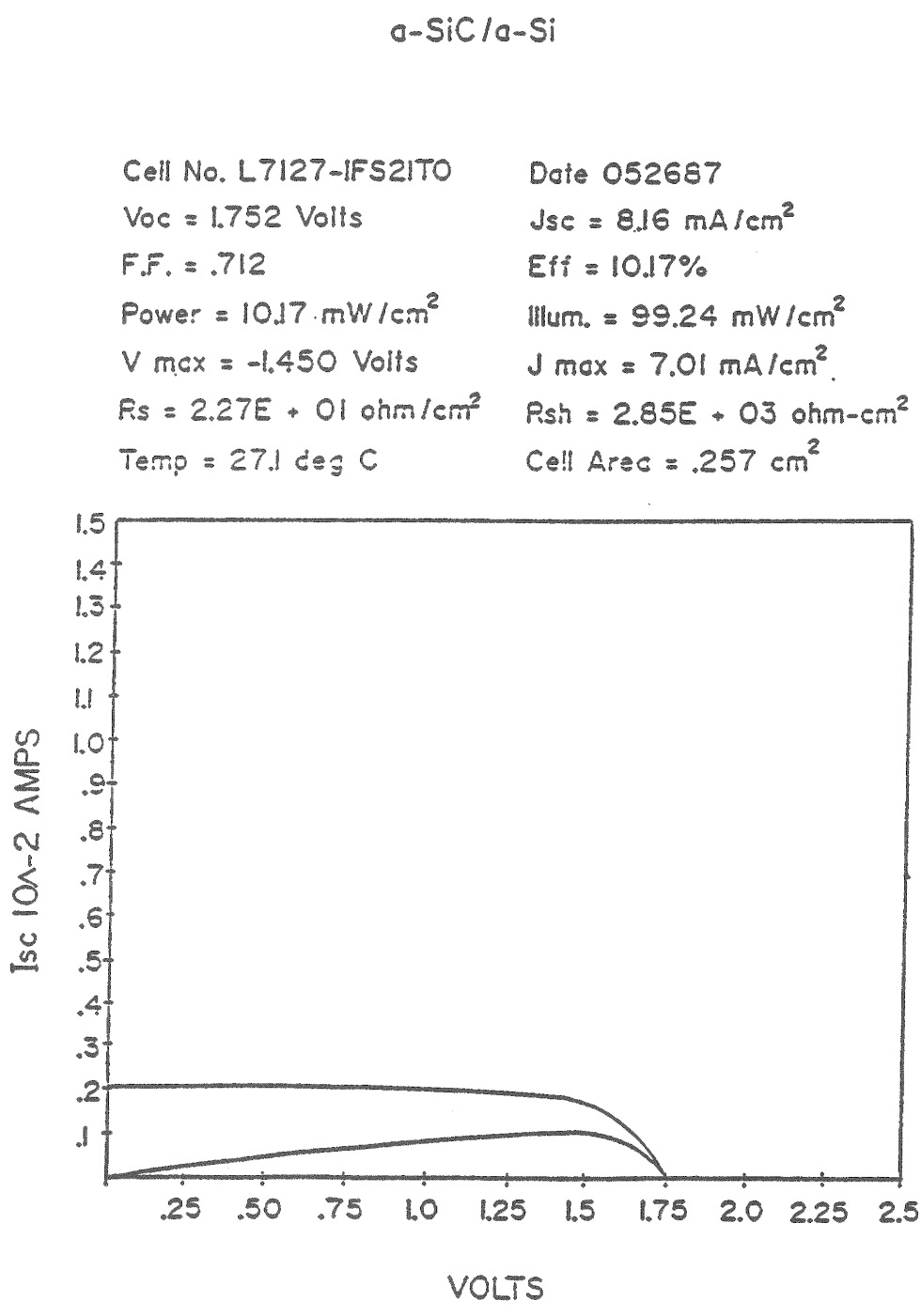

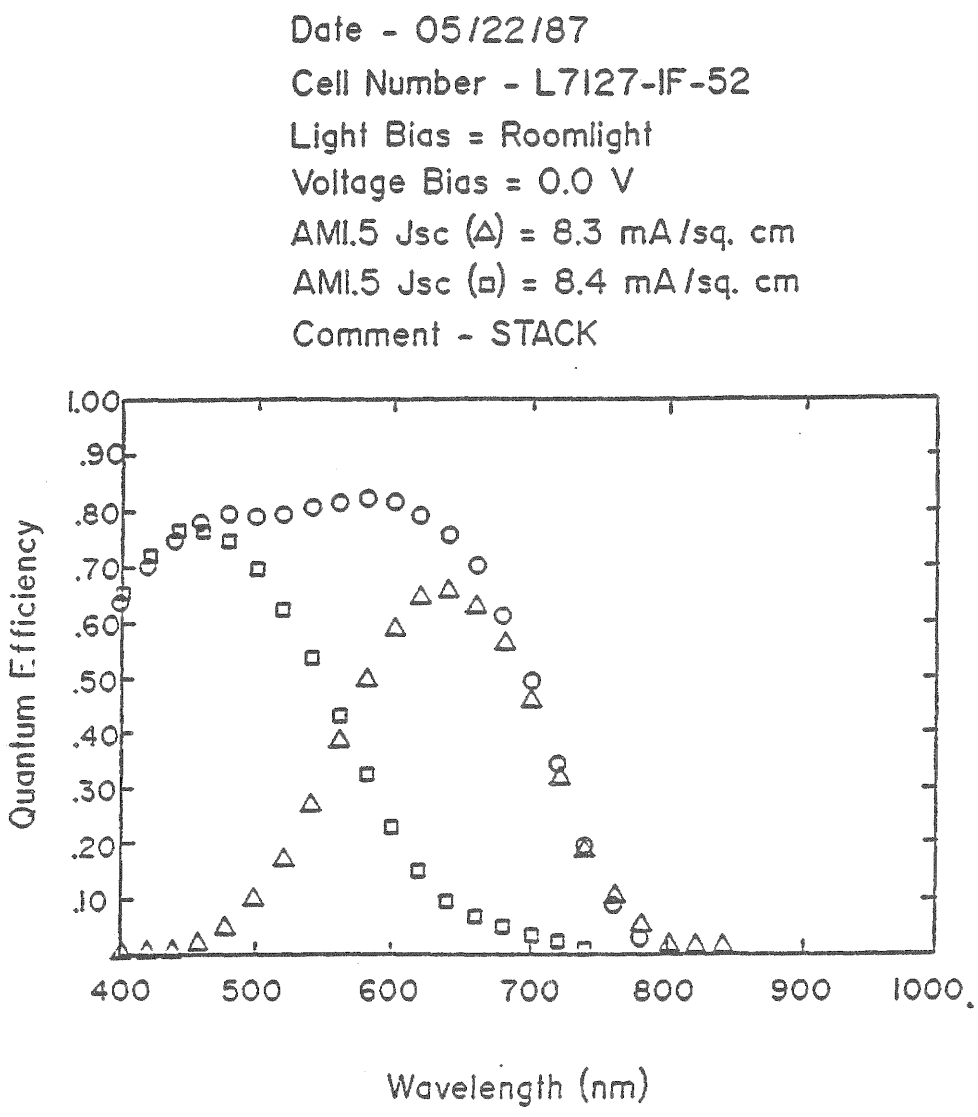

FIGURE 2-19 QUANTUM EFFICIENCY OF DEVICE IN FIGURE 2-18

FIGURE 2-20 J-V CHARACTERISTICS OF a-SiC/a-SiGe STACKED CELLS WITH A 10.5% CONVERSION EFFICIENCY.

Cell No. LL7217-3-3 TIAR	Date 870810
Voc = -1.722 Volts	Jsc = 9.11 mA/cm^2
F.F. = .670	Eff = 10.51%
Power = 10.51 mW/cm^2	Illum. = 101.01 mW/cm^2
V max = -1.354 Volts	J max = 7.76 mA/cm^2
Rs = 2.26E+01 ohm/cm^2	Rsh = 6.67E+03 ohm/cm^2
Temp = 24.1 deg. C	Cell Area = .755 cm^2

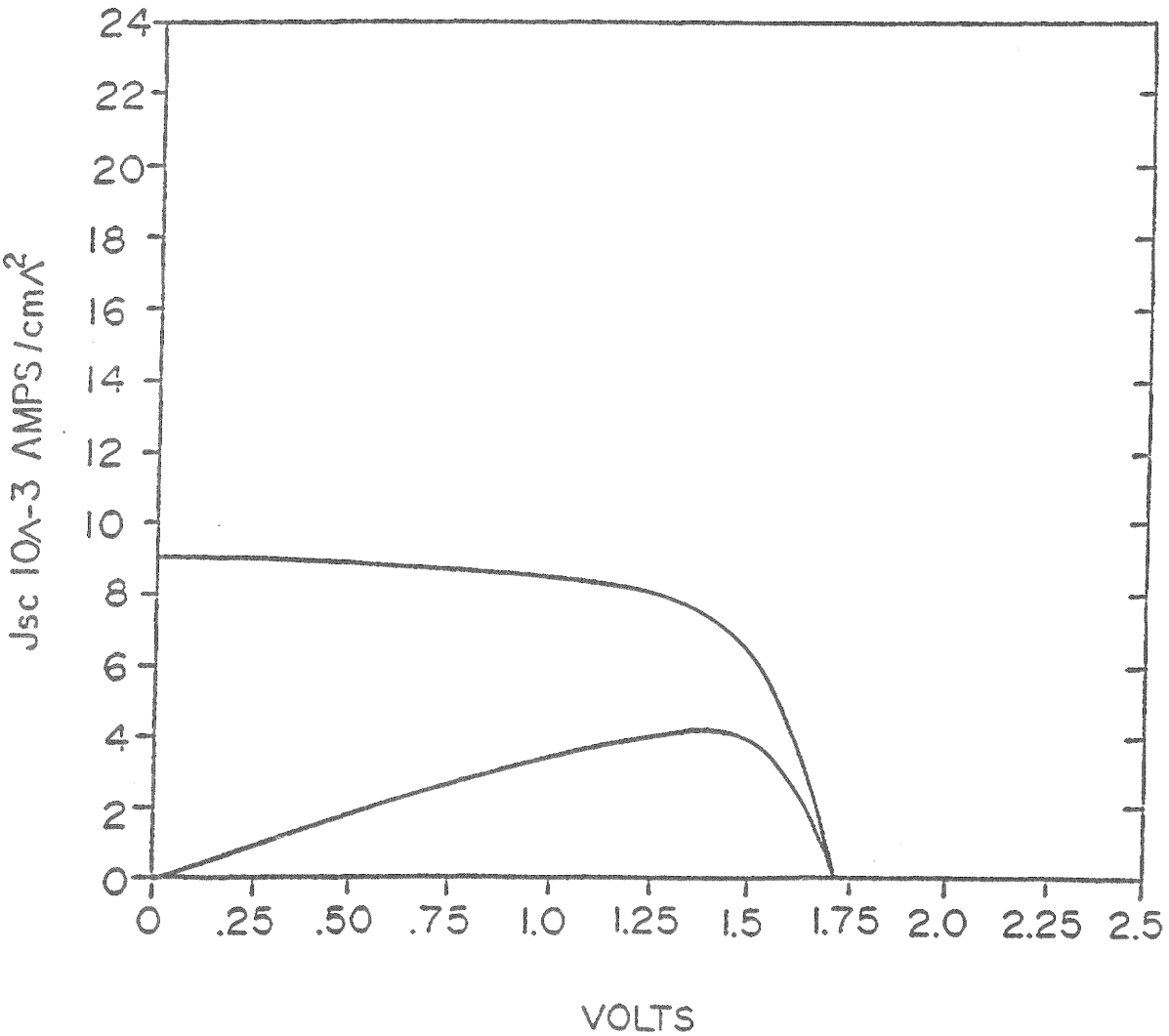

the following photovoltaic parameters: V_{oc} = 1.7222V, J_{sc} = 9.11mA/cm^2, and fill-factor = 0.67. Figure 2-21 shows the quantum efficiency versus wavelength measurement of this device. The cell measurements were verified at SERI where a conversion efficiency of 10.3% was measured.

Multi-junction (triple) solar cells have been fabricated in which the top most cell is either a-SiC or a-Si, the middle cell is a-Si, and the bottom cell is either a-SiGe:H alloy with bandgap of about 1.4eV or with a bandgap of 1.5eV. The highest conversion efficiency has been achieved on a triple stacked cell with a 1.4eV bandgap bottom cell. The conversion efficiency of this cell was 8.8% with the following parameters: V_{oc} = 2.107V, J_{sc} = 6.1mA/cm^2, and FF = 0.681. Figure 2-22 shows the J-V characteristics of this cell and Figure 2-23 shows the quantum efficiency measurements. The J-V measurements were made under a single source Xenon simulator which is quite deficient in the red part of the spectrum. Moreover, the simulator is calibrated to global AM1.5 spectrum by using a silicon cell with a BG-38 filter on it which simulates an a-Si:H single junction cell. We are in the process of setting-up a multi-source simulator for indoor measurements. Until such measurements are done the accuracy of J-V measurements on multi-junction cells with high response in the red part of the spectrum will remain doubtful. Some of these difficulties and the progress made in this direction is discussed in the next section. Nevertheless, these triple stack cells show excellent response at 800nm and beyond.

2.5 MEASUREMENT OF MULTI-JUNCTION CELLS

Substantial improvements have been made in our ability to measure the quantum efficiency of two- and three-junction devices. Procedures have been worked out which allow us to apply the appropriate electrical bias across and optical bias on a device in order to measure each of the individual junctions at any arbitrary voltage bias. These procedures have been incorporated into the software which controls the measurement.

In order to isolate a single component of a stacked device for spectral response measurement, appropriate conditions of light bias must be applied. These conditions of light bias put the device in a state in which the overall response of the device is determined entirely by the response of that component which is to be measured, or equivalently, put it in a state in which the junction of interest is generating far less current than the remaining components (see Figure 2-24 for a three-junction device). In order to achieve this state those components of the device other than the one under investigation must be flooded with light. This is accomplished by means of a bias light or lights, the color of which is determined according to Table 2-5 below. The intensity of the bias light is not critical but is normally set at about 5-10mW/cm^2.

Having optically isolated that component to be measured, it is necessary to establish some voltage bias across it. Typically, for example, one wants to measure the spectral response of a particular component at 0V. Since the same current must flow through all junctions, under any of the conditions of light bias described above the component(s) being flooded with bias light are pinned at a bias very close to V_{oc} (see Figure 2-24). Thus if an external bias, V_{app}, is applied to the device, an amount equal to the open circuit voltages of the two flooded components will be dropped across these components, the remaining portion, V_{comp}, positive or negative, will be dropped across the component which is being measured. The bias across the component which has been isolated optically will be given by

$V_{comp} = V_{app} - V_{oc}/2$ for a tandem and
$V_{comp} = V_{app} - V_{oc}/3$ for a triple.

It is important to realize that the open circuit voltage referred to above is that measured under the conditions of light bias being used in the measurement and not AM1.5 illumination. The above equations are approximate, but the approximation is reasonably good if each junction in the device has a good fill factor. In our apparatus,

FIGURE 2-21 QUANTUM EFFICIENCY OF DEVICE FROM FIG. 2-20

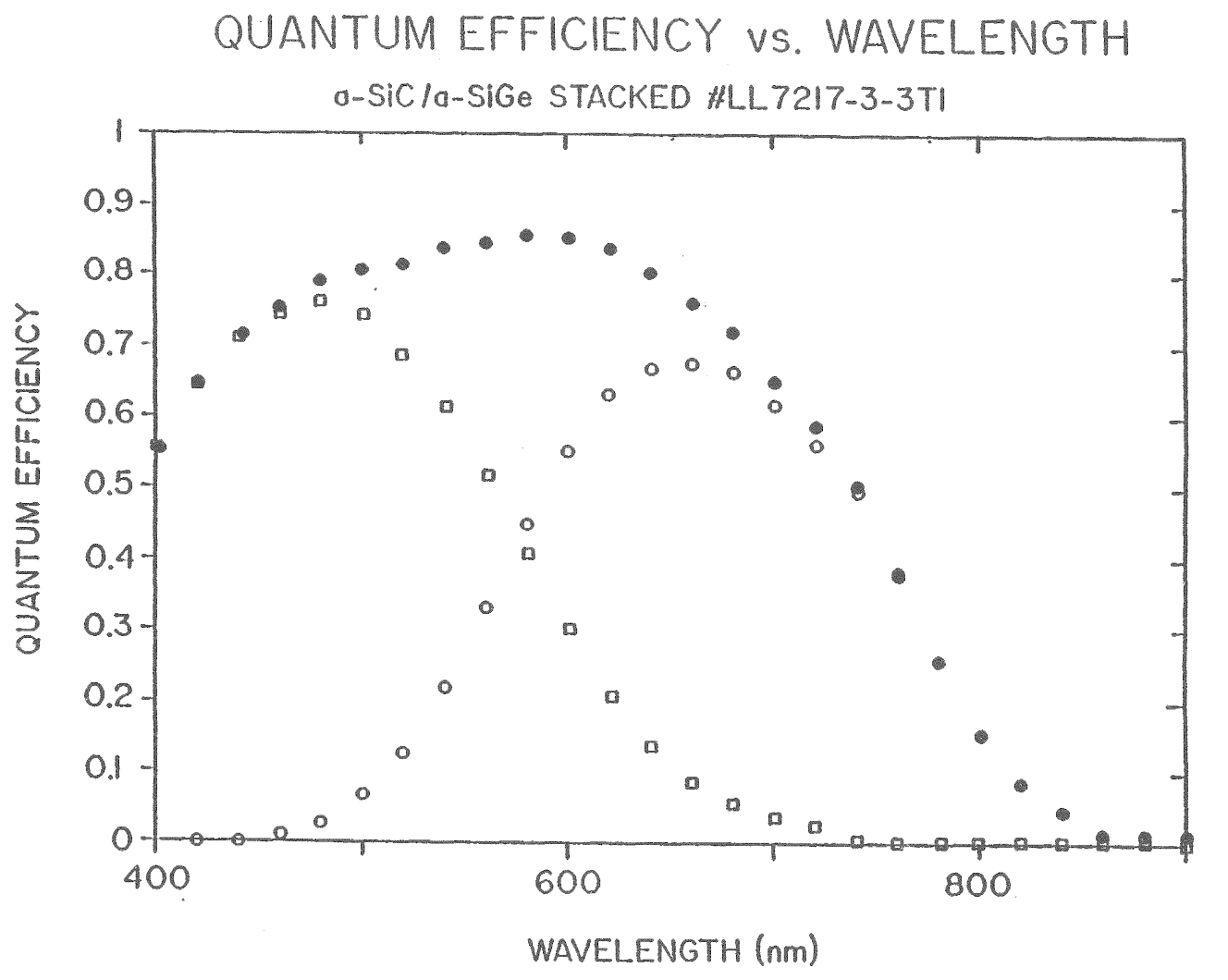

FIGURE 2-22 J-V CHARACTERISTICS OF AN a-SiC/a-Si/a-SiGe TRIPLE STACK CELL UNDER GLOBAL 1.5 ILLUMINATION.

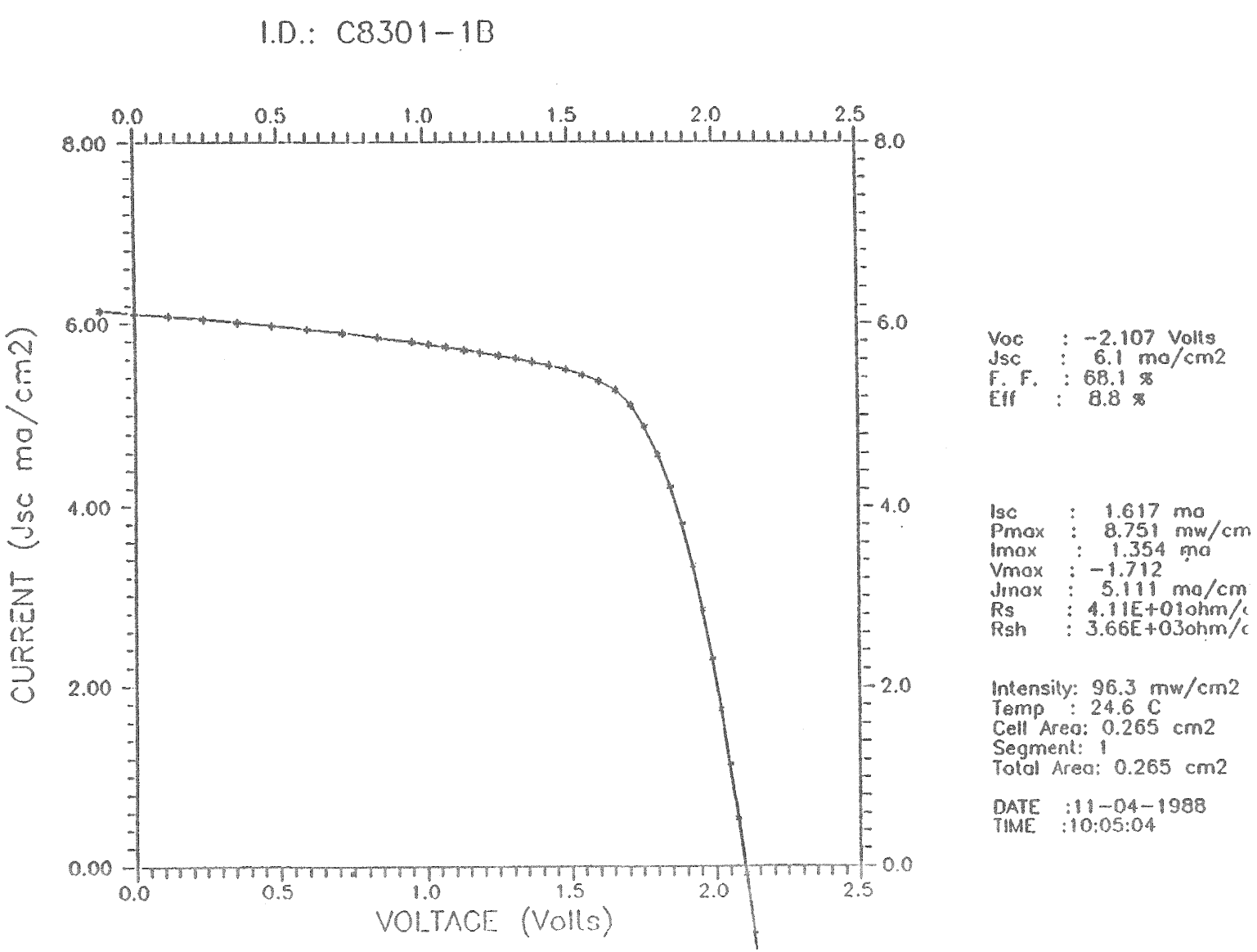

FIGURE 2-23 QUANTUM EFFICIENCY VERSUS WAVELENGTH MEASUREMENT OF THE CELL IN FIG. 2-22

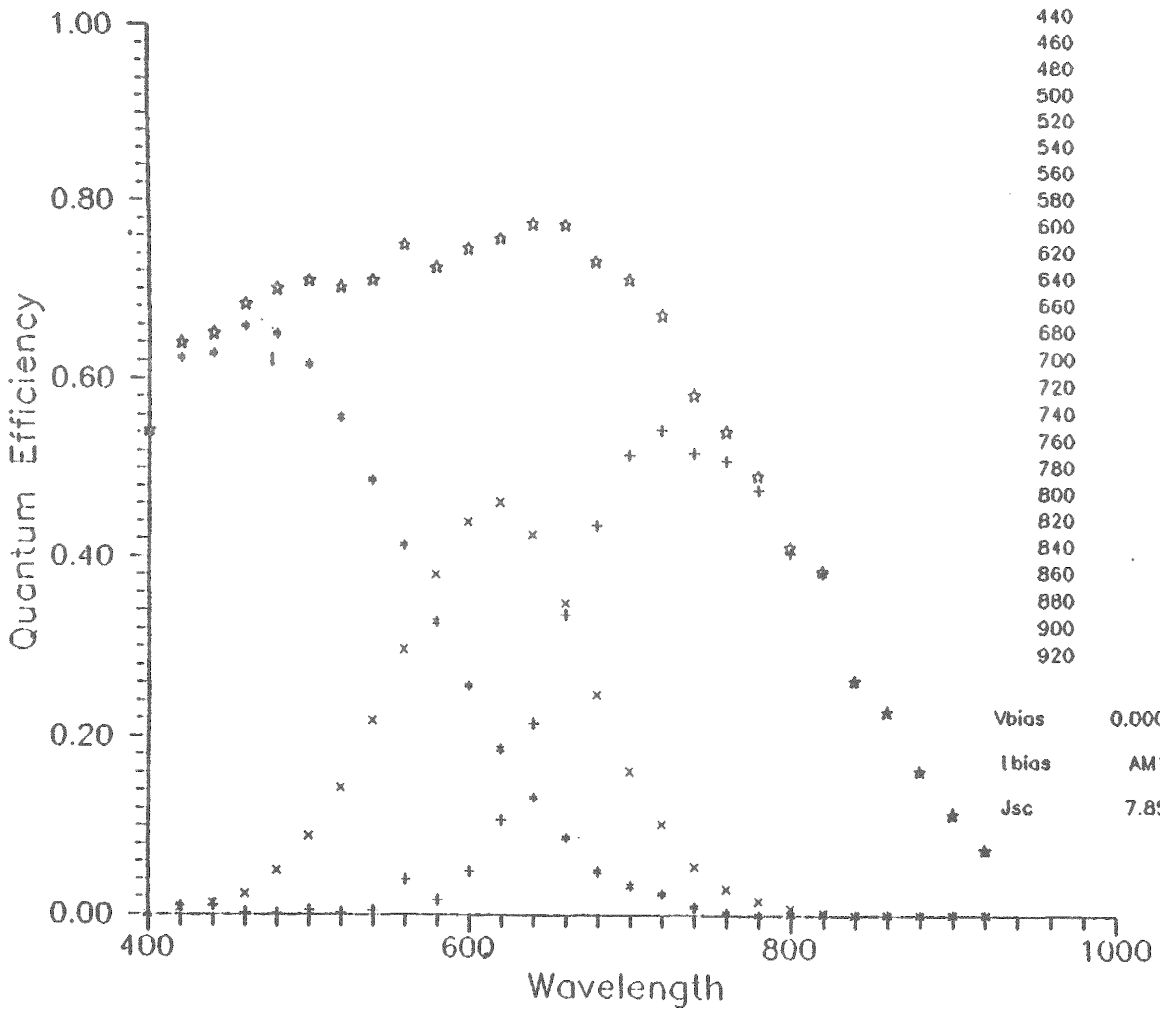

12-07-1988
C8301-1B S2
TRIPLE

	*	×	+	
400	.543	.000	.000	.543
420	.623	.008	.009	.640
440	.628	.012	.010	.650
460	.658	.023	.002	.683
480	.650	.050	.001	.701
500	.616	.089	.005	.710
520	.558	.143	.002	.703
540	.488	.219	.004	.711
560	.414	.298	.039	.751
580	.329	.381	.016	.726
600	.258	.440	.049	.747
620	.187	.463	.108	.758
640	.133	.426	.216	.775
660	.088	.349	.337	.774
680	.049	.248	.436	.733
700	.033	.162	.518	.713
720	.024	.103	.546	.673
740	.009	.055	.520	.584
760	.003	.029	.512	.544
780	.000	.016	.478	.494
800	.000	.007	.406	.413
820	.000	.002	.384	.386
840	.000	.000	.265	.265
860	.000	.000	.230	.230
880	.000	.000	.164	.164
900	.000	.000	.116	.116
920	.000	.000	.075	.075

Vbias	0.000	0.000	0.000
Ibias	AM1	AM1	AM1
Jsc	7.85	5.15	7.79

FIGURE 2-24 SCHEMATIC REPRESENTATION OF THE J-V CHARACTERISTICS OF THE COMPONENTS OF A THREE JUNCTION DEVICE WHERE TWO ARE FLOODED AND THE THIRD IS LIMITING. IN THIS REPRESENTATIVE THE ENTIRE DEVICE IS HELD AT 0V BIAS.

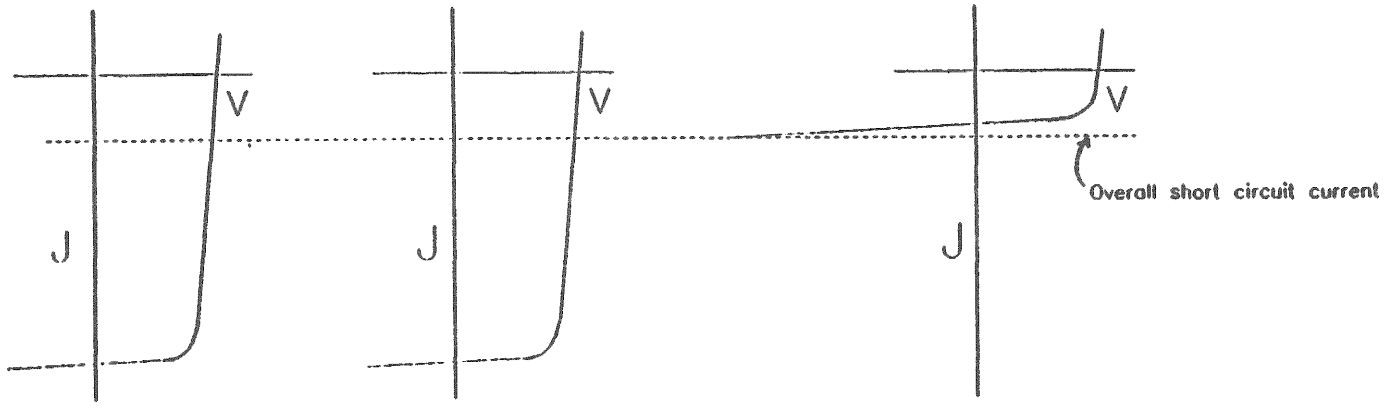

Components being flooded with light

Component being measured

TABLE 2-5

FILTERS USED FOR MEASUREMENT OF QUANTUM EFFICIENCY OF INDIVIDUAL JUNCTION IN TWO AND THREE JUNCTION STACKED CELLS

# of Junctions	Junction of interest	Filter(s) Used to Isolate
Two	Front	700nm interference
"	Back	450nm interference
Three	Front	700nm interference
"	Middle	Color glass filter*
"	Back	450, 600 interference**

*transmits below 470nm and above 740m.
**two beams, one filter in each.

V_{oc} is measured, then V_{app} is calculated and applied so that V_{comp} appears automatically across the junction of interest as desired.

Presently we make our current-voltage measurements under an Oriel solar simulator, matches the AM1.5 insolation to wavelengths solar simulator, matches the AM1.5 insolation to wavelengths up to about 750nm but is low in intensity in the infrared part of the spectrum. This is shown in Figure 2-25 which shows a spectroradiometric measurement of the output of our simulator compared to the AM1.5 global spectrum published by Bird et al. This indicates that the Oriel simulator is satisfactory up to about 750nm, an adequate range for a-Si devices but not for those with SiGe i-layers. Accordingly, we are presently constructing a multi-source simulator. In this approach we will use the simulator to cover the 300-700nm range, however the infrared part of the spectrum will be provided by means of a second, incandescent source.

2.6 LIGHT INDUCED EFFECTS

In the beginning of this year a great deal of work was done on the kinetics of stacked devices. The rates of degradation of multi-junction devices were determined in terms of the rates of degradation of the component junctions. These results were described in the previous semi-annual report and were also presented at the last IEEE conference in Las Vegas. To summarize briefly, the improved stability of multi-junction cells results from two factors. Most importantly, the very thin front junction(s) are nearly stable and tend to stabilize the overall device. In addition, the thicker back junction(s), which are less stable, are shaded to some extent by the front junction(s), thereby delaying the onset of their degradation. Our best thin a-Si/a-Si tandem cells with average initial efficiencies of 8.96% degrade to 7.7% after 1150 hours of continuous light soaking at open-circuit voltage on a Na-vapor lamp (100mW/cm^2) (Figure 2-26).

Although this work was done on all silicon devices, it can be used to predict the rate of degradation of multi-junction devices containing alloyed i-layers. However, first the kinetics of the individual alloyed junctions have to be known. To this end, single junction devices containing the structures typically used in stacked devices are now under investigation. There is a difficulty, however, in that the structures of alloy junctions, at least in the case of SiGe, are often very complex, involving, in most cases, several graded layers, and can very greatly from one design to the next. While it is not possible to catalog every design individually, single junction cells which will incorporate these features in a generic way are being made in order to investigate the effects of the various design features on stability. The first set of single junction cells to have been light-soaked were SiGe cells containing no grading so that the structure is a simple p-i-n device with a SiGe i-layer. The doped layers were held the same throughout the run. Thus the efficiencies were not optimized, and there is a possible complication due to differences in band discontinuities as the Ge content increases. Nonetheless, as shown in Figure 2-27, the rate of degradation increases as Ge is added to a bandgap of about 1.5eV, then decreases until the devices are more or less stable. This stability may only be apparent and may result from the very poor initial efficiency, however it appears more likely to reflect relatively stable material. Witness the effect of adding C when making cells with SiC i-layers. With relatively large amounts of C the initial efficiency may be very close to zero, nonetheless, unlike the SiGe cells the SiC cells degrade very rapidly. It can be seen that the least stable device has about twice the degradation rate of a-Si. The light-soaking of all devices was carried out on the same lamp so that the intensity was somewhat higher for the lower bandgap devices. Based on experience with a-Si devices, however, even a factor of two in intensity is barely perceptible when plotting efficiency against the logarithm of time, thus the initial increases in degradation rate with decreasing bandgap is not an artifact of the light-soak method. Further investigations are underway on SiGe devices containing one or more graded layers.

These studies are intended to help explain and predict the rates of degradation of multi-junction devices containing alloy i-layers. Thus, simultaneously we are measuring the rates of degradation of multi-junction devices which incorporate SiGe i-layers corresponding to the single junction devices described above.

FIGURE 2-25 SPECTRAL IRRADIANCE OF SOLAREX'S RESEARCH SOLAR SIMULATOR COMPARED TO MODEL DATA PUBLISHED BY BIRD et al.

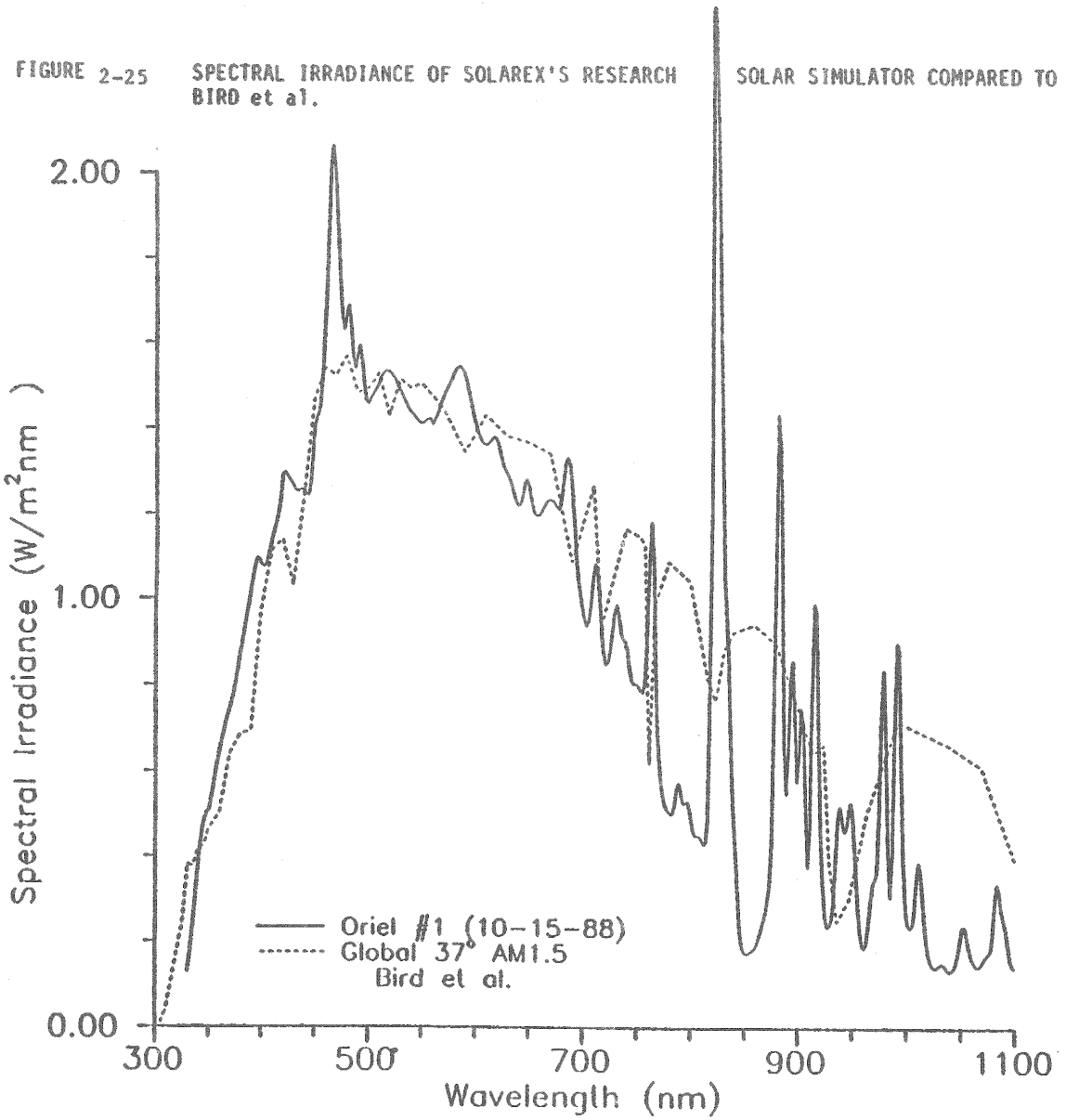

FIGURE 2-26 EFFICIENCY VS. TIME OF 7.7% Si/Si STACKED CELL.

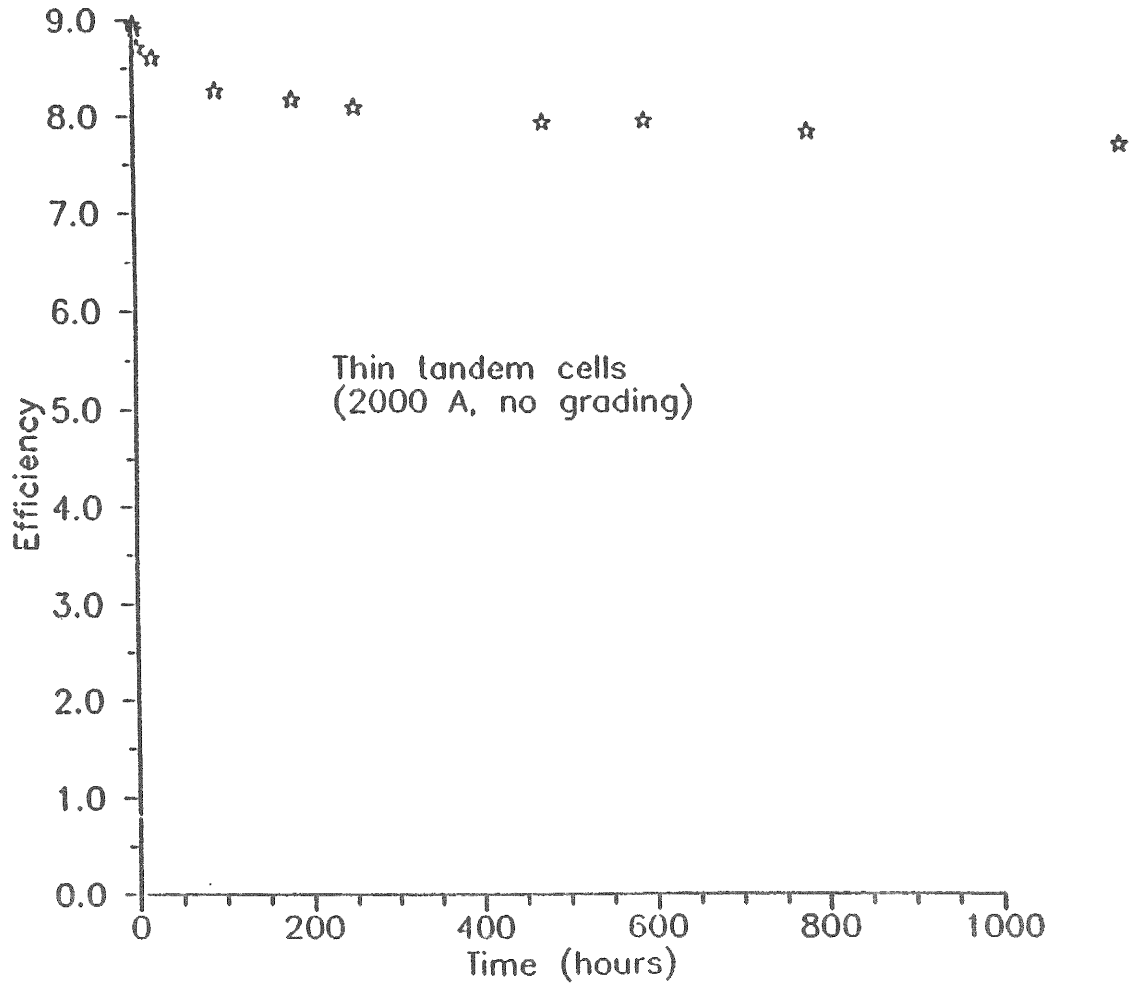

FIGURE 2-27 RATES OF DEGRADATION OF SiGe SOLAR CELLS AS A FUNCTION OF THE BANDGAP OF THE i-LAYER MATERIAL. THE UNITS OF THE y-AXIS SHOULD BE MORE COMPLETELY WRITTEN AS % LOSS OF INITIAL EFFICIENCY PER DECADE OF TIME. BECAUSE EFFICIENCY DECREASES LINEARLY WITH THE LOGARITHM OF TIME, THESE ARE UNITS OF SLOPE.

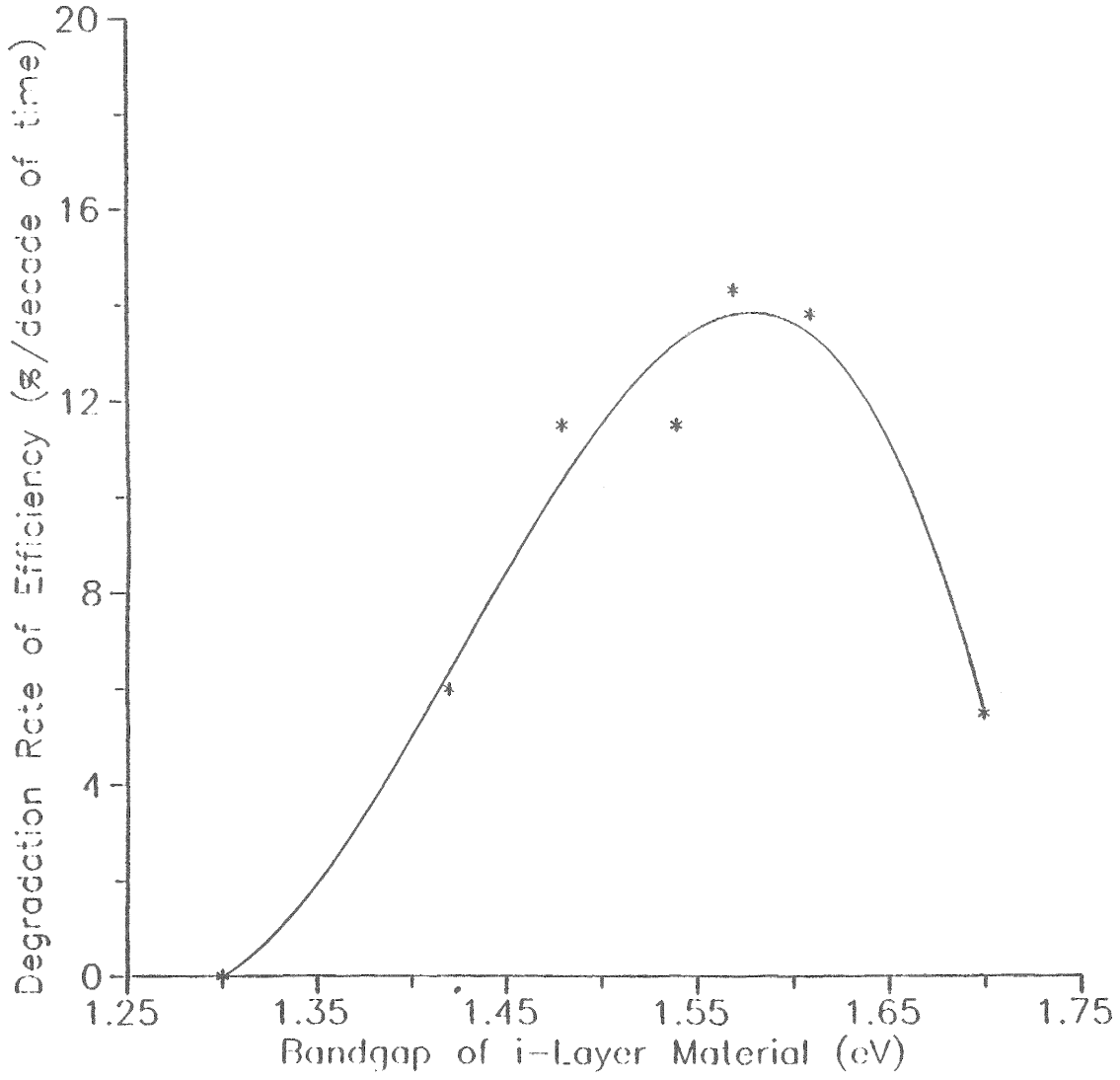

3.0 NON-SEMICONDUCTOR MATERIALS RESEARCH

3.1 ABSORPTION ENHANCEMENT IN a-Si:H SOLAR CELLS

3.1.1 Introduction

Enhancement of absorption of long wavelength radiation (>600nm) is of continued interest due to the large current gains which may be realized. To direct efforts to maximize absorption enhancement in a-Si:H solar cells, the light losses occurring in the structure are determined. The results of modeling the a-Si:H single junction solar cell structure are summarized below.

3.1.2 Optical Modeling

In the a-Si:H solar cells, the enhancement of absorption in the i layer is limited by absorption of radiation in the inactive layers of the structure. Deckman, et al. considered the effect of these parasitic absorptions on the absorption occurring in the i layer, viz.,

$$1-\exp(-\alpha I_I l_I)+ \frac{(\exp(-\alpha_I l_I(\,1-\exp(-2\,\alpha_I l_I))(1-\eta_r)[\exp(-2\alpha_I l_I)(1-\eta_f)(1-(1/n_I)^2)+\,1]}{1-\exp(-4\alpha_I l_I)(1-\eta_r)(1-\eta_f)(1-(1/n_I)^2)} \qquad (3\text{-}1)$$

where:

n_f = parasitic absorption of front contact

n_r = parastic absorption of the rear contact

n_I = index of refraction of i-layer

α_I = absorption coefficient of i-layer

ℓ_I = thickness of i-layer

The above expression differs from that of Deckman, et al., in that, here, first pass absorption is treated separately from subsequent passes and the front and rear contact absorptions are treated individually. In developing this expression it was assumed that radiation reflected off the rear contact is scattered in Lambertian distribution.

If the fraction of the radiation incident upon the solar cell which enters the i-layer and the parasitic absorptions are known, the above expression may be used to predict the i-layer absorption. To obtain estimates of these quantities, a Lambertian angle averaged ray was followed through the various layers of the structure. The solar cell structure considered was: glass/textured tin oxide/a-Si:H p-i-n/rear contact. The rear contact was a metal or ITO (indium tin oxide)/metal. Figures 3-1 to -4 summarize the expected optical transmission or absorption for the various layers in the device structure. Figure 3-1 illustrates the transmission of light into the i-layer in the model presented above. Figure 3-2 plots the absorption loss expected for the p-layer. The parasitic absorption due to the rear contact is plotted in Figure 3-3 for molybdenum and aluminum contacts. Note that aluminum is far superior to molybdenum. Figures 3-4 and -5 illustrate the parasitic absorption for ITO/Mo and

FIGURE 3-1 LIGHT TRANSMITTED INTO THE I-LAYER AS A FUNCTION OF WAVELENGTH FOR THE MODE DISCUSSED IN THE TEXT.

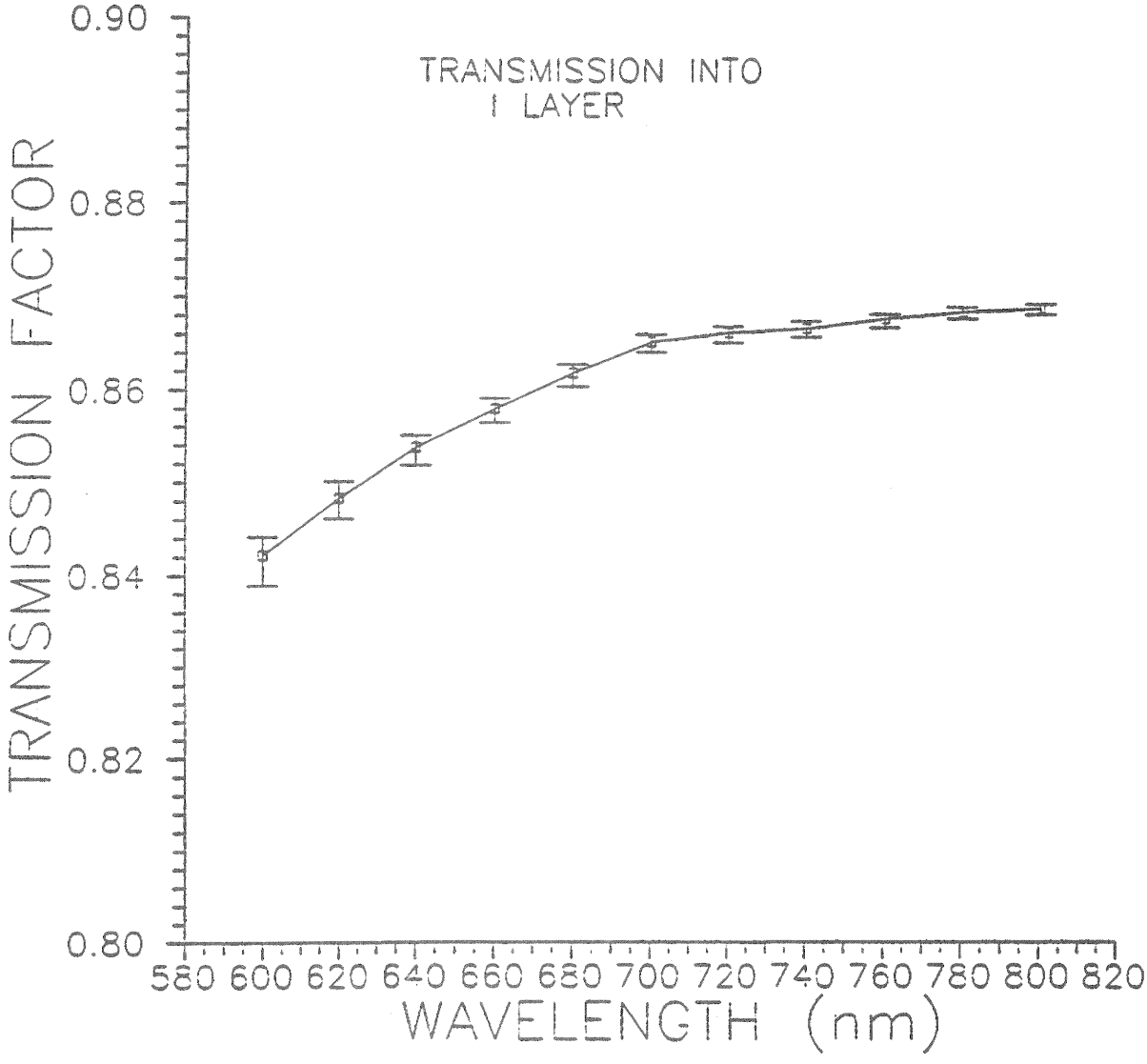

FIGURE 3-2 ABSORPTION LOSS EXPECTED FOR THE P-LAYER.

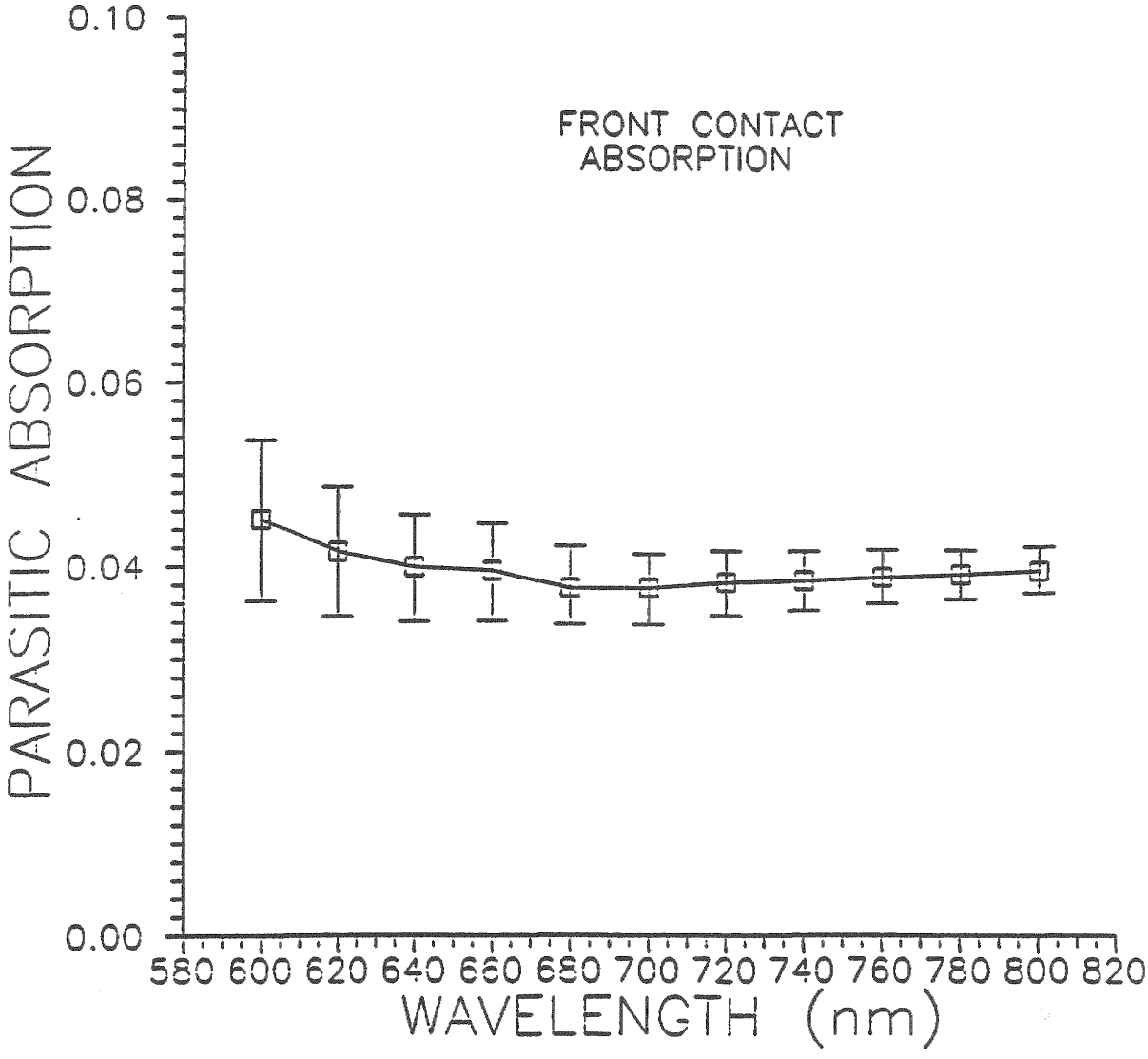

FIGURE 5-3 PARASITIC ABSORPTION DUE TO Al AND Mo REAR CONTACTS

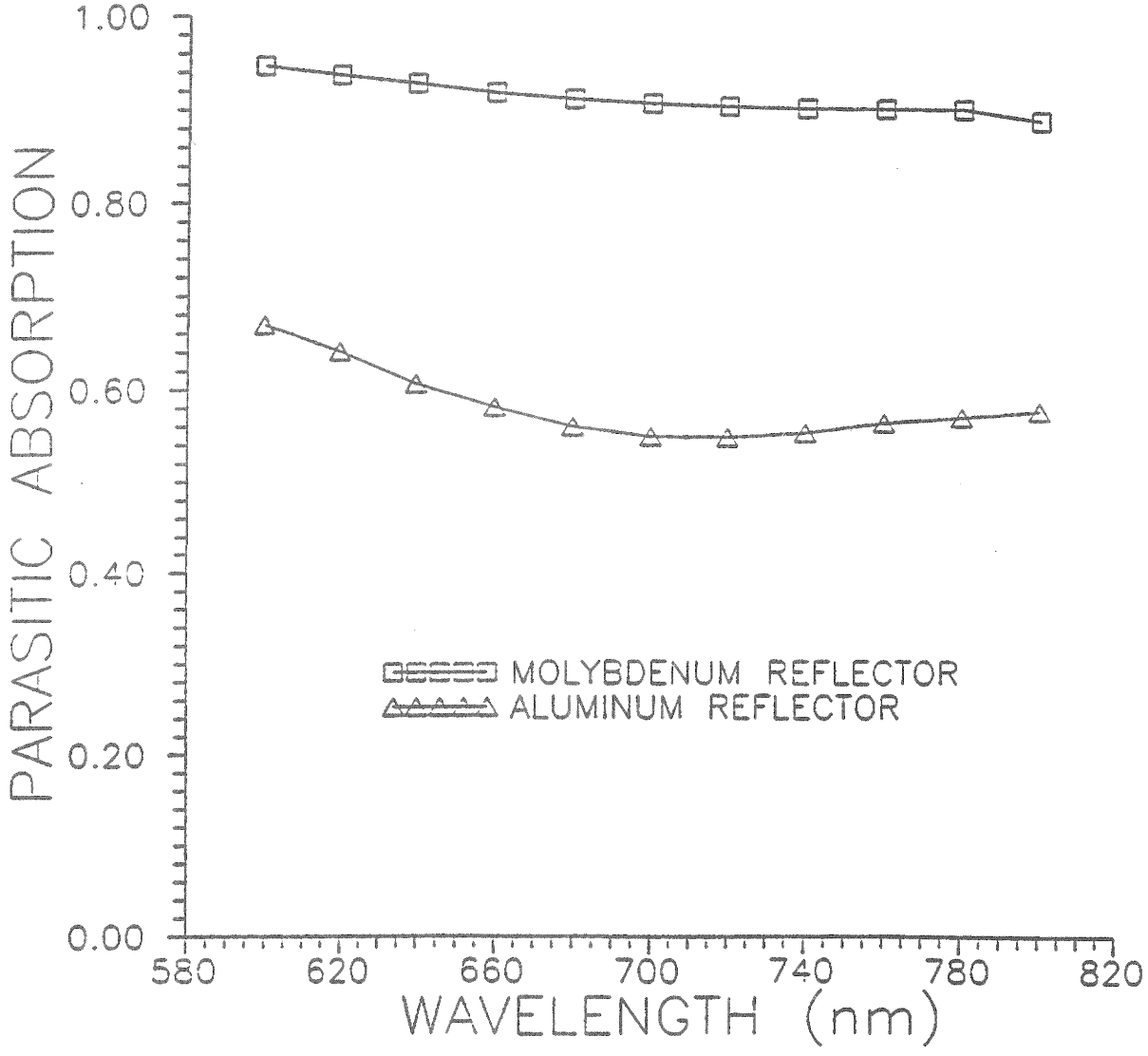

FIGURE 3-4 PARASITIC ABSORPTION FOR ITO/Mo REAR CONTACTS.

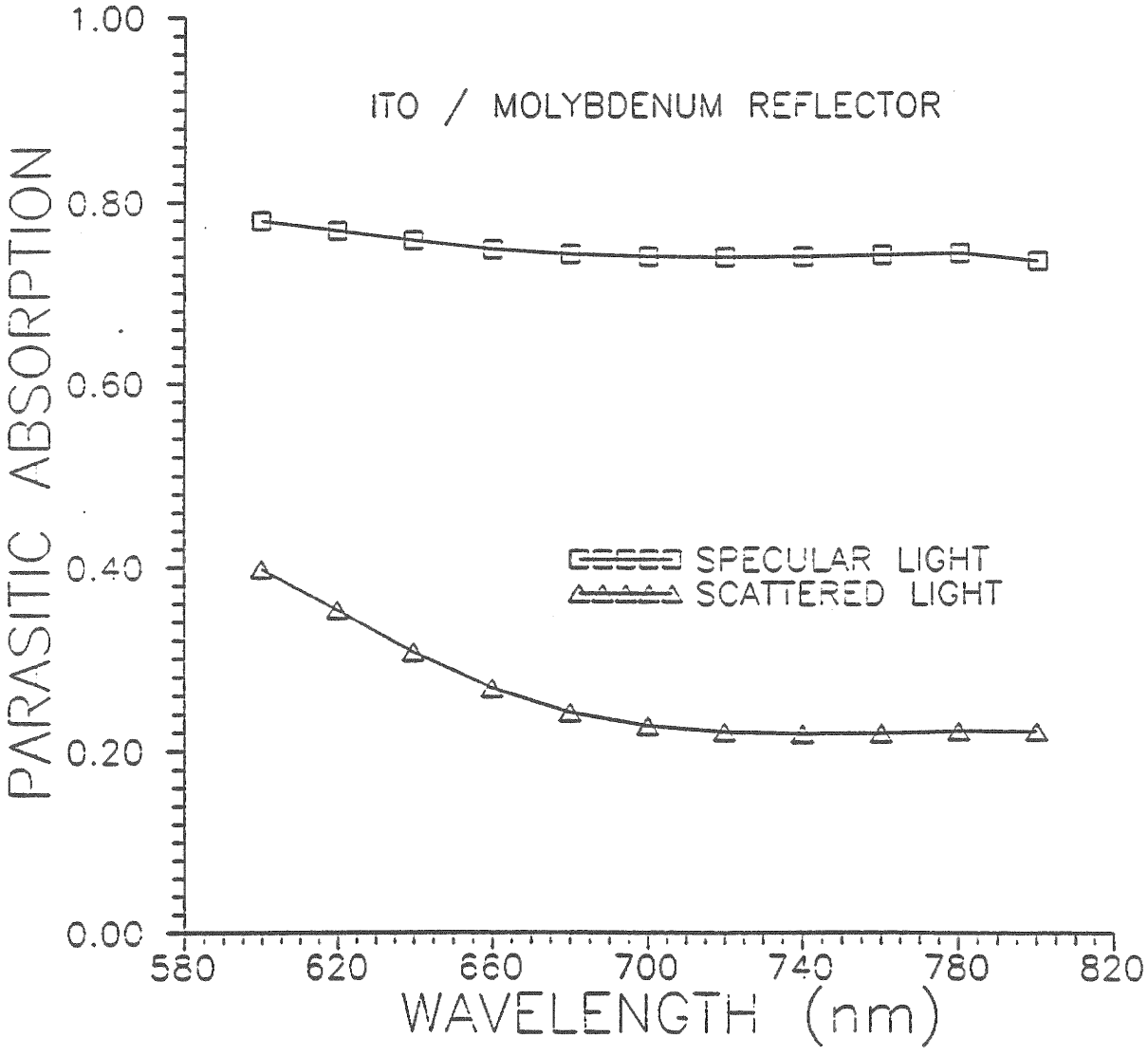

FIGURE 3-5 PARASITIC ABSORPTION FOR ITO/Ag REAR CONTACTS.

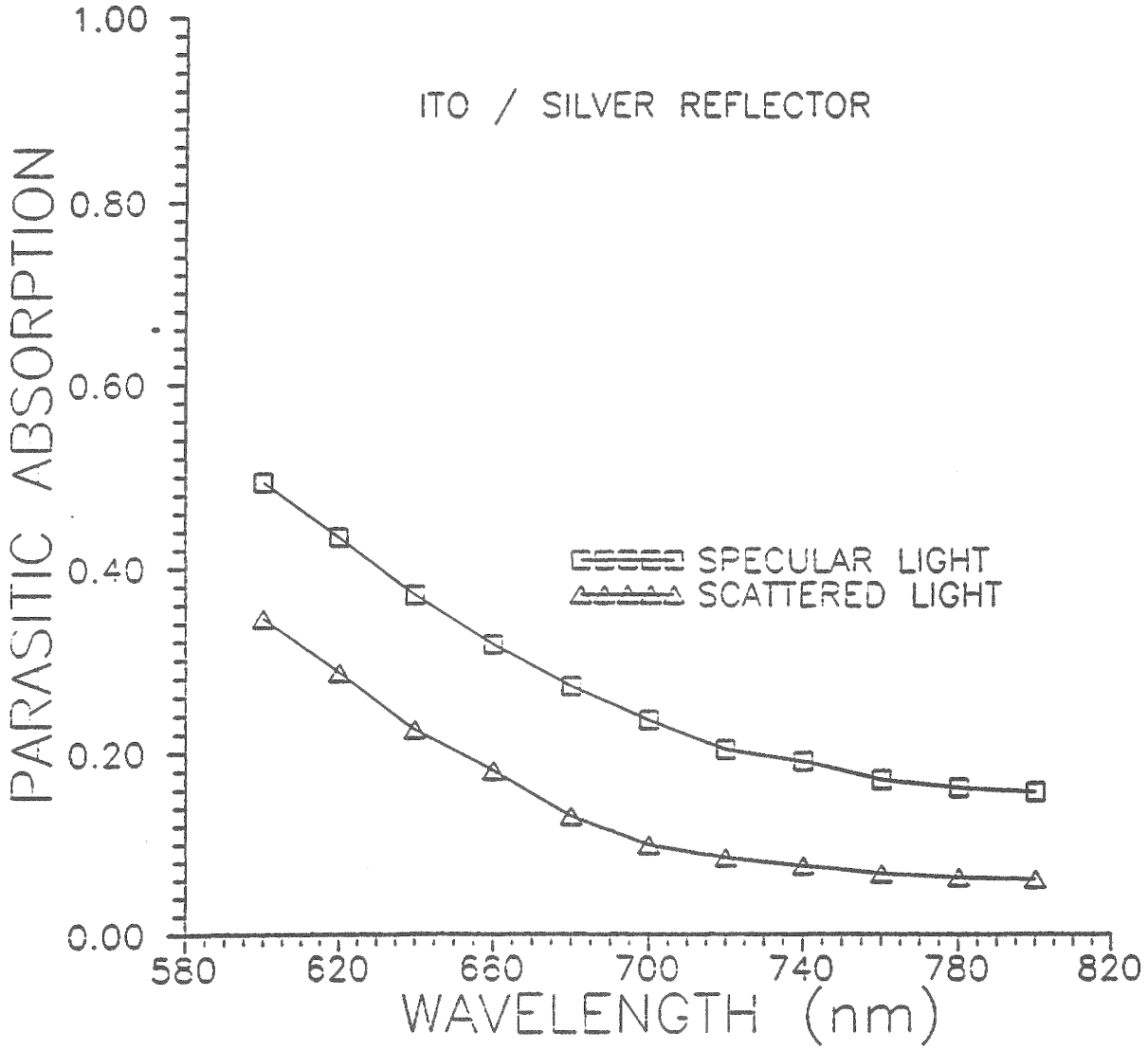

ITO/Ag rear contacts. Both the specular and trapped case are illustrated. Either metal contact in combination with ITO is far superior to the metal contact above, and as expected the ITO/Ag combination has extremely low absorption, which coupled with high reflectivity makes this contact an outstanding choice.

Figures 3-6 thru -9 illustrate the expected long wavelength QE, for Mo, Al, ITO/Mo and ITO/Ag. Good agreement with experiment is seen in all but the ITO/Ag contact. This discrepancy is likely due to the particular sample used in this experiment. Generally higher QE's at long wavelength are observed.

In summary, the long wavelength response of a-Si:H solar cells is limited by the parasitic absorptions which are present in the structure. The absorption in the rear contact is, in most cases, the major loss mechanism.

3.1.3 Light trapping effects

Optical studies have shown that the degree of light trapping which has been achieved at long wavelengths (800nm) is significantly less than is theoretically possible. Light trapping by total internal reflection is usually incorporated in a-Si:H p-i-n devices by texturing the front conductive transparent oxide (CTO) layer. The degree of texture, in turn, is a strong function of the CTO film thickness. The results of a study to determine the affect of textured tin oxide thickness on the long wavelength response of single junction a-Si:H and a-Si:Ge, p-i-n solar cells is summarized in Figures 3-10 - 12. CTO thicknesses of 8000Å, 16,000Å, and 32,000Å, were investigated. Figures 3-10 and -11 illustrate the ratio of the average long wavelength response of cells grown on 16,000 and 32,000Å thick textured tin oxide to the average response of the same devices grown on textured tin oxide of 8000Å thickness.

The average response of the cells grown on the thinnest tin oxide is initially higher than that of cells grown on the thicker layers. At longer wavelengths however, the average response of the solar cells grown on the thicker tin oxide layers increases above that of the cells grown on the tin oxide of 8000Å thickness. Figure 3-12 indicates the effect of increasing tin oxide thickness on the total current generated in the a-Si:H p-i-n solar cells. The increase in long wavelength response is not enough to compensate for the corresponding increase in light absorption of the thicker textured tin oxide layers.

3.1.4 Rear contact studies

As part of an effort to further optimize the ITO - silver rear reflector, a group of double stacked junction devices (a-Si:H/ a-Si:Ge) was used to determine the effect of ITO layer thickness of the response of the lower junction. The thickness of the ITO layer was varied from 1000Å to 5000Å. The response of the second junction was measured at a negative voltage of 1/2 V_{oc} and under blue light illumination. The results are summarized in Figure 3-13, which indicates the average response of the second junction as a function of the thickness of the ITO layer in the ITO - silver reflector. No statistically significant difference in response was found.

Multi-layer reflecting contacts deposited on large area series connected modules are subject to several post deposition processes. The large area contact must maintain optical, electronic, and mechanical integrity. In addition, uniform deposition over large areas is required. Initial attempts to utilize the ITO - silver reflector on series connected modules were unsuccessful due to the relatively poor adhesion of the silver film to the ITO layer. Modification of the deposition parameters (power, rate, etc.) did result in a significant improvement in the adhesion of silver, however the optical characteristics of the films were not optimum. Surface treatments of the ITO layer prior to silver deposition were also of limited success. Two approaches currently under development have shown promising results. Inserting a thin interlayer of Zinc Oxide between the ITO and silver layers has resulted in excellent adhesion and a spectral response of 0.569 at 700nm for a single junction, a-Si:H i-layer device. Sputtering of the ITO and silver films has also resulted in good adhesion and is currently under development.

FIGURE 3-6 COMPARISON OF THE CALCULATED AND MEASURED LONG WAVELENGTH QE FOR Mo CONTACT.

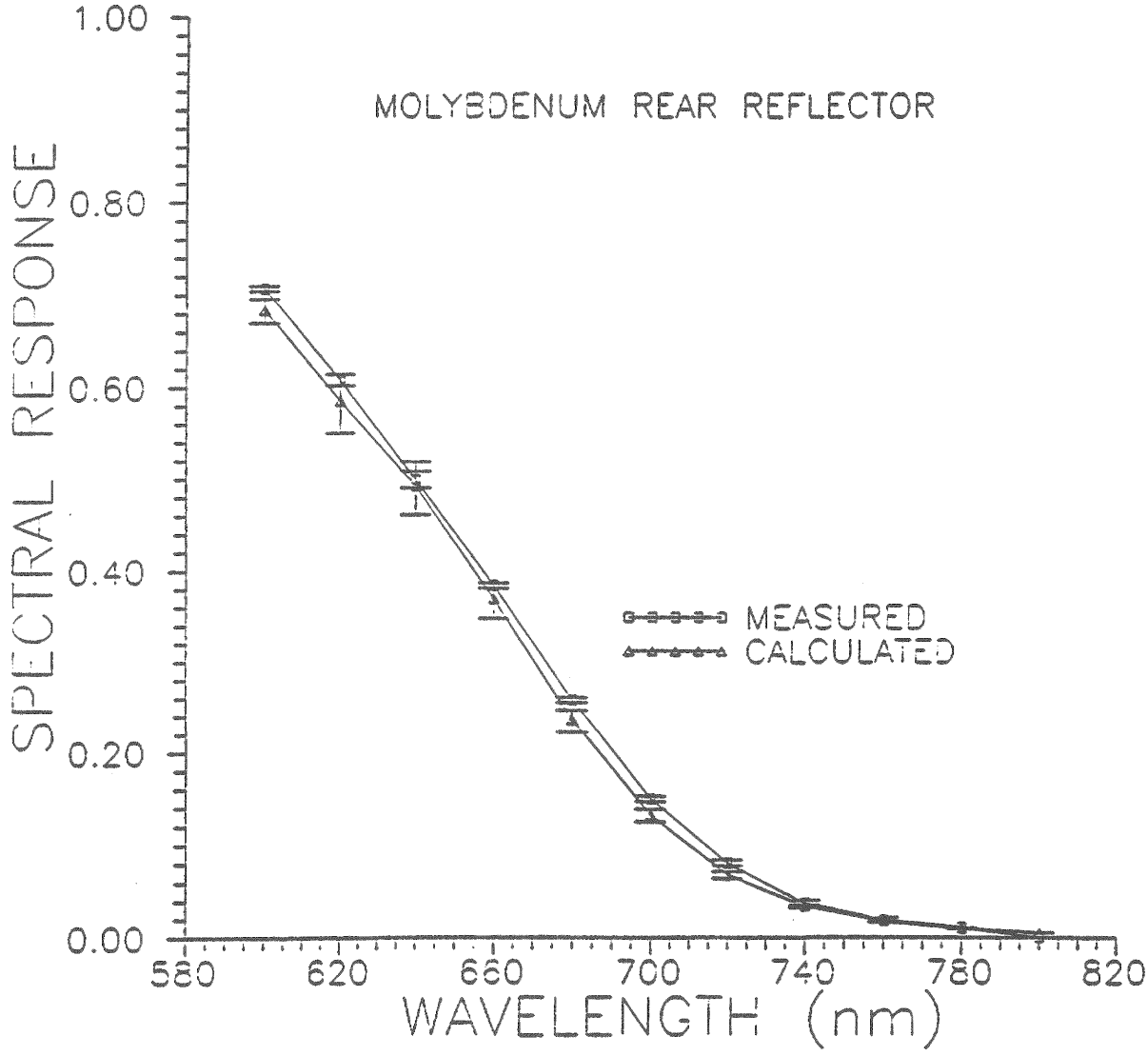

FIGURE 3-7 COMPARISON OF THE CALCULATED AND MEASURED LONG WAVELENGTH QE FOR Al CONTACT.

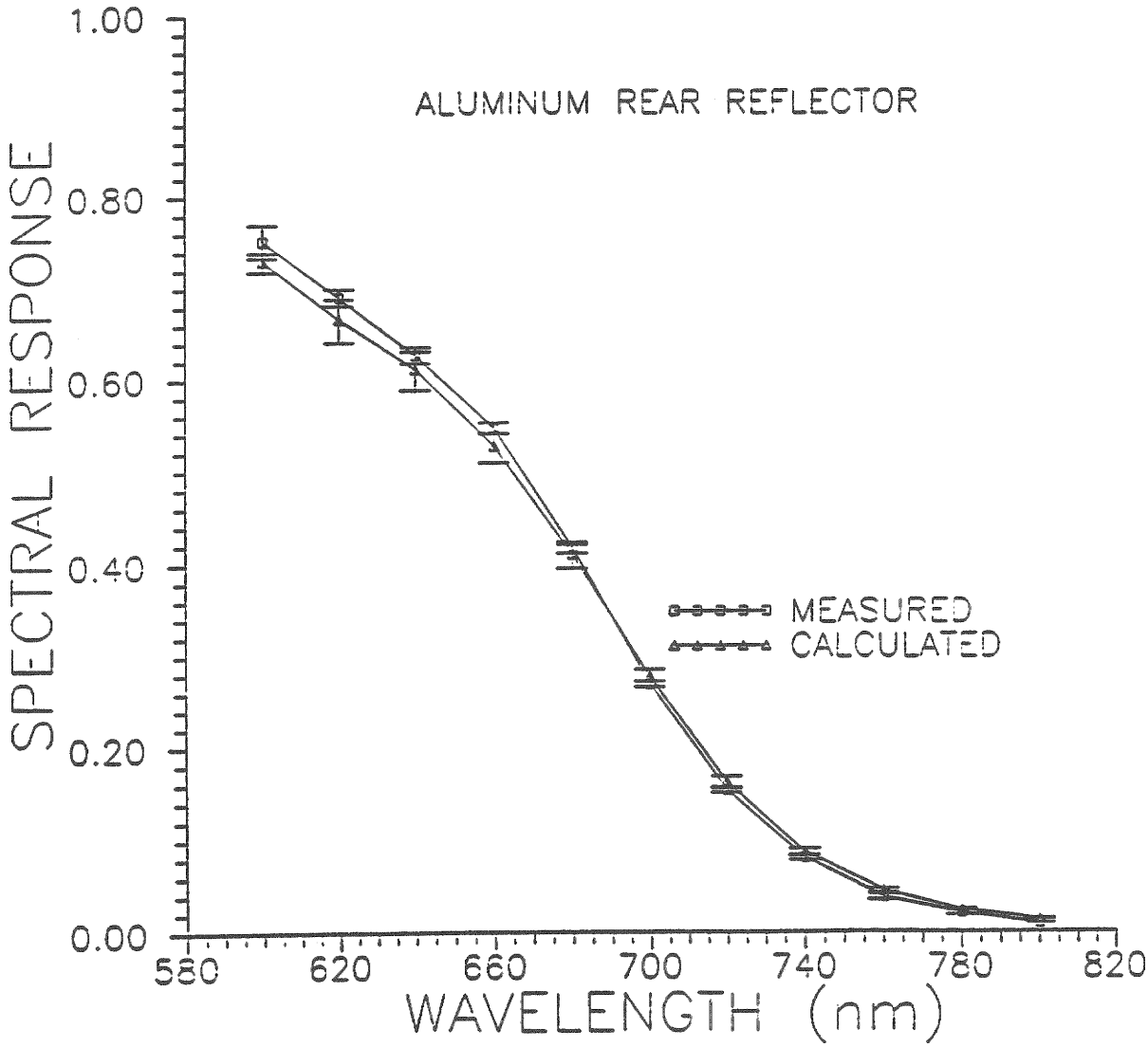

FIGURE 3-8 COMPARISON OF THE CALCULATED AND MEASURED LONG WAVELENGTH QE FOR ITO/Mo CONTACT.

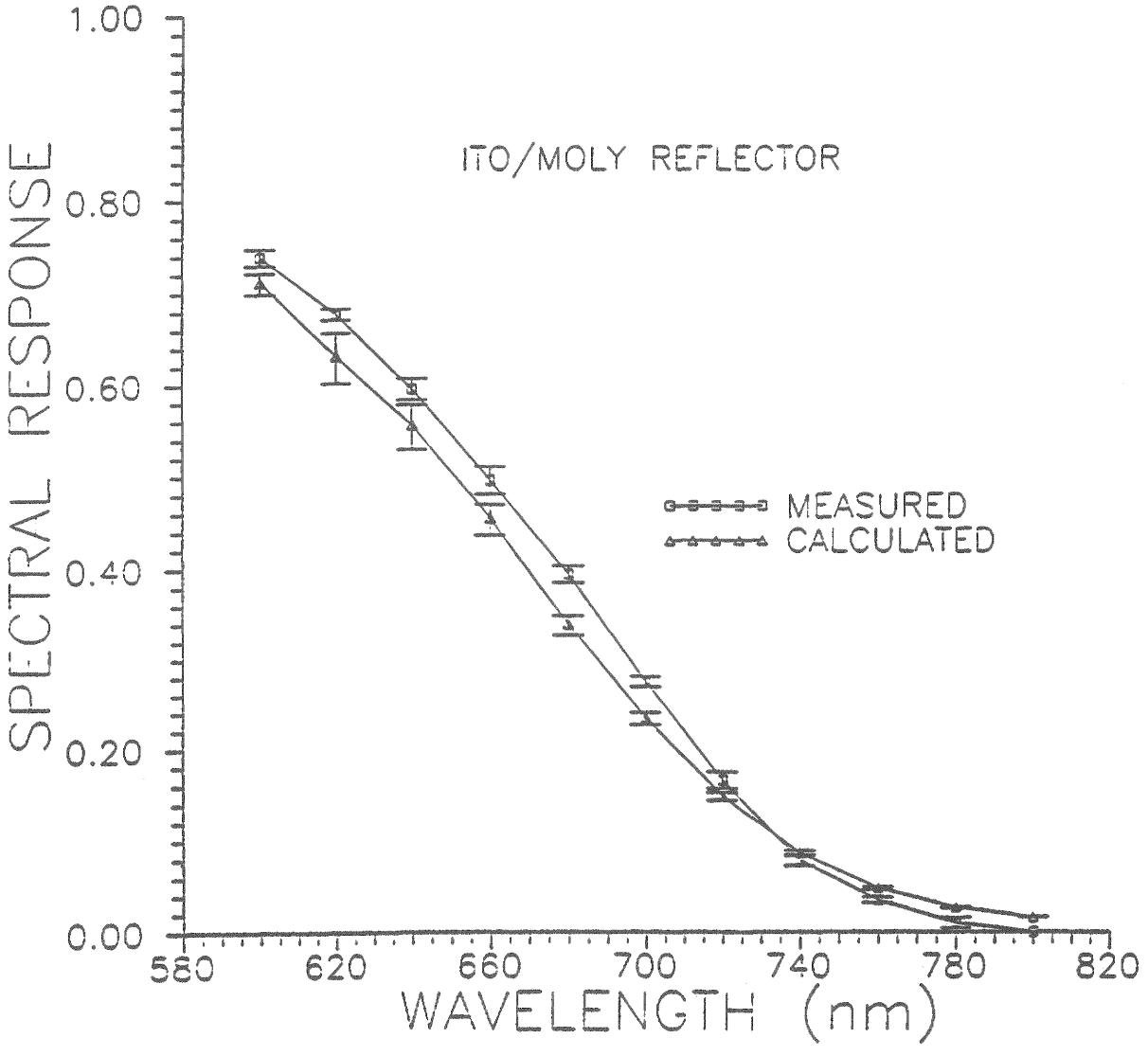

FIGURE 3-9 COMPARISON OF THE CALCULATED AND MEASURED LONG WAVELENGTH QE FOR ITO/Ag CONTACT.

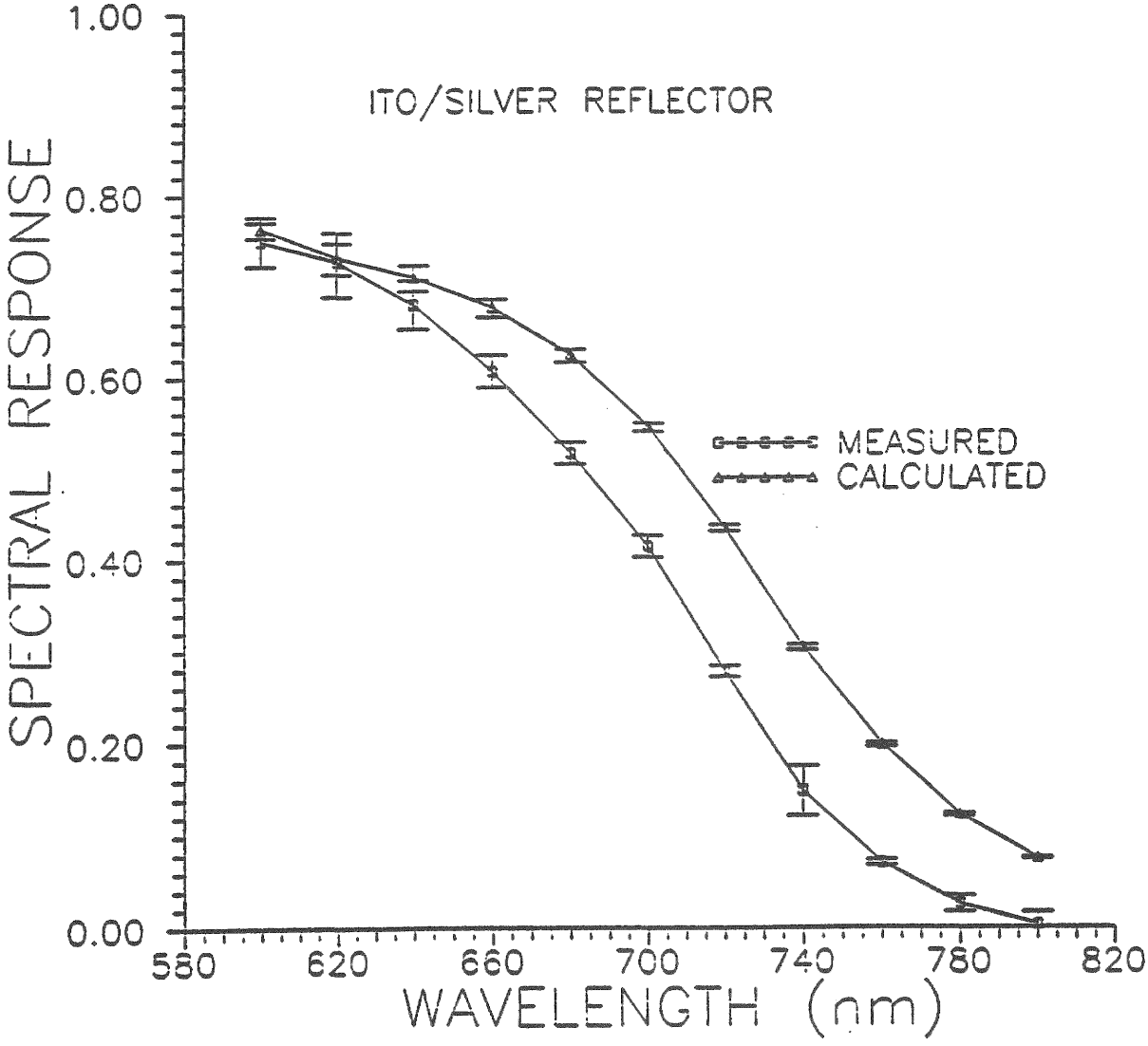

FIGURE 3-10 RATIO OF THE LONG WAVELENGTH RESPONSE OF SOLAR CELLS WITH a-Si:H i-LAYER ON THICK TEXTURED TIN OXIDE TO THE RESPONSE OF SOLAR CELLS ON TEXTURED TIN OXIDE OF 8000Å THICKNESS

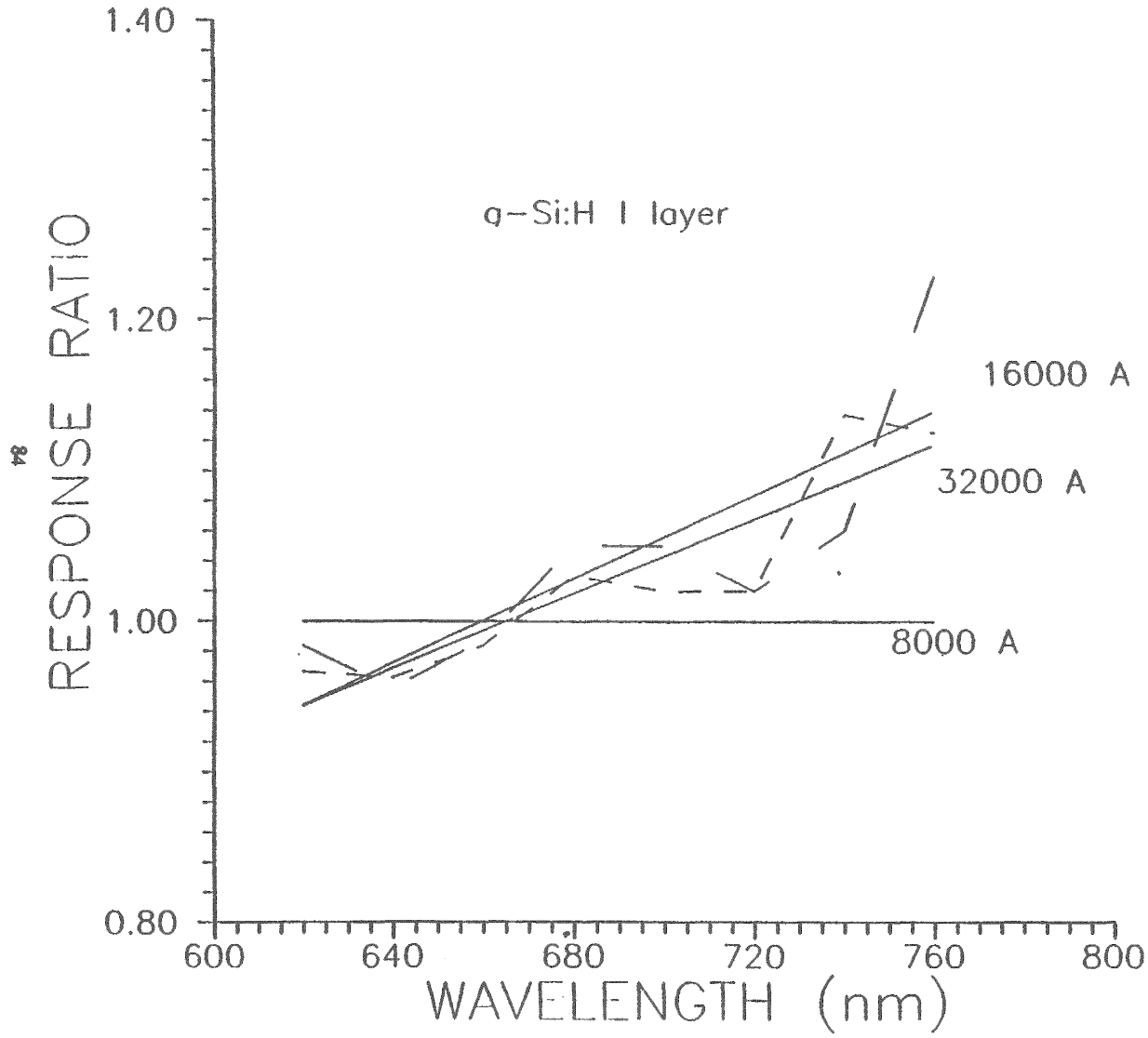

FIGURE 3-11 RATIO OF THE LONG WAVELENGTH RESPONSE OF SOLAR CELLS WITH a-SiGe i-LAYER ON THICK TEXTURED TIN OXIDE TO THE RESPONSE OF SOLAR CELLS ON TEXTURED TIN OXIDE 8000Å THICKNESS.

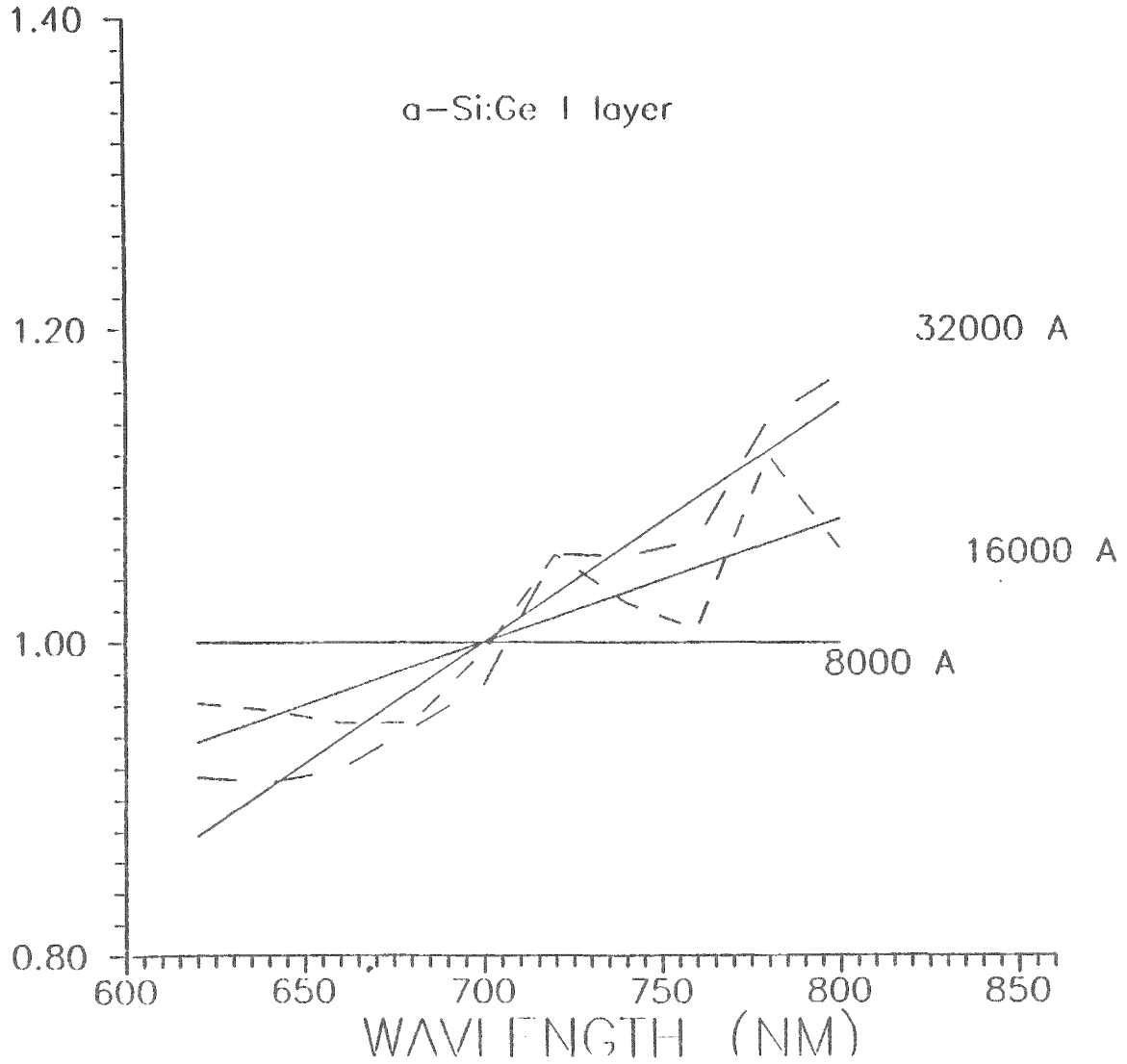

FIGURE 3-12 AVERAGE SHORT CIRCUIT CURRENT OF SOLAR CELLS AS A FUNCTION OF TEXTURED TIN OXIDE THICKNESS.

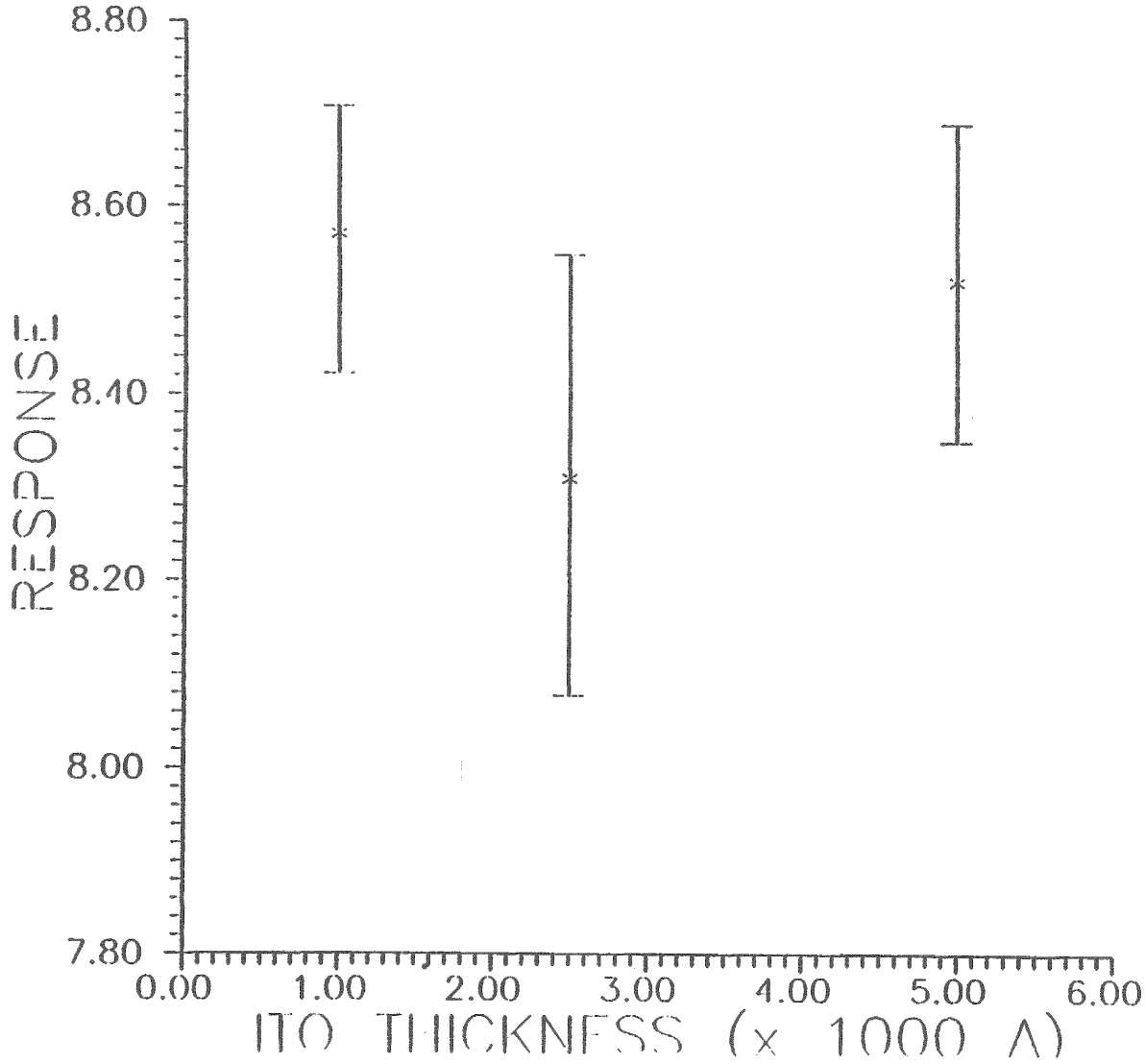

FIGURE 3-13 RESPONSE OF THE SECOND (LOWER) JUNCTION OF TANDEM CELLS AS A FUNCTION OF ITO LAYER THICKNESS.

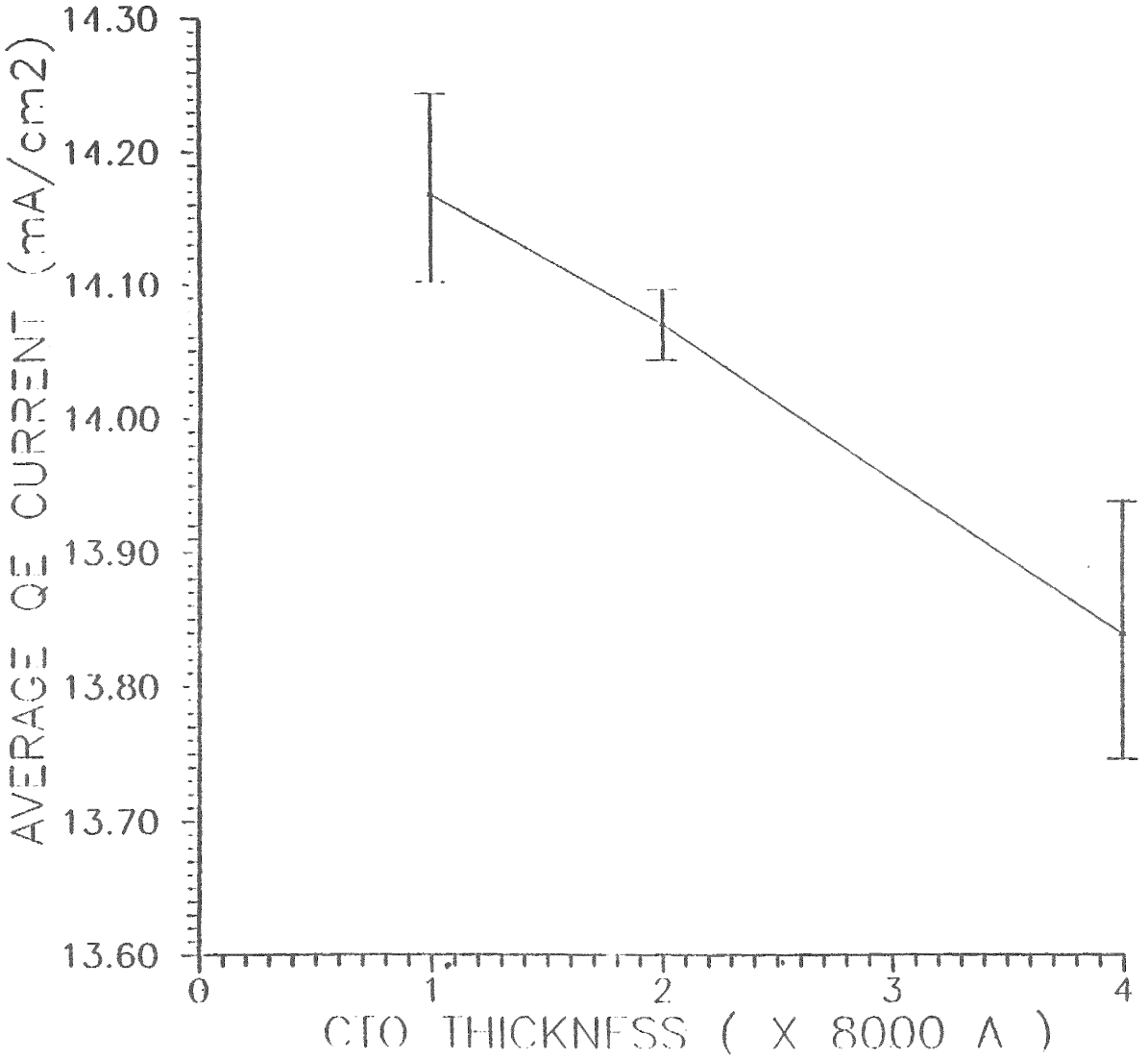

3.2 PROCESSES AND MATERIALS FOR SUBMODULE FINISHING

Investigation of materials and processing techniques for module finishing operations which are cost effective and adaptable to continuous in line manufacturing are ongoing. Process steps which are being examined include edge isolation, electrical connection and encapsulation for environmental protection. Simultaneous study of these factors has been undertaken because of their mutual interaction in manufacturing operations and in the capabilities of the finished product.

A high degree of electrical isolation is necessary for the safety and durability of high voltage array systems. Methods studied to achieve 1550 volts minimum wet isolation to the CTO coated edge include chemical etching, laser cutting and abrasive media blasting. Both laser cutting and abrasive media blasting in combination with a variety of coating materials including epoxy, urethane and asphaltic material consistently achieved isolation breakdown voltage greater than 1550 volts dc. Optimization of the isolation methods and coatings are continuing.

Improvements are also being sought in the methods of electrical interface with the basic PV module. Direct resistance welding to the aluminum backing metal, ultrasonic welding of nickel clad aluminum ribbon and printing of silver filled thick film and polymeric base conductors have been examined. Epoxy, polyester and polyimide base conductors have shown initial promise along with printed thick film silver. Each has survived 50 cycles of thermal cycle and 10 cycles of humidity freeze tests. More extensive environmental testing is in progress.

Resistance welds directly to the aluminum back metal have not been successful. The thin metal appears to prove insufficient thickness to survive this process. The feasibility of laser welding of aluminum metal to the back metal of the plate has been demonstrated. Apparently the control available in laser processing can overcome the difficulties of working with the thin backing metals. Ultrasonic welding of nickel clad aluminum ribbon to a previously welded aluminum ribbon was demonstrated. This provides means of replacing the large solder pad for wire connection with an equally solderable but more convenient wire connection point.

A variety of coating materials which can be applied to PV modules in a production oriented spray type process are being evaluated. Varnish, epoxy, urethane and their derivatives, epoxy urethane and acrylic urethane along with acrylic and asphaltic materials have been applied to modules. Epoxies and urethanes both appear promising as protective materials.

In addition these coatings have good dielectric properties and low moisture absorption which is essential to achieving electrical isolation to 1550 volts wet on both the edge and back of PV modules. Optimization of application techniques is required to achieve good adhesion, defect free and electrically insulating coatings in manufacturing operations.

4.0 SUBMODULE RESEARCH

4.1 HIGH EFFICIENCY MODULES WITH ITO/Ag/Al

The fabrication of high efficiency small area amorphous silicon solar cells often utilizes silver as a highly reflecting back metal contact. Other materials such as titanium, ITO, or ZnO often are deposited prior to silver. These materials serve as diffusion barriers to silver migration during heat treatments or they provide an enhanced red response in the quantum efficiency of the solar cells. Masks are used during the deposition of the back contact to the define the active area of the solar cells.

When silver or the combination of silver with other materials are used to fabricate large area modules special problems must be addressed. The primary problem is silver diffusion which electrically shorts the solar cell diodes when the metal is scribed with a laser or when the diodes are electrically cured. This problem is severe

when Ti/Ag is used as a back metal contact. When ITO/Ag is used this difficulty is minimized. Unfortunately, the laser scribing of ITO/Ag films can result in silver peeling and subsequent poor performance of solar cell modules.

One approach to solving the above problems is to deposit ITO/Ag over most of the area of module diodes using a mask that covers the laser scribing interconnect portions of the solar cell module. This metallization is then followed by an aluminum deposition over the entire module after the mask is removed. The result is a module that has ITO/Ag covering most of the area of the module diodes but has aluminum in the region of the laser scribed interconnects. In this way, a module retains the well established metal scribing of aluminum but has an enhanced red response (and corresponding J_{sc}) from ITO/Ag. A cross sectional view of a series connected module using ITO/Ag/Al is shown in Figure 4-1.

The best high efficiency modules use $1000cm^2$ quartz or pyrex substrates with approximately 5000Å textured CTO. Because of the relatively high cost of these substrates, development of the ITO/Ag/Al process is underway using small 3"x3" modules. Amorphous silicon depositions are made directly on 3"x3" substrates or on 12"x13" substrates which are subsequently cut into many 3"x3" substrates. Table 4-1 gives the best results for 3"x3" Al and ITO/Ag/Al modules.

Table 4-1 compares the results obtained on 3"x3" modules processed with ITO/Ag/Al metallization. The "best" V_{oc}, J_{sc}, FF, and η numbers are the highest observed for any module. However, no module is observed with all the best parameters in the same module. The typical parameters are more representative and often are observed together in one module. Table 4-2 gives the best results for a given module.

Generally, the ITO/Ag/Al metallization results in a J_{sc} that is ~0.6 to $0.9mA/cm^2$ higher than that found in an identical module which uses Al. Most of this current increase is in the red response of the modules. Modules processed using ITO/Ag/Al generally have lower FF than those with Al back metal contacts. The FF for both Al and for ITO/Ag/Al modules can be improved by optimizing the segment width of the modules.

Table 4-3 gives the results of experiments completed on variable segment widths for modules. The purpose of these experiments was to optimize the segment width to improve module fill factor. Standard pin amorphous silicon depositions were performed on manufacturing CTO having sheet resistivities approximately 18 to 20Ω/□. Aluminum was used as the back metal contact. The table given below summarizes the results for 3"x3" modules with increasing number of segments (decreasing segment width).

While these results should be interpreted cautiously because of several module processing factors, it is clear that decreasing the segment width improves the module fill factor and module performance. Fill factors in excess of 0.7 have not been observed previously. Now, fill factors in excess of 0.7 are often observed in 70 segment $1000cm^2$ modules (not just 3"x3" modules). Indeed, a marked performance improvement was obtained on 1/2 of 12"x13" modules containing 34 segments. A module efficiency of 9.43% (active area) was obtained with parameters of V_{oc} = 879mV/seg, J_{sc} = $15.05mA/cm^2$ and FF = 0.713. An AR coating was also used to enhance the efficiency.

The photovoltaic parameters and the losses in the area of the best a-Si:H single junction module are summarized in Table 4-4. The photovoltaic parameters of the highest fill-factor a-Si:H module are tabulated in Table 4-5.

Assuming very modest parameters of V_{oc} = 880mV, J_{sc} = $16.5mA/cm^2$, and FF = 0.7, a module efficiency over 10% can be obtained. It is believed that with optimization of the segment width all of these parameters will result in routine fabrication of high performance modules. Similarly this contacting method should yield very high (>13%) performance modules when coupled with the a-SiC/a-SiGe tandem devices.

FIGURE 4-1 CROSS SECTIONAL VIEW OF SERIES CONNECTED MODULES USING ITO/Ag/Al REAR CONTACTS.

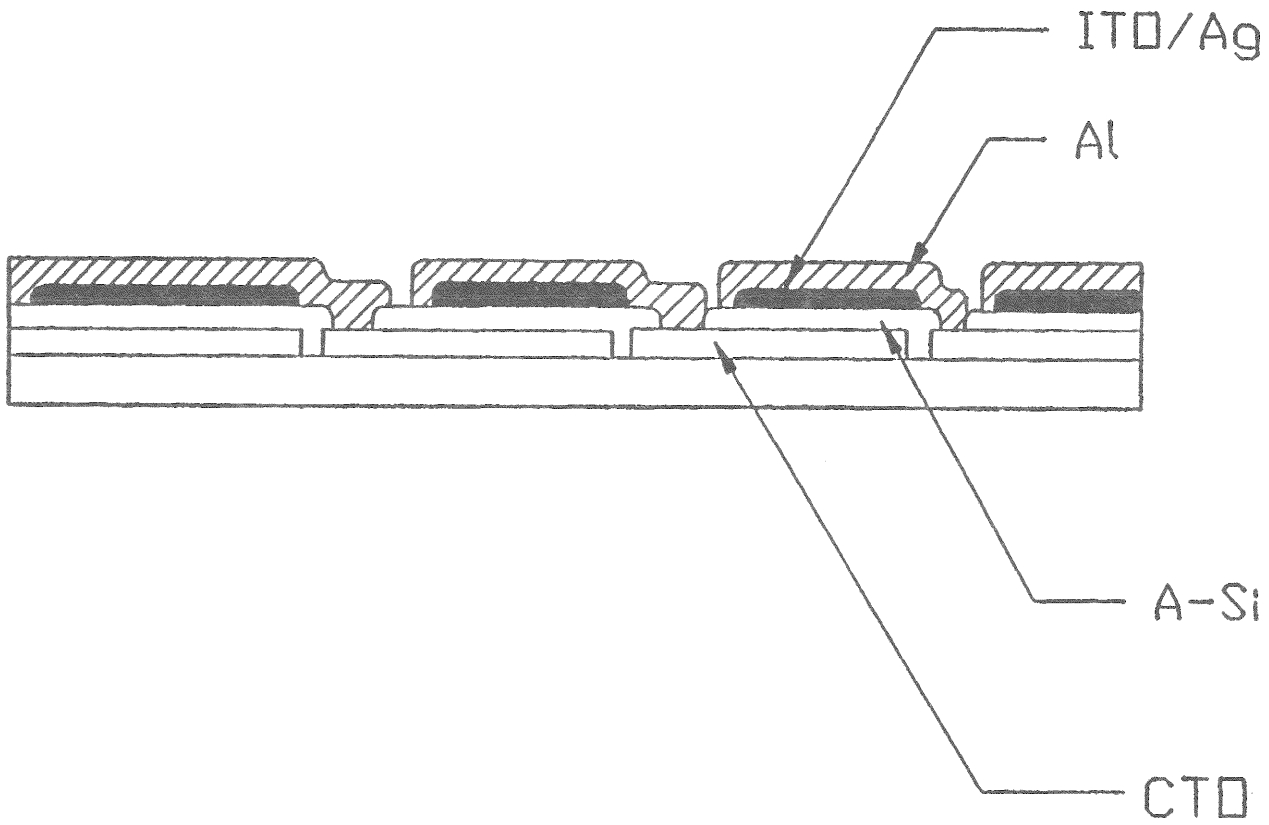

Table 4-1

COMPARISON OF TYPICAL AND BEST
IV CHARACTERISTICS OF 3"x3" MODULES

	Best	Typical
V_{oc}/segment	900mV	860-870mV
FF	0.67	0.64
J_{sc}	16.2mA/cm^2	15.8mA/cm^2
η_{act}	8.89%	8.6-8.8%

Table 4-2

BEST IV PARAMETERS OBSERVED
TOGETHER IN 3"x3" MODULES

	Metal	#Seg	V_{oc}	FF	J_{sc}	η_{active}
D2112	Al	5	4.492	.666	15.11	9.05
D2098	ITO/Ag/Al	5	4.352	.646	15.81	8.89

Table 4-3

FILL FACTOR MEASURED ON 3"x3" MODULE AFTER RBHT

Run #	# Seg per $1000cm^2$ Module	Seg Width (cm)	0 RBHT	1 RBHT	2 RBHT	3 RBHT
D2255	40	.72	.547	.587	.565	.564
D2253	50	.58	.616	.673	.687	.668
D2250	60	.48	.617	.692	.688	.691
D2248	70	.41	.713	.744	.740	.714

TABLE 4-4

SINGLE JUNCTION a-Si:H MODULE

Module #	D2248
V_{oc}	29.894V
I_{sc}	0.175A
FF	0.713
EFF	9.4%
P_{max}	3.73W
Segment Area	11.625cm^2
Active Area	337.125cm^2
# of Segments	29
	LOSSES
Border Losses	24.128cm^2
Edge Losses	45.419cm^2
1 Bad Segment	13.29cm^2
Scribe Loss	57.8cm^2
Total Losses	140.64cm^2
Total Area	503.22cm^2
Hence, total area efficiency	~6.77%
SERI Measured	6.5%

TABLE 4-5

PV PARAMETERS OF HIGHEST FILL FACTOR MODULE

V_{oc}	60.1V
I_{sc}	0.165A
FF	0.731
Efficiency	7.79%
# of Segments	70
Segment Width	11.625cm^2
Active Area	813.75cm^2

4.2 STACKED JUNCTION MODULES

During the period of this report over one hundred a-Si/a-Si stacked junction modules were fabricated. The average active area conversion efficiency was 6.07%. These devices incorporated a thin rear junction i-layer. Degradation studies were conducted under continuous illumination for 200 hours. Based on these studies we project a one year degradation of 14.8%. Little additional degradation occurs beyond this time. This is major improvement over single junction modules.

The highest conversion efficiency obtained on an all alloy tandem module with an a-SiC front cell and an a-SiGe rear cell was 7.73% (active area). The photovoltaic parameters of this module are tabulated in Table 4-6 and Figure 4-2 shows the J-V characteristics of this module. This module had a conventional rear contact of Al. The measurements were verified at SERI where a total area efficiency of 7% was measured.

4.3 ADVANCED SCRIBING PROCESSES

An advanced laser scribing process that reduces the number of scribing stations from three to two was recently developed at Solarex and described in an earlier report. This two-step process has the advantage that modules proceed from amorphous silicon processing into metallization without breaking vacuum. The final interconnection and metal scribing is accomplished as a final process. Figure 4-3 illustrates the advantage of this process. The entire manufacturing line decreases in size, throughput increases and capital equipment costs decrease.

The standard 30 segment SA-5 modules produced using the 2-step process have efficiencies equal to those using the 3-step The standard 30 segment SA-5 modules produced using the 2-step process have efficiencies equal to those using the 3-step process. However, they initially failed both environmental tests (50 temperature cycles from -40 to +90° C plus humidity) and sustained temperature (150° C) tests. Load currents dropped to <290mA and efficiencies decreased >1% (due mostly to changes in fill factor). In addition they degraded under illumination somewhat faster than control modules made with 3-step laser scribing.

Additional work on the 2-step process has resulted in improved 2-step scribes. Modules incorporating these scribes have now passed temperature-humidity cycling and sustained temperature tests, and the light-induced degradation of module performance after being subjected to both indoor and outdoor testing showed equal or better performance with time when compared to controls using 3-step scribing.

Figure 4-4 compares the change in I_{ld} (in mA) as a function of temperature humidity cycles. Earlier 2-step scribing processes used on modules show a degradation with increasing temperature cycling. However, the new improved 2-step scribing process used in modules show no significant change in I_{ld} with time, in line with typical results for (3-step) control modules.

Figure 4-5 shows plots of fill-factor vs time (hours) at 150° C for two sets of modules, one a control set and one a 2-step set. All the control modules have failed by 12 hours, while the 2-step scribe modules remain working with no deterioration in performance.

Figure 4-6 shows the results of continuous indoor light soaking by simulated AM1 light (~100mw/cm^2). As can be readily seen, the new improved 2-step scribing process used on modules produces slightly better performance than that of controls. Because the indoor light soaking data is at constant temperature, tests are currently underway outdoors. While the data are incomplete, the results shown in Figure 4-7 do illustrate favorable comparison to control modules. The data in Figure 4-7 derives from 1000cm^2 modules cut into two identical modules. One half of the module is processed with control scribing (3-step) and the other half is processed with the new improved 2-step process. Thus, the data compares modules identical in all processing except for the introduction of the new 2-step process.

TABLE 4-6

PV PARAMETERS OF BEST a-SiC/a-SiGe MODULE

V_{oc}	50.918V
I_{sc}	0.221A
FF	0.624
Efficiency	7.73%
# of Segments	30
Segment Width	$30.28cm^2$
Active Area	$908.4cm^2$
Power	7.02W
SERI Measured	7%

FIGURE 4-2 J-V CHARACTERISTICS OF a-SiC/a-SiGe MODULE (MEASURED AT SERI).

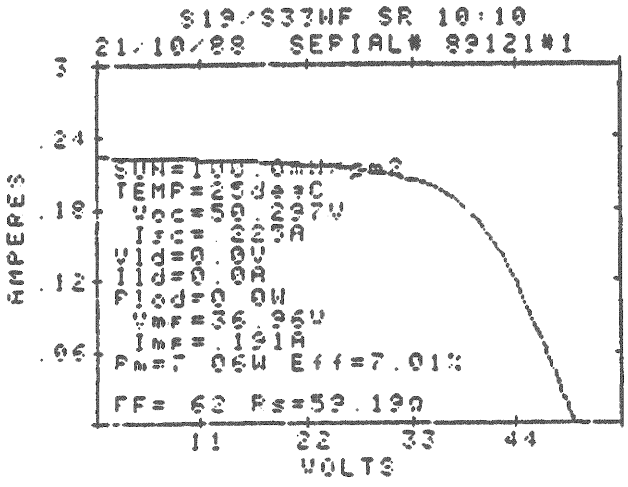

FIGURE 4-3 ILLUSTRATION OF TWO-STEP LASER SCRIBING PROCESS.

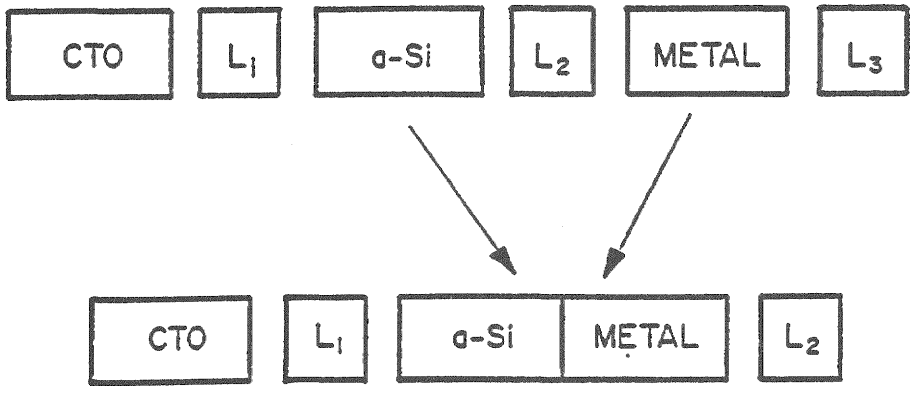

FIGURE 4-4 CHANGES IN FF AS A FUNCTION OF HOURS AT 150°C OF MODULES.

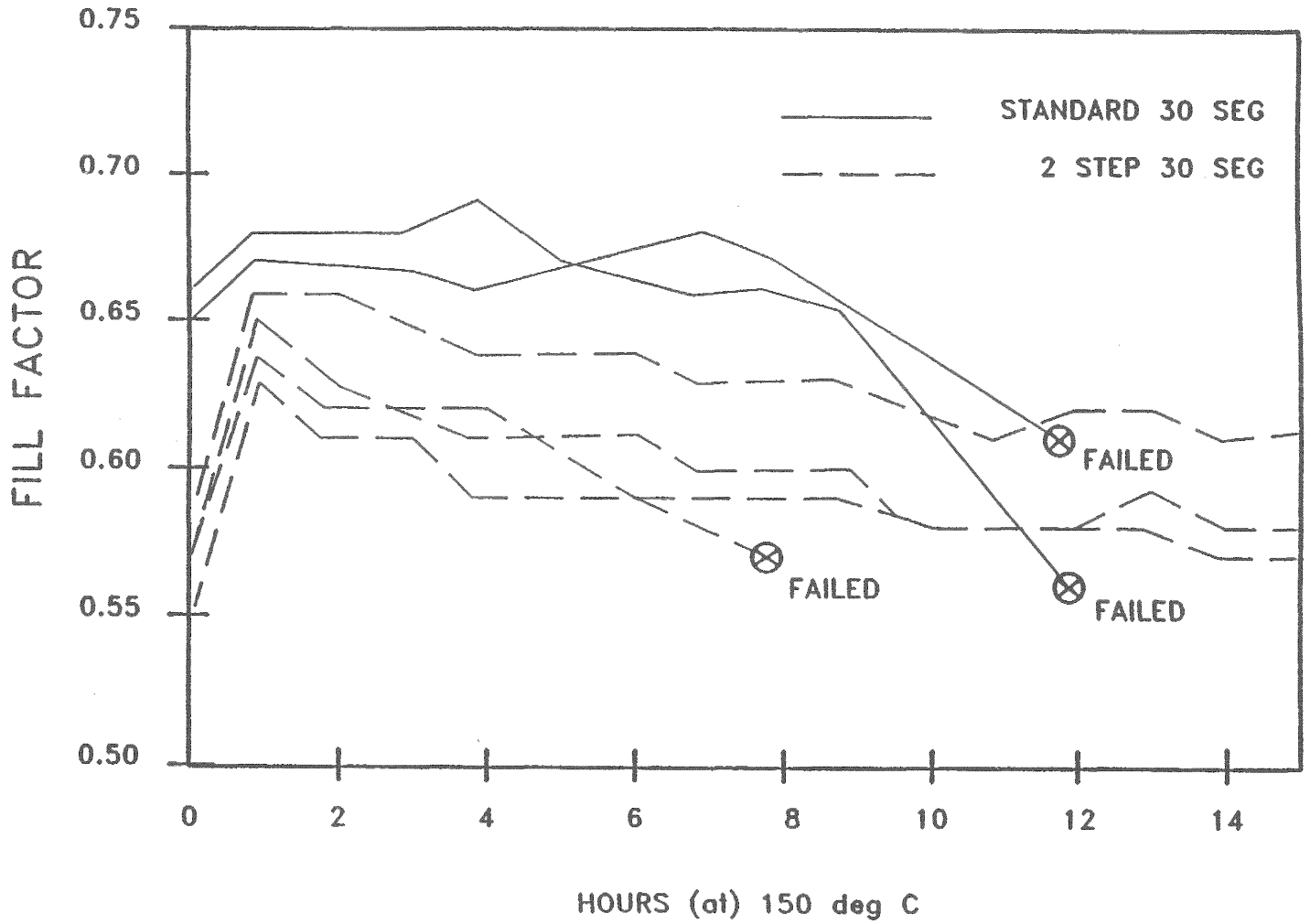

FIGURE 4-5 CHANGE IN I_{1d} AS A FUNCTION OF NUMBER OF TEMP-HUMIDITY CYCLES.

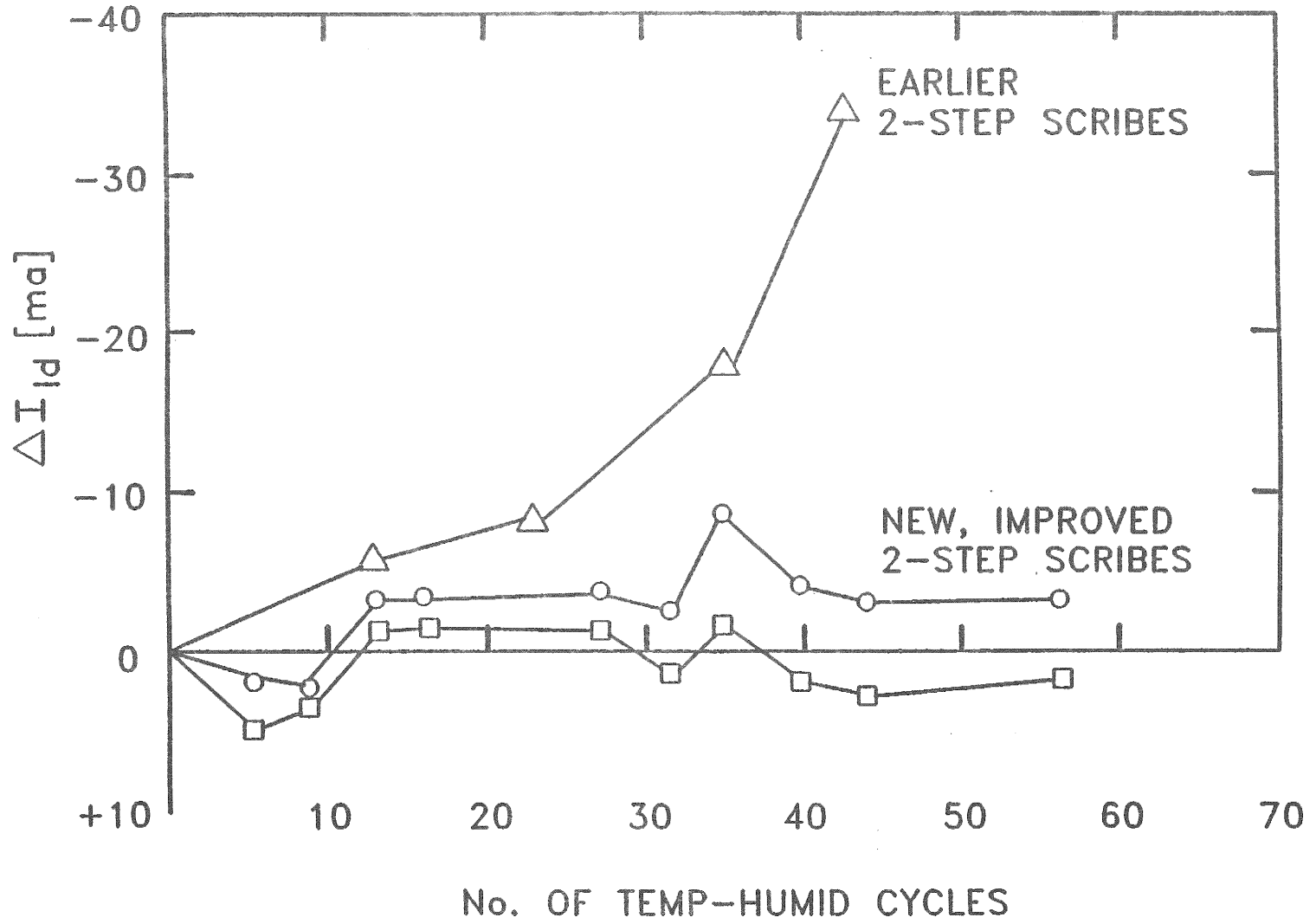

FIGURE 4-6 NORMALIZED POWER AS A FUNCTION OF HOURS OF INDOOR LIGHT SOAKING OF MODULES.

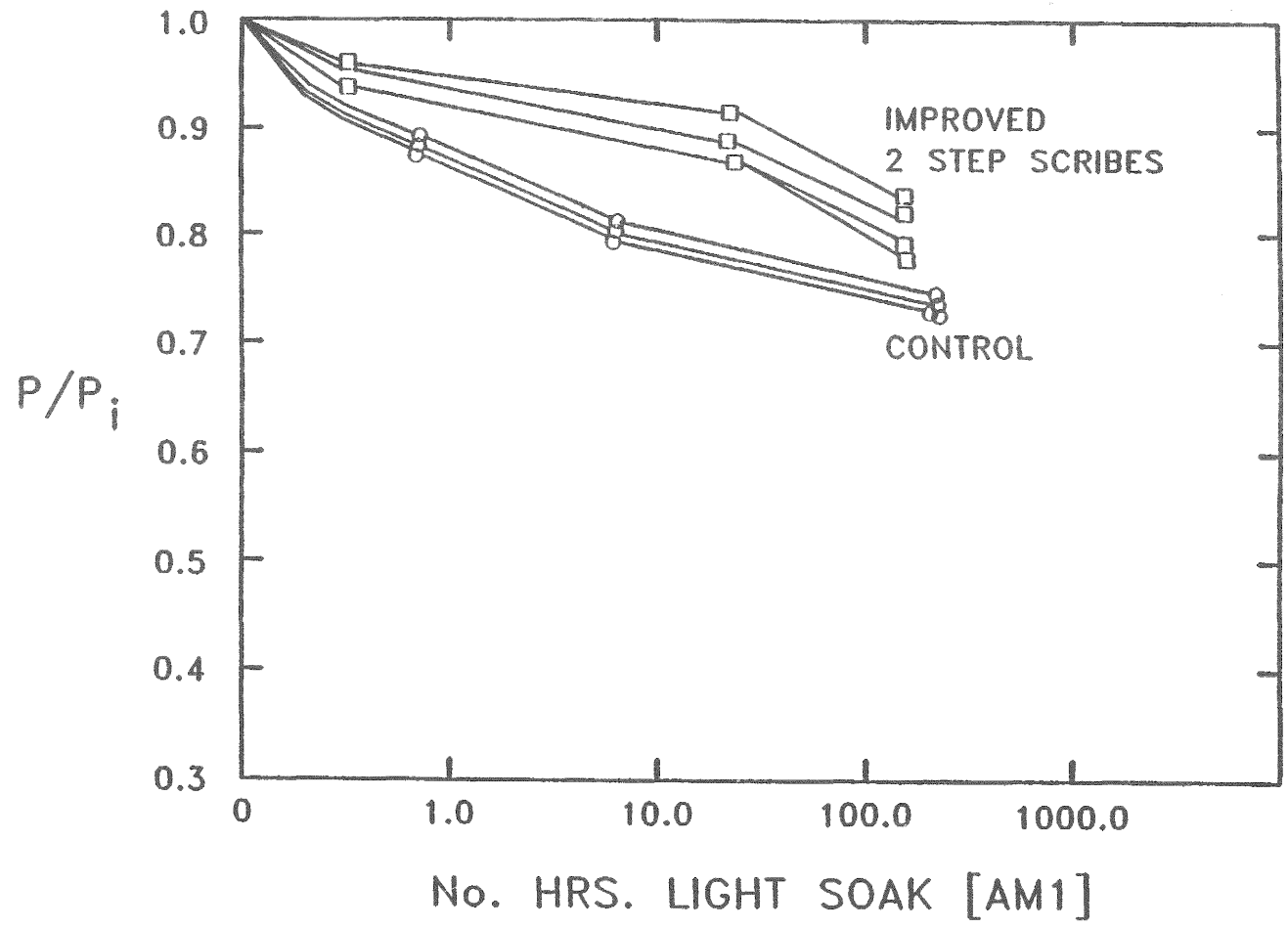

FIGURE 4-7 NORMALIZED POWER AS A FUNCTION OF NUMBER OF DAYS OF OUTDOOR EXPOSURE.

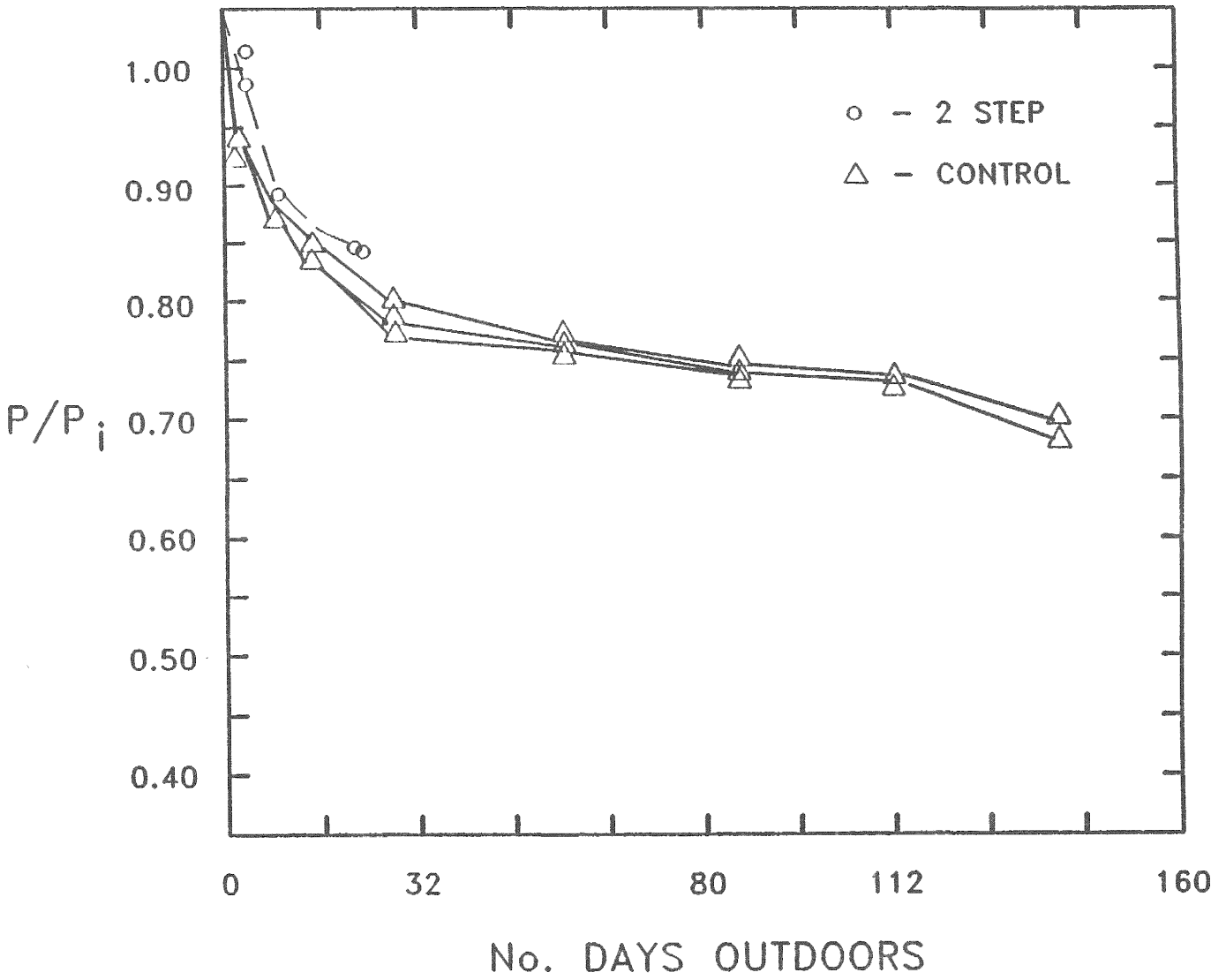

Document Control Page	1. SERI Report No. SERI/STR-211-3580	2. NTIS Accession No. DE89009491	3. Recipient's Accession No.

4. Title and Subtitle
Task B: Research on Stable High-Efficiency, Large Area Amorphous Silicon-Based Solar Cells, Phase II Annual Subcontract Report, 1 February 1988 - 1 February 1989

5. Publication Date
October 1989

6.

7. Author(s)
A.W. Catalano, Principle Investigator

8. Performing Organization Rept. No.

9. Performing Organization Name and Address
Solarex Thin Film Division
826 Newtown-Yardley Road
Newtown, Pennsylvania 18940

10. Project/Task/Work Unit No.

11. Contract (C) or Grant (G) No.
(C)ZB-7-06003-2
(G)

12. Sponsoring Organization Name and Address
Solar Energy Research Institute
1617 Cole Boulevard
Golden, Colorado 80401-3393

13. Type of Report & Period Covered
Technical Report

14.

15. Supplementary Notes
SERI Technical Monitor: Byron Stafford, (303) 231-7126

16. Abstract (Limit: 200 words)

This document describes photovoltaic research conducted in four areas: semiconductor materials, high-efficiency cells, nonsemiconductor materials, and submodules. The major focus of semiconductor materials research was on improving the quality of wide-band-gap a-SiC:H alloys and narrow-band-gap a-SiGe:H alloys. Raman spectroscopy suggested that the alloys are inhomogeneous, showing a higher concentration of Ge-Ge bonds than expected from a random mixing model. In high-efficiency device research, silicon-carbon single-junction cells resulted in open-circuit voltages as high as 0.96 V with a higher than 0.6 fill factor. Silicon-germanium cells show far better performance using a p/i-graded interface, an i(a-Si)/i(a-SiGe)-graded interface, and an inverse-graded interface at the i/n junction along with an a-Si n-layer compared with an a-SiGe:H n-layer. In the nonsemiconductor materials research, modeling optical enhancement of long-wavelength light in single-junction cells suggested that several parasitic losses are present in the device structure. In most cases, absorption in the rear contact is the major loss mechanism. In submodule research, the focus was on developing high-efficiency a-Si:H single-junction modules, stable a-Si:H stacked-junction modules, high-efficiency alloy-stacked modules, and advanced laser scribing processes.

17. Document Analysis
a. Descriptors Silicon solar cells ; efficiency ; semiconductor materials ; submodules

b. Identifiers/Open-Ended Terms

c. UC Categories 271

18. Availability Statement
National Technical Information Service
U.S. Department of Commerce
5285 Port Royal Road
Springfield, Virginia 22161

19. No. of Pages
115

20. Price
A06

Form No. 0069 (3-25-82)

☆U.S. GOVERNMENT PRINTING OFFICE: 1989 - 773 - 107/00023